

1 **A Measurement of the $t\bar{t}$ Cross Section in $p\bar{p}$ Collisions at**
2 **$\sqrt{s} = 1.96$ TeV using Dilepton Events with a Lepton plus Track**
3 **Selection**

4 T. Aaltonen,²⁴ J. Adelman,¹⁴ T. Akimoto,⁵⁶ B. Álvarez González^{t,12} S. Amerio^{z,44}
5 D. Amidei,³⁵ A. Anastassov,³⁹ A. Annovi,²⁰ J. Antos,¹⁵ G. Apollinari,¹⁸ A. Apresyan,⁴⁹
6 T. Arisawa,⁵⁸ A. Artikov,¹⁶ W. Ashmanskas,¹⁸ A. Attal,⁴ A. Aurisano,⁵⁴ F. Azfar,⁴³
7 W. Badgett,¹⁸ A. Barbaro-Galtieri,²⁹ V.E. Barnes,⁴⁹ B.A. Barnett,²⁶ P. Barria^{bb,47}
8 V. Bartsch,³¹ G. Bauer,³³ P.-H. Beauchemin,³⁴ F. Bedeschi,⁴⁷ D. Beecher,³¹ S. Behari,²⁶
9 G. Bellettini^{aa,47} J. Bellinger,⁶⁰ D. Benjamin,¹⁷ A. Beretvas,¹⁸ J. Beringer,²⁹ A. Bhatti,⁵¹
10 M. Binkley,¹⁸ D. Bisello^{z,44} I. Bizjak^{ff,31} R.E. Blair,² C. Blocker,⁷ B. Blumenfeld,²⁶
11 A. Bocci,¹⁷ A. Bodek,⁵⁰ V. Boisvert,⁵⁰ G. Bolla,⁴⁹ D. Bortoletto,⁴⁹ J. Boudreau,⁴⁸
12 A. Boveia,¹¹ B. Brau^{a,11} A. Bridgeman,²⁵ L. Brigliadori^{y,6} C. Bromberg,³⁶ E. Brubaker,¹⁴
13 J. Budagov,¹⁶ H.S. Budd,⁵⁰ S. Budd,²⁵ S. Burke,¹⁸ K. Burkett,¹⁸ G. Busetto^{z,44} P. Bussey,²²
14 A. Buzatu,³⁴ K. L. Byrum,² S. Cabrera^{v,17} C. Calancha,³² M. Campanelli,³⁶ M. Campbell,³⁵
15 F. Canelli^{14,18} A. Canepa,⁴⁶ B. Carls,²⁵ D. Carlsmith,⁶⁰ R. Carosi,⁴⁷ S. Carrillo^{n,19}
16 S. Carron,³⁴ B. Casal,¹² M. Casarsa,¹⁸ A. Castro^{y,6} P. Catastini^{bb,47} D. Cauz^{ee,55}
17 V. Cavaliere^{bb,47} M. Cavalli-Sforza,⁴ A. Cerri,²⁹ L. Cerrito^{p,31} S.H. Chang,²⁸ Y.C. Chen,¹
18 M. Chertok,⁸ G. Chiarelli,⁴⁷ G. Chlachidze,¹⁸ F. Chlebana,¹⁸ K. Cho,²⁸ D. Chokheli,¹⁶
19 J.P. Chou,²³ G. Choudalakis,³³ S.H. Chuang,⁵³ K. Chung,¹³ W.H. Chung,⁶⁰ Y.S. Chung,⁵⁰
20 T. Chwalek,²⁷ C.I. Ciobanu,⁴⁵ M.A. Ciocci^{bb,47} A. Clark,²¹ D. Clark,⁷ G. Compostella,⁴⁴
21 M.E. Convery,¹⁸ J. Conway,⁸ M. Cordelli,²⁰ G. Cortiana^{z,44} C.A. Cox,⁸ D.J. Cox,⁸
22 F. Crescioli^{aa,47} C. Cuenca Almenar^{v,8} J. Cuevas^{t,12} R. Culbertson,¹⁸ J.C. Cully,³⁵
23 D. Dagenhart,¹⁸ M. Datta,¹⁸ T. Davies,²² P. de Barbaro,⁵⁰ S. De Cecco,⁵² A. Deisher,²⁹
24 G. De Lorenzo,⁴ M. Dell'Orso^{aa,47} C. Deluca,⁴ L. Demortier,⁵¹ J. Deng,¹⁷ M. Deninno,⁶
25 P.F. Derwent,¹⁸ A. Di Canto^{aa,47} G.P. di Giovanni,⁴⁵ C. Dionisi^{dd,52} B. Di Ruzza^{ee,55}
26 J.R. Dittmann,⁵ M. D'Onofrio,⁴ S. Donati^{aa,47} P. Dong,⁹ J. Donini,⁴⁴ T. Dorigo,⁴⁴
27 S. Dube,⁵³ J. Efron,⁴⁰ A. Elagin,⁵⁴ R. Erbacher,⁸ D. Errede,²⁵ S. Errede,²⁵ R. Eusebi,¹⁸
28 H.C. Fang,²⁹ S. Farrington,⁴³ W.T. Fedorko,¹⁴ R.G. Feild,⁶¹ M. Feindt,²⁷ J.P. Fernandez,³²
29 C. Ferrazza^{cc,47} R. Field,¹⁹ G. Flanagan,⁴⁹ R. Forrest,⁸ M.J. Frank,⁵ M. Franklin,²³

30 J.C. Freeman,¹⁸ I. Furic,¹⁹ M. Gallinaro,⁵² J. Galyardt,¹³ F. Garberson,¹¹ J.E. Garcia,²¹
 31 A.F. Garfinkel,⁴⁹ P. Garosi^{bb},⁴⁷ K. Genser,¹⁸ H. Gerberich,²⁵ D. Gerdes,³⁵ A. Gessler,²⁷
 32 S. Giagu^{dd},⁵² V. Giakoumopoulou,³ P. Giannetti,⁴⁷ K. Gibson,⁴⁸ J.L. Gimmell,⁵⁰
 33 C.M. Ginsburg,¹⁸ N. Giokaris,³ M. Giordani^{ee},⁵⁵ P. Giromini,²⁰ M. Giunta,⁴⁷ G. Giurgiu,²⁶
 34 V. Glagolev,¹⁶ D. Glenzinski,¹⁸ M. Gold,³⁸ N. Goldschmidt,¹⁹ A. Golossanov,¹⁸
 35 G. Gomez,¹² G. Gomez-Ceballos,³³ M. Goncharov,³³ O. González,³² I. Gorelov,³⁸
 36 A.T. Goshaw,¹⁷ K. Goulianos,⁵¹ A. Gresele^z,⁴⁴ S. Grinstein,²³ C. Grosso-Pilcher,¹⁴
 37 R.C. Group,¹⁸ U. Grundler,²⁵ J. Guimaraes da Costa,²³ Z. Gunay-Unalan,³⁶ C. Haber,²⁹
 38 K. Hahn,³³ S.R. Hahn,¹⁸ E. Halkiadakis,⁵³ B.-Y. Han,⁵⁰ J.Y. Han,⁵⁰ F. Happacher,²⁰
 39 K. Hara,⁵⁶ D. Hare,⁵³ M. Hare,⁵⁷ S. Harper,⁴³ R.F. Harr,⁵⁹ R.M. Harris,¹⁸ M. Hartz,⁴⁸
 40 K. Hatakeyama,⁵¹ C. Hays,⁴³ M. Heck,²⁷ A. Heijboer,⁴⁶ J. Heinrich,⁴⁶ C. Henderson,³³
 41 M. Herndon,⁶⁰ J. Heuser,²⁷ S. Hewamanage,⁵ D. Hidas,¹⁷ C.S. Hill^c,¹¹ D. Hirschbuehl,²⁷
 42 A. Hocker,¹⁸ S. Hou,¹ M. Houlden,³⁰ S.-C. Hsu,²⁹ B.T. Huffman,⁴³ R.E. Hughes,⁴⁰
 43 U. Husemann,⁶¹ M. Hussein,³⁶ J. Huston,³⁶ J. Incandela,¹¹ G. Introzzi,⁴⁷ M. Iori^{dd},⁵²
 44 A. Ivanov,⁸ E. James,¹⁸ D. Jang,¹³ B. Jayatilaka,¹⁷ E.J. Jeon,²⁸ M.K. Jha,⁶ S. Jindariani,¹⁸
 45 W. Johnson,⁸ M. Jones,⁴⁹ K.K. Joo,²⁸ S.Y. Jun,¹³ J.E. Jung,²⁸ T.R. Junk,¹⁸ T. Kamon,⁵⁴
 46 D. Kar,¹⁹ P.E. Karchin,⁵⁹ Y. Kato^l,⁴² R. Kephart,¹⁸ W. Ketchum,¹⁴ J. Keung,⁴⁶
 47 V. Khotilovich,⁵⁴ B. Kilminster,¹⁸ D.H. Kim,²⁸ H.S. Kim,²⁸ H.W. Kim,²⁸ J.E. Kim,²⁸
 48 M.J. Kim,²⁰ S.B. Kim,²⁸ S.H. Kim,⁵⁶ Y.K. Kim,¹⁴ N. Kimura,⁵⁶ L. Kirsch,⁷ S. Klimentko,¹⁹
 49 B. Knuteson,³³ B.R. Ko,¹⁷ K. Kondo,⁵⁸ D.J. Kong,²⁸ J. Konigsberg,¹⁹ A. Korytov,¹⁹
 50 A.V. Kotwal,¹⁷ M. Kreps,²⁷ J. Kroll,⁴⁶ D. Krop,¹⁴ N. Krumnack,⁵ M. Kruse,¹⁷
 51 V. Krutelyov,¹¹ T. Kubo,⁵⁶ T. Kuhr,²⁷ N.P. Kulkarni,⁵⁹ M. Kurata,⁵⁶ S. Kwang,¹⁴
 52 A.T. Laasanen,⁴⁹ S. Lami,⁴⁷ S. Lammel,¹⁸ M. Lancaster,³¹ R.L. Lander,⁸ K. Lannon^s,⁴⁰
 53 A. Lath,⁵³ G. Latino^{bb},⁴⁷ I. Lazzizzera^z,⁴⁴ T. LeCompte,² E. Lee,⁵⁴ H.S. Lee,¹⁴ S.W. Lee^u,⁵⁴
 54 S. Leone,⁴⁷ J.D. Lewis,¹⁸ C.-S. Lin,²⁹ J. Linacre,⁴³ M. Lindgren,¹⁸ E. Lipeles,⁴⁶ A. Lister,⁸
 55 D.O. Litvintsev,¹⁸ C. Liu,⁴⁸ T. Liu,¹⁸ N.S. Lockyer,⁴⁶ A. Loginov,⁶¹ M. Loreti^z,⁴⁴
 56 L. Lovas,¹⁵ D. Lucchesi^z,⁴⁴ C. Luci^{dd},⁵² J. Lueck,²⁷ P. Lujan,²⁹ P. Lukens,¹⁸ G. Lungu,⁵¹
 57 L. Lyons,⁴³ J. Lys,²⁹ R. Lysak,¹⁵ D. MacQueen,³⁴ R. Madrak,¹⁸ K. Maeshima,¹⁸
 58 K. Makhoul,³³ T. Maki,²⁴ P. Maksimovic,²⁶ S. Malde,⁴³ S. Malik,³¹ G. Manca^e,³⁰
 59 A. Manousakis-Katsikakis,³ F. Margaroli,⁴⁹ C. Marino,²⁷ C.P. Marino,²⁵ A. Martin,⁶¹

60 V. Martin^k,²² M. Martínez,⁴ R. Martínez-Ballarín,³² T. Maruyama,⁵⁶ P. Mastrandrea,⁵²
 61 T. Masubuchi,⁵⁶ M. Mathis,²⁶ M.E. Mattson,⁵⁹ P. Mazzanti,⁶ K.S. McFarland,⁵⁰
 62 P. McIntyre,⁵⁴ R. McNulty^j,³⁰ A. Mehta,³⁰ P. Mehtala,²⁴ A. Menzione,⁴⁷ P. Merkel,⁴⁹
 63 C. Mesropian,⁵¹ T. Miao,¹⁸ N. Miladinovic,⁷ R. Miller,³⁶ C. Mills,²³ M. Milnik,²⁷ A. Mitra,¹
 64 G. Mitselmakher,¹⁹ H. Miyake,⁵⁶ N. Moggi,⁶ C.S. Moon,²⁸ R. Moore,¹⁸ M.J. Morello,⁴⁷
 65 J. Morlock,²⁷ P. Movilla Fernandez,¹⁸ J. Mülmenstädt,²⁹ A. Mukherjee,¹⁸ Th. Muller,²⁷
 66 R. Mumford,²⁶ P. Murat,¹⁸ M. Mussini^y,⁶ J. Nachtman^o,¹⁸ Y. Nagai,⁵⁶ A. Nagano,⁵⁶
 67 J. Naganoma,⁵⁶ K. Nakamura,⁵⁶ I. Nakano,⁴¹ A. Napier,⁵⁷ V. Necula,¹⁷ J. Nett,⁶⁰
 68 C. Neu^w,⁴⁶ M.S. Neubauer,²⁵ S. Neubauer,²⁷ J. Nielsen^g,²⁹ L. Nodulman,² M. Norman,¹⁰
 69 O. Norniella,²⁵ E. Nurse,³¹ L. Oakes,⁴³ S.H. Oh,¹⁷ Y.D. Oh,²⁸ I. Oksuzian,¹⁹ T. Okusawa,⁴²
 70 R. Orava,²⁴ K. Osterberg,²⁴ S. Pagan Griso^z,⁴⁴ E. Palencia,¹⁸ V. Papadimitriou,¹⁸
 71 A. Papaikonomou,²⁷ A.A. Paramonov,¹⁴ B. Parks,⁴⁰ S. Pashapour,³⁴ J. Patrick,¹⁸
 72 G. Pauletta^{ee},⁵⁵ M. Paulini,¹³ C. Paus,³³ T. Peiffer,²⁷ D.E. Pellett,⁸ A. Penzo,⁵⁵
 73 T.J. Phillips,¹⁷ G. Piacentino,⁴⁷ E. Pianori,⁴⁶ L. Pinera,¹⁹ K. Pitts,²⁵ C. Plager,⁹
 74 L. Pondrom,⁶⁰ O. Poukhov^{*},¹⁶ N. Pounder,⁴³ F. Prakoshyn,¹⁶ A. Pronko,¹⁸ J. Proudfoot,²
 75 F. Ptohosⁱ,¹⁸ E. Pueschel,¹³ G. Punzi^{aa},⁴⁷ J. Pursley,⁶⁰ J. Rademacker^c,⁴³ A. Rahaman,⁴⁸
 76 V. Ramakrishnan,⁶⁰ N. Ranjan,⁴⁹ I. Redondo,³² P. Renton,⁴³ M. Renz,²⁷ M. Rescigno,⁵²
 77 S. Richter,²⁷ F. Rimondi^y,⁶ L. Ristori,⁴⁷ A. Robson,²² T. Rodrigo,¹² T. Rodriguez,⁴⁶
 78 E. Rogers,²⁵ S. Rolli,⁵⁷ R. Roser,¹⁸ M. Rossi,⁵⁵ R. Rossin,¹¹ P. Roy,³⁴ A. Ruiz,¹² J. Russ,¹³
 79 V. Rusu,¹⁸ B. Rutherford,¹⁸ H. Saarikko,²⁴ A. Safonov,⁵⁴ W.K. Sakumoto,⁵⁰ O. Saltó,⁴
 80 L. Santi^{ee},⁵⁵ S. Sarkar^{dd},⁵² L. Sartori,⁴⁷ K. Sato,¹⁸ P. Savard,⁶² A. Savoy-Navarro,⁴⁵
 81 P. Schlabach,¹⁸ A. Schmidt,²⁷ E.E. Schmidt,¹⁸ M.A. Schmidt,¹⁴ M.P. Schmidt^{*},⁶¹
 82 M. Schmitt,³⁹ T. Schwarz,⁸ L. Scodellaro,¹² A. Scribano^{bb},⁴⁷ F. Scuri,⁴⁷ A. Sedov,⁴⁹
 83 S. Seidel,³⁸ Y. Seiya,⁴² A. Semenov,¹⁶ L. Sexton-Kennedy,¹⁸ F. Sforza^{aa},⁴⁷ A. Sfyrla,²⁵
 84 S.Z. Shalhout,⁵⁹ T. Shears,³⁰ P.F. Shepard,⁴⁸ M. Shimojima^r,⁵⁶ S. Shiraishi,¹⁴
 85 M. Shochet,¹⁴ Y. Shon,⁶⁰ I. Shreyber,³⁷ P. Sinervo,³⁴ A. Sisakyan,¹⁶ A.J. Slaughter,¹⁸
 86 J. Slaunwhite,⁴⁰ K. Sliwa,⁵⁷ J.R. Smith,⁸ F.D. Snider,¹⁸ R. Snihur,³⁴ A. Soha,⁸
 87 S. Somalwar,⁵³ V. Sorin,³⁶ T. Spreitzer,³⁴ P. Squillacioti^{bb},⁴⁷ M. Stanitzki,⁶¹ R. St. Denis,²²
 88 B. Stelzer,³⁴ O. Stelzer-Chilton,³⁴ D. Stentz,³⁹ J. Strologas,³⁸ G.L. Strycker,³⁵

* Deceased

89 J.S. Suh,²⁸ A. Sukhanov,¹⁹ I. Suslov,¹⁶ T. Suzuki,⁵⁶ A. Taffard^f,²⁵ R. Takashima,⁴¹
 90 Y. Takeuchi,⁵⁶ R. Tanaka,⁴¹ M. Tecchio,³⁵ P.K. Teng,¹ K. Terashi,⁵¹ J. Thom^h,¹⁸
 91 A.S. Thompson,²² G.A. Thompson,²⁵ E. Thomson,⁴⁶ P. Tipton,⁶¹ P. Ttito-Guzmán,³²
 92 S. Tkaczyk,¹⁸ D. Toback,⁵⁴ S. Tokar,¹⁵ K. Tollefson,³⁶ T. Tomura,⁵⁶ D. Tonelli,¹⁸
 93 S. Torre,²⁰ D. Torretta,¹⁸ P. Totaro^{ee},⁵⁵ S. Tourneur,⁴⁵ M. Trovato^{cc},⁴⁷ S.-Y. Tsai,¹
 94 Y. Tu,⁴⁶ N. Turini^{bb},⁴⁷ F. Ukegawa,⁵⁶ S. Vallecorsa,²¹ N. van Remortel^b,²⁴ A. Varganov,³⁵
 95 E. Vataga^{cc},⁴⁷ F. Vázquezⁿ,¹⁹ G. Velev,¹⁸ C. Vellidis,³ M. Vidal,³² R. Vidal,¹⁸ I. Vila,¹²
 96 R. Vilar,¹² T. Vine,³¹ M. Vogel,³⁸ I. Volobouev^u,²⁹ G. Volpi^{aa},⁴⁷ P. Wagner,⁴⁶
 97 R.G. Wagner,² R.L. Wagner,¹⁸ W. Wagner^x,²⁷ J. Wagner-Kuhr,²⁷ T. Wakisaka,⁴²
 98 R. Wallny,⁹ S.M. Wang,¹ A. Warburton,³⁴ D. Waters,³¹ M. Weinberger,⁵⁴ J. Weinelt,²⁷
 99 W.C. Wester III,¹⁸ B. Whitehouse,⁵⁷ D. Whiteson^f,⁴⁶ A.B. Wicklund,² E. Wicklund,¹⁸
 100 S. Wilbur,¹⁴ G. Williams,³⁴ H.H. Williams,⁴⁶ P. Wilson,¹⁸ B.L. Winer,⁴⁰ P. Wittich^h,¹⁸
 101 S. Wolbers,¹⁸ C. Wolfe,¹⁴ T. Wright,³⁵ X. Wu,²¹ F. Würthwein,¹⁰ S. Xie,³³ A. Yagil,¹⁰
 102 K. Yamamoto,⁴² J. Yamaoka,¹⁷ U.K. Yang^q,¹⁴ Y.C. Yang,²⁸ W.M. Yao,²⁹ G.P. Yeh,¹⁸
 103 K. Yi^o,¹⁸ J. Yoh,¹⁸ K. Yorita,⁵⁸ T. Yoshida^m,⁴² G.B. Yu,⁵⁰ I. Yu,²⁸ S.S. Yu,¹⁸
 104 J.C. Yun,¹⁸ L. Zanello^{dd},⁵² A. Zanetti,⁵⁵ X. Zhang,²⁵ Y. Zheng^d,⁹ and S. Zucchelli^y,⁶

105 (CDF Collaboration[†])

106 ¹*Institute of Physics, Academia Sinica,*
 107 *Taipei, Taiwan 11529, Republic of China*

108 ²*Argonne National Laboratory, Argonne, Illinois 60439*

109 ³*University of Athens, 157 71 Athens, Greece*

110 ⁴*Institut de Fisica d'Altes Energies,*

111 *Universitat Autònoma de Barcelona,*

112 *E-08193, Bellaterra (Barcelona), Spain*

113 ⁵*Baylor University, Waco, Texas 76798*

114 ⁶*Istituto Nazionale di Fisica Nucleare Bologna,*

115 ⁹*University of Bologna, I-40127 Bologna, Italy*

116 ⁷*Brandeis University, Waltham, Massachusetts 02254*

117 ⁸*University of California, Davis, Davis, California 95616*

118 ⁹*University of California, Los Angeles, Los Angeles, California 90024*

[†] With visitors from ^aUniversity of Massachusetts Amherst, Amherst, Massachusetts 01003, ^bUniversiteit Antwerpen, B-2610 Antwerp, Belgium, ^cUniversity of Bristol, Bristol BS8 1TL, United Kingdom, ^dChinese Academy of Sciences, Beijing 100864, China, ^eIstituto Nazionale di Fisica Nucleare, Sezione di Cagliari, 09042 Monserrato (Cagliari), Italy, ^fUniversity of California, Irvine, Irvine, CA 92697, ^gUniversity of

- 119 ¹⁰*University of California, San Diego, La Jolla, California 92093*
- 120 ¹¹*University of California, Santa Barbara, Santa Barbara, California 93106*
- 121 ¹²*Instituto de Fisica de Cantabria, CSIC-University of Cantabria, 39005 Santander, Spain*
- 122 ¹³*Carnegie Mellon University, Pittsburgh, PA 15213*
- 123 ¹⁴*Enrico Fermi Institute, University of Chicago, Chicago, Illinois 60637*
- 124 ¹⁵*Comenius University, 842 48 Bratislava,*
- 125 *Slovakia; Institute of Experimental Physics, 040 01 Kosice, Slovakia*
- 126 ¹⁶*Joint Institute for Nuclear Research, RU-141980 Dubna, Russia*
- 127 ¹⁷*Duke University, Durham, North Carolina 27708*
- 128 ¹⁸*Fermi National Accelerator Laboratory, Batavia, Illinois 60510*
- 129 ¹⁹*University of Florida, Gainesville, Florida 32611*
- 130 ²⁰*Laboratori Nazionali di Frascati, Istituto Nazionale*
- 131 *di Fisica Nucleare, I-00044 Frascati, Italy*
- 132 ²¹*University of Geneva, CH-1211 Geneva 4, Switzerland*
- 133 ²²*Glasgow University, Glasgow G12 8QQ, United Kingdom*
- 134 ²³*Harvard University, Cambridge, Massachusetts 02138*
- 135 ²⁴*Division of High Energy Physics, Department of Physics,*
- 136 *University of Helsinki and Helsinki Institute of Physics, FIN-00014, Helsinki, Finland*
- 137 ²⁵*University of Illinois, Urbana, Illinois 61801*
- 138 ²⁶*The Johns Hopkins University, Baltimore, Maryland 21218*
- 139 ²⁷*Institut für Experimentelle Kernphysik,*
- 140 *Universität Karlsruhe, 76128 Karlsruhe, Germany*
- 141 ²⁸*Center for High Energy Physics: Kyungpook National University,*
- 142 *Daegu 702-701, Korea; Seoul National University, Seoul 151-742,*
- 143 *Korea; Sungkyunkwan University, Suwon 440-746,*
- 144 *Korea; Korea Institute of Science and Technology Information, Daejeon,*
- 145 *305-806, Korea; Chonnam National University, Gwangju, 500-757, Korea*
- 146 ²⁹*Ernest Orlando Lawrence Berkeley National Laboratory, Berkeley, California 94720*
- 147 ³⁰*University of Liverpool, Liverpool L69 7ZE, United Kingdom*
- 148 ³¹*University College London, London WC1E 6BT, United Kingdom*
- 149 ³²*Centro de Investigaciones Energeticas*
- 150 *Medioambientales y Tecnologicas, E-28040 Madrid, Spain*

151 ³³*Massachusetts Institute of Technology, Cambridge, Massachusetts 02139*

152 ³⁴*Institute of Particle Physics: McGill University, Montréal,*

153 *Québec, Canada H3A 2T8; Simon Fraser University, Burnaby,*

154 *British Columbia, Canada V5A 1S6; University of Toronto,*

155 *Toronto, Ontario, Canada M5S 1A7; and TRIUMF,*

156 *Vancouver, British Columbia, Canada V6T 2A3*

157 ³⁵*University of Michigan, Ann Arbor, Michigan 48109*

158 ³⁶*Michigan State University, East Lansing, Michigan 48824*

159 ³⁷*Institution for Theoretical and Experimental Physics, ITEP, Moscow 117259, Russia*

160 ³⁸*University of New Mexico, Albuquerque, New Mexico 87131*

161 ³⁹*Northwestern University, Evanston, Illinois 60208*

162 ⁴⁰*The Ohio State University, Columbus, Ohio 43210*

163 ⁴¹*Okayama University, Okayama 700-8530, Japan*

164 ⁴²*Osaka City University, Osaka 588, Japan*

165 ⁴³*University of Oxford, Oxford OX1 3RH, United Kingdom*

166 ⁴⁴*Istituto Nazionale di Fisica Nucleare, Sezione di Padova-Trento,*

167 ^z*University of Padova, I-35131 Padova, Italy*

168 ⁴⁵*LPNHE, Universite Pierre et Marie*

169 *Curie/IN2P3-CNRS, UMR7585, Paris, F-75252 France*

170 ⁴⁶*University of Pennsylvania, Philadelphia, Pennsylvania 19104*

171 ⁴⁷*Istituto Nazionale di Fisica Nucleare Pisa, ^{aa}University of Pisa,*

172 ^{bb}*University of Siena and ^{cc}Scuola Normale Superiore, I-56127 Pisa, Italy*

173 ⁴⁸*University of Pittsburgh, Pittsburgh, Pennsylvania 15260*

174 ⁴⁹*Purdue University, West Lafayette, Indiana 47907*

175 ⁵⁰*University of Rochester, Rochester, New York 14627*

176 ⁵¹*The Rockefeller University, New York, New York 10021*

177 ⁵²*Istituto Nazionale di Fisica Nucleare, Sezione di Roma 1,*

178 ^{dd}*Sapienza Università di Roma, I-00185 Roma, Italy*

179 ⁵³*Rutgers University, Piscataway, New Jersey 08855*

180 ⁵⁴*Texas A&M University, College Station, Texas 77843*

181 ⁵⁵*Istituto Nazionale di Fisica Nucleare Trieste/Udine,*

182 *I-34100 Trieste, ^{ee}University of Trieste/Udine, I-33100 Udine, Italy*

183 ⁵⁶*University of Tsukuba, Tsukuba, Ibaraki 305, Japan*

184 ⁵⁷*Tufts University, Medford, Massachusetts 02155*

185 ⁵⁸*Waseda University, Tokyo 169, Japan*

186 ⁵⁹*Wayne State University, Detroit, Michigan 48201*

187 ⁶⁰*University of Wisconsin, Madison, Wisconsin 53706*

188 ⁶¹*Yale University, New Haven, Connecticut 06520*

189 ⁶²*Institute of Particle Physics: McGill University, Montréal,*
190 *Canada H3A 2T8; and University of Toronto, Toronto, Canada M5S 1A7*

191 (Dated: May 15, 2009)

Abstract

This paper reports a measurement of the cross section for the pair production of top quarks in $p\bar{p}$ collisions at $\sqrt{s} = 1.96$ TeV at the Fermilab Tevatron. The data was collected from the CDF Run II detector in a set of runs with a total integrated luminosity of 1.1 fb^{-1} . The cross section is measured in the dilepton channel, the subset of $t\bar{t}$ events in which both top quarks decay through $t \rightarrow Wb \rightarrow \ell\nu b$, where $\ell = e, \mu, \text{ or } \tau$. The lepton pair is reconstructed as one identified electron or muon and one isolated track. The use of an isolated track to identify the second lepton increases the $t\bar{t}$ acceptance, particularly for the case in which one W decays as $W \rightarrow \tau\nu$. The purity of the sample may be further improved at the cost of a reduction in the number of signal events, by requiring an identified b -jet. We present the results of measurements performed with and without the request of an identified b -jet. The former is the first published CDF result for which a b -jet requirement is added to the dilepton selection. In the CDF data there are 129 pretag lepton + track candidate events, of which 69 are tagged. With the tagging information, the sample is divided into tagged and untagged sub-samples, and a combined cross section is calculated by maximizing a likelihood. The result is $\sigma_{t\bar{t}} = 9.6 \pm 1.2(\text{stat.})_{-0.5}^{+0.6}(\text{sys.}) \pm 0.6(\text{lum.}) \text{ pb}$, assuming a branching ratio of $BR(W \rightarrow \ell\nu) = 10.8 \%$ and a top mass of $m_t = 175 \text{ GeV}/c^2$.

192 PACS numbers: 14.65.Ha,13.85.Qk

193 **I. INTRODUCTION**

194 Top quark data collected at the Tevatron have been an active testing ground for the
195 validity of the standard model since the discovery of the top quark in 1995 during Run
196 I [1, 2]. The definitive observation at both the CDF and DØ experiments used data where
197 one or both W 's from the top decays $t \rightarrow W^+b$ and $\bar{t} \rightarrow W^-\bar{b}$ decay in turn to a charged
198 lepton and neutrino.

199 This paper focuses on the dilepton channel, in which both W 's decay to leptons. The
200 final state contains two isolated charged leptons with large momentum in the direction
201 transverse to the beamline (p_T). The two neutrinos also carry large transverse momentum
202 but escape the detector without interacting. Their presence can be inferred by an imbalance
203 in the total reconstructed transverse momentum in the detector, referred to as the missing
204 transverse energy (\cancel{E}_T) because it is reconstructed from calorimeter information. Only the
205 momentum transverse to the beam can be used for this because in hadron collisions, the
206 total longitudinal momentum of the system is not known in any one collision, and large
207 longitudinal momentum may also be carried by very forward prongs which escape detection.
208 Combined with the jets produced by the hadronization of the b quarks, the distinctive
209 signature of the charged and neutral leptons allows the $t\bar{t}$ signature to be distinguished from
210 the background.

211 The top quark is unique because of its large mass
212 ($m_t = 173.1 \pm 0.6$ (stat.) ± 1.1 (sys.) GeV/c^2 [3]), which distinguishes it from the other
213 fermions of the standard model and is more akin to the masses of the weak force carriers
214 (W and Z) and the expected mass range for the proposed Higgs boson [4]. In Run II of the
215 Tevatron, at center-of-mass energy of 1.96 TeV, the CDF detector has collected well over
216 ten times the amount of integrated luminosity obtained in Run I. Using these data, the
217 study of the top quark sector continues, motivated by a desire to better understand this
218 unique corner of the standard model and to test for physics beyond what the model is able
219 to describe.

220 Precise measurements of the cross section are of fundamental interest because the top
221 quark is one of the most recent additions to the array of particles that can be produced in
222 the laboratory. The standard model predicts the production of top quark-antiquark pairs
223 through the strong interaction. The leading order Feynman diagrams are shown in Fig. 1.

224 Approximately 85% of $t\bar{t}$ pairs at the Tevatron are produced through quark-antiquark anni-
 225 hilation, and the remaining 15% through gluon-gluon fusion [5]. Because of the interaction
 226 scale involved, the cross section can be calculated using perturbative QCD techniques. The
 227 pair production cross section has been calculated at next-to-leading order (NLO), with the
 228 resummation of the leading logarithmic corrections due to the radiation of soft gluons com-
 229 pleted to next-to-leading logarithmic (NLL) order [6, 7]. These resummations do not change
 230 the calculated cross section by more than a few percent, but improve the stability of the
 231 result with respect to the normalization and factorization scales [5]. Recent updates to the
 232 cross section calculation [8–10] include newer parton distribution functions (PDFs) sets, with
 233 reduced associated uncertainties, and incorporate calculations of next-to-next-to-leading order
 234 (NNLO) terms. The predicted cross sections cited here have an accuracy of better
 235 than 10%. As the accuracy of measurements improves to a comparable level, meaningful
 236 comparison with the theoretical prediction becomes possible.

237 The measurements in this paper were completed using a reference cross section of
 238 $6.7_{-0.9}^{+0.7}$ pb, calculated for a top quark mass of $m_t = 175$ GeV/ c^2 [5]. The newer calcula-
 239 tions give similar answers with reduced uncertainties. For example, the similar calculation
 240 from Ref. [8] gives $6.6_{-0.5}^{+0.3}$ (scale) $_{-0.3}^{+0.4}$ (PDF) pb. Most numbers in this paper which depend
 241 on the theoretical calculation of the $t\bar{t}$ production cross section are quoted using the original
 242 reference cross section, but in the Results section (Sec. IX) we will compare the measured
 243 cross sections to the most recent predictions.

244 Significant deviation of the measured cross section from the predicted value could indi-
 245 cate the presence of new particles or interactions. Top quark pair production cross section
 246 measurements can be sensitive to new physics through the production of a new particle or
 247 particles which then decay to top quarks. Examples of this include a new heavy top quark
 248 of the type predicted by “little Higgs” theories [11], which decays to a top quark and a
 249 stable, heavy analog to the photon, which escapes the detector, adding extra \cancel{E}_T to the
 250 final state. The resulting signature is similar to top quark decay and would enhance the
 251 measured cross section. The production of $t\bar{t}$ pairs through a resonance would also raise the
 252 total cross section [12–14], although current limits on resonance production in the $t\bar{t}$ channel
 253 make it unlikely that it would be possible to distinguish the effects of a resonance on the
 254 cross section at the Tevatron [15–17].

255 The cross section could also be affected by a process with a final state sufficiently similar

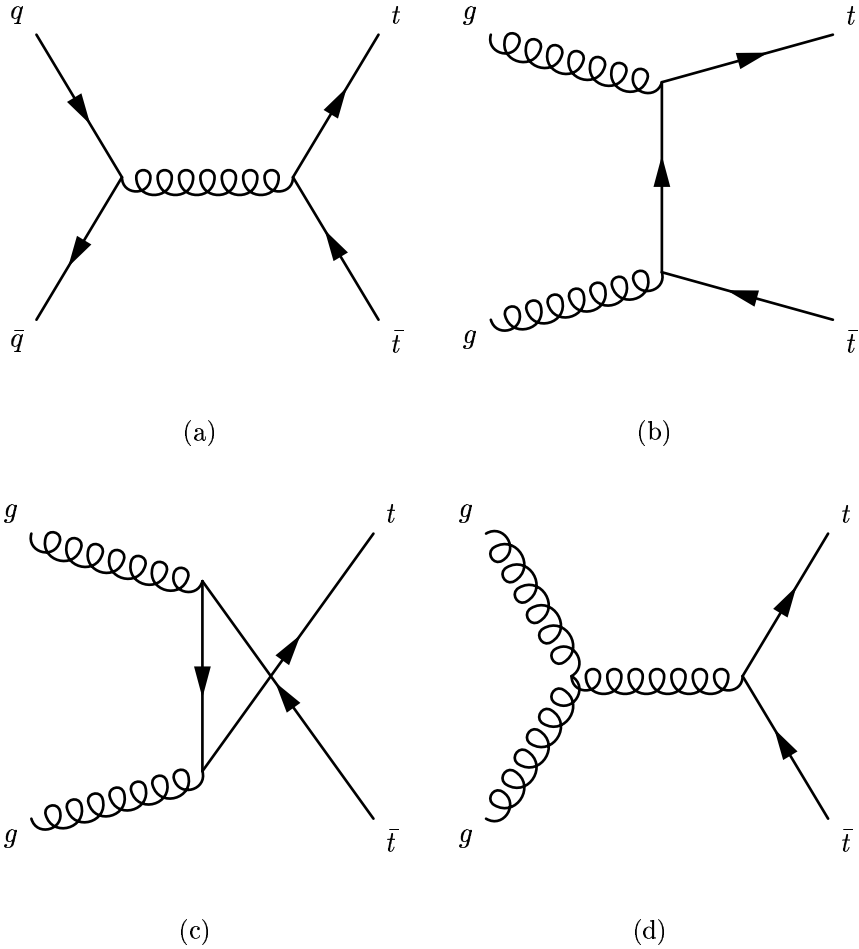


FIG. 1: Leading order diagrams for top quark pair production at the Tevatron.

256 to the $t\bar{t}$ signature to pass the event selection. The decay of supersymmetric particles
 257 is expected to produce multilepton, multijet signatures with significant missing transverse
 258 energy from the lightest supersymmetric particles escaping the detector [18, 19].

259 Finally, even in the absence of evidence of new physics at the Tevatron, a solid under-
 260 standing of the top quark sector and the composition of the multilepton + multijet + \cancel{E}_T
 261 sample will be a prerequisite to the discovery and understanding of new physics processes
 262 that may appear at the higher energies accessible at the CERN Large Hadron Collider
 263 (LHC). This is particularly important because of the approximately hundredfold increase
 264 in the $t\bar{t}$ production cross section at the 14 TeV center-of-mass energy at the LHC rela-
 265 tive to the Tevatron [8]. For example, the possibility of catching the decay signatures of
 266 supersymmetric partner particles with event selection designed for top quark pairs implies

267 the converse, that top quark production will be an important background in searches for
268 supersymmetry. Searches for new physics with top quarks in the final state, motivated by
269 models like those referenced above which have a heavy top partner or resonance, will also
270 rely on thorough understanding of the top signature and associated backgrounds.

271 In this paper, we measure the $t\bar{t}$ production cross section in the dilepton channel. The
272 final state contains two isolated charged leptons with large transverse momentum, missing
273 transverse energy from the undetected neutrinos, and two jets from the hadronization of the
274 b quarks (b -jets). One or more additional jets may also be present, having been produced
275 by initial or final state QCD radiation.

276 The dilepton channel, because of the dual leptonic W decays, has a smaller branching
277 ratio, about 1/9 if all τ decays are included, than the channels where one or both W 's
278 decay to quarks, which are referred to as the “lepton + jets” and “all-hadronic” channels,
279 respectively. The dilepton channel has the compensating advantage of a good (1:1 or better)
280 signal to background ratio even without the identification of jets as possible b decay products
281 (“tagging”), because so few standard model processes produce two high- p_T leptons and \cancel{E}_T .
282 Production of events with a W and jets ($W + \text{jets}$) is a background for the dilepton channel,
283 just as it is for the lepton + jets channel, but it does not overwhelm the $t\bar{t}$ signal in spite of its
284 large cross section, because one of the jets must pass the lepton selection used in this analysis.
285 Such a misreconstructed jet is referred to a “fake” lepton. The dilepton channel also does
286 not suffer from the same large QCD multijet background as does the all-hadronic channel,
287 for similar reasons. The background from Drell-Yan ($p\bar{p} \rightarrow Z/\gamma^* + X \rightarrow \ell\ell + X$)[63] is
288 reduced by the requirement of multiple jets and \cancel{E}_T . We also apply several criteria designed
289 specifically to veto Drell-Yan events, including an increased \cancel{E}_T threshold when the lepton
290 pair has a reconstructed invariant mass close to the Z resonance. Finally, those events which
291 may produce both real leptons and \cancel{E}_T , such as WW , are manageable backgrounds because
292 their cross section times branching ratio is comparable to or smaller than that for dilepton
293 $t\bar{t}$ events after the requirement of two or more jets.

294 We report on two measurements of the $t\bar{t}$ cross section using the dilepton final state, with
295 and without b -jet identification, using data collected between March 2002 and February
296 2006, corresponding to approximately 1.1 fb^{-1} of integrated luminosity, using the upgraded
297 Collider Detector at Fermilab (CDF II). These are updates of the previously published result
298 in which one of leptons is reconstructed simply as an isolated track, while the other must

299 be identified as an electron or muon of opposite sign [20]. The previous version did not
 300 use b -jet identification. The isolated track selection increases the acceptance by including
 301 most decay channels of τ leptons, thereby increasing the accessible branching fraction. It
 302 also recovers acceptance for electrons or muons that are not within the fiducial region of the
 303 calorimetry or muon detectors. We will refer to the selection criteria we use (excluding the
 304 b -jet identification), and the corresponding sample selected from the data, using the name
 305 “lepton + track”.

306 The previous CDF publication used Run II data corresponding to an integrated luminos-
 307 ity of 200 pb^{-1} . It included a cross section measurement in the lepton + track channel and
 308 a similar measurement where both leptons were fully reconstructed as electrons or muons.
 309 The combined result was $7.0_{-2.1}^{+2.4}$ (stat.) $_{-1.1}^{+1.6}$ (sys.) ± 0.4 (lum.) pb [20]. The DØ collabora-
 310 tion has also published a measurement in the dilepton channel using Run II data with an
 311 integrated luminosity of about 425 pb^{-1} . It includes measurements where both leptons were
 312 fully reconstructed as well as a measurement employing lepton + track and b -jet tagging
 313 selection similar to that used in this analysis. Combining the individual measurements, they
 314 find 7.4 ± 1.4 (stat.) ± 0.9 (sys.) ± 0.5 (lum.) pb [21].

315 This measurement is a substantial update of the analysis in the previous CDF publi-
 316 cation. It uses more than five times the amount of integrated luminosity. The calculated
 317 backgrounds and associated systematic uncertainties reflect an improved understanding of
 318 the background composition in the lepton + track sample, with the overall systematic un-
 319 certainty decreasing from about 1.4 pb to about 0.55 pb, i.e., from about 20% to 6% relative
 320 to the measured values of the cross section. We also perform the cross section measurement
 321 using the same event selection, but with the added requirement that at least one jet in the
 322 event is b -tagged. This significantly suppresses some otherwise irreducible backgrounds, in-
 323 creasing the purity of the candidate sample. The estimated signal to background ratio, using
 324 the theoretical cross section of 6.7 pb, is about 6:1 in the b -tagged sample, to be compared
 325 to about 1:1 in the pretag sample. Finally, we divide the pretag sample into its tagged and
 326 untagged components, in order to combine the results into a single cross section result with
 327 smaller uncertainties than the individual measurements.

328 CDF and DØ have also measured the cross section in other $t\bar{t}$ decay modes. In
 329 the lepton + jets mode, CDF has used two different methods to identify b -jets. One
 330 is based on the probability that a large number of tracks within a jet miss the pri-

331 mary vertex, and finds $\sigma_{t\bar{t}} = 8.9^{+1.0}_{-1.0}$ (stat.) $^{+1.1}_{-1.0}$ (sys.) pb in a data sample with an in-
 332 tegrated luminosity of 320 pb^{-1} [22]. The second measurement uses the same sample,
 333 but identifies b jets via a reconstructed secondary vertex significantly displaced from the
 334 beamline, using the same algorithm as is used in this paper, resulting in a cross sec-
 335 tion of 8.7 ± 0.9 (stat.) $^{+1.1}_{-0.9}$ (sys.) pb [23]. The DØ collaboration also has two recent
 336 results in the lepton + jets channel, both using a data sample with an integrated lu-
 337 minosity of 0.9 fb^{-1} . The first is a combined result from an analysis requiring a b -
 338 tagged jet and an analysis using a kinematic likelihood discriminant, with a result of
 339 $\sigma_{t\bar{t}} = 7.4 \pm 0.5$ (stat.) ± 0.5 (sys.) ± 0.5 (lum.) pb [24]. The second is a simultaneous
 340 fit to the cross section and the relative branching ratio $\mathcal{B}(t \rightarrow Wb)/\mathcal{B}(t \rightarrow Wq)$,
 341 where the q represents any down-type quark, resulting in a measured cross section of
 342 $8.2^{+0.9}_{-0.8}$ (stat.+sys.) ± 0.5 (lum.) pb [25]. In the all-hadronic channel, both CDF and DØ
 343 base their measurements on events with six or more jets, at least one of which is b -tagged.
 344 The CDF collaboration applies a neural-net-based discriminant before counting tags, and
 345 measures $\sigma_{t\bar{t}} = 8.3 \pm 1.0$ (stat.) $^{+2.0}_{-1.5}$ (sys.) ± 0.5 (lum.) pb in data with an integrated lu-
 346 minosity of 1.0 fb^{-1} [26]. The DØ collaboration also uses a neural-net discriminant and mea-
 347 sures $4.5^{+2.0}_{-1.9}$ (stat.) $^{+1.4}_{-1.1}$ (sys.) ± 0.3 (lum.) pb with 0.4 fb^{-1} [27]. All these measurements
 348 are quoted at the reference mass of $m_t = 175 \text{ GeV}/c^2$, and the uncertainty on the integrated
 349 luminosity is included in the systematic uncertainty if it is not written separately.

350 The cross section is determined by the number of candidate events N_{obs} , the integrated
 351 luminosity $\int \mathcal{L} dt$, the acceptance times efficiency for $t\bar{t}$ events $\mathcal{A}\epsilon$, and the calculated number
 352 of background events N_{bkg} . The acceptance \mathcal{A} is defined as the fraction of $t\bar{t}$ signal events
 353 passing the event selection, and includes the branching ratio of the W boson to a lepton
 354 pair of a particular flavor, for which we use the the measured value, 0.1080 ± 0.0009 [4]. We
 355 calculate the cross sections by maximizing the likelihood of obtaining the observed number
 356 of candidate events given the number predicted as a function of the $t\bar{t}$ cross section, $\sigma_{t\bar{t}}$. The
 357 number predicted, N_{pred} , is the sum of the signal and background contributions:

$$N_{\text{pred}} = \sigma_{t\bar{t}} \mathcal{A}\epsilon \int \mathcal{L} dt + N_{\text{bkg}}. \quad (1)$$

358 The uncertainties are taken from the cross section points where the logarithm of the like-
 359 lihood decreases by 0.5, and systematic uncertainties are included as nuisance parameters
 360 obeying Gaussian probability distributions. The central value from the likelihood maximiza-

361 tion is equal to the one obtained from the familiar formula

$$\sigma_{t\bar{t}} = \frac{N_{\text{obs}} - N_{\text{bkg}}}{\mathcal{A} \int \mathcal{L} dt}. \quad (2)$$

362 We choose to use a likelihood because it yields statistical uncertainties correctly reflecting
363 the fact that the number of candidates follows a Poisson probability distribution, and allows
364 extraction of a single cross section from multiple data samples.

365 The paper is structured as follows: First, we briefly describe relevant features of the
366 CDF II detector (Section II). We give details of the observed and simulated data samples
367 in Section III. The event selection is described in Section IV, and the acceptance for that
368 selection, including corrections, is described in Section V. In Section VI, we discuss the
369 algorithm to tag jets from b quarks and calculate the efficiency for tagging lepton + track $t\bar{t}$
370 events. The background estimation methods for the pretag and tagged samples are described
371 in Sections VII and VIII, respectively. The resulting cross section measurements, including
372 the combination method and combined result, are presented in Section IX.

373 II. THE CDF II DETECTOR

374 The CDF II detector is described in detail elsewhere [28]; we summarize here the com-
375 ponents relevant to our measurements. We use a cylindrical coordinate system where θ is
376 the polar angle defined with respect to the proton beam, φ is the azimuthal angle about
377 the beam axis measured relative to the plane of the accelerator, and the pseudorapidity,
378 η , is defined as $-\ln \tan(\theta/2)$. Transverse energy is defined as $E_T = E \sin \theta$, and transverse
379 momentum (p_T) is defined similarly.

380 The interaction region of the detector has a Gaussian width of $\sigma_z = 29$ cm. The circular
381 transverse cross section width is approximately $30 \mu\text{m}$ at $z = 0$ cm, rising to $50 \mu\text{m}$ at
382 $z = 40$ cm.

383 A. Tracking

384 The charged particle tracking system of the CDF detector is contained in a solenoid
385 magnet that produces a 1.4 T field coaxial with the beams, and measures the curvature
386 of particle tracks in the transverse plane. The innermost device employs silicon microstrip

387 sensors, and is composed of three sub-detectors. A single-sided layer of silicon sensors
 388 (L00) is installed directly onto the beryllium vacuum beam pipe, at an average radius of
 389 1.5 cm [29]. It is followed by five concentric layers of double-sided silicon sensors (SVXII),
 390 located at radii between 2.5 and 10.6 cm [30]. The intermediate silicon layers (ISL) consist
 391 of one double-sided layer at a radius of 22 cm in the central region and two double-sided
 392 layers at radii of 20 and 28 cm in the forward regions [31]. Typical strip pitch in the silicon
 393 sensors is 55 - 65 μm for axial strips, 60 - 75 μm for small-angle stereo strips (1.2°), and
 394 125 - 145 μm for 90° stereo strips. The axial-position resolution of the SVXII sensors is
 395 about 12 μm . For the ISL sensors, it is about 16 μm .

396 Surrounding the silicon sensors is the central outer tracker (COT), a 3.1 m long open-cell
 397 cylindrical drift chamber covering radii from 40 to 137 cm [32]. The COT has 96 measure-
 398 ment layers arrayed in eight alternating axial and 2° stereo superlayers of 12 wires each.
 399 The COT provides coverage for $|\eta| < 1$, and the fiducial region of the SVXII-ISL system
 400 extends out to $|\eta| \sim 2$. The resolution of the combined tracker for tracks with $\theta = 90^\circ$ is
 401 $\sigma(p_T)/p_T^2 = 0.15 \text{ \%/GeV}$.

402 B. Calorimetry

403 Outside of the tracking systems and the solenoid coil are the electromagnetic and
 404 hadronic calorimeters which measure the energy of particles that interact electromagneti-
 405 cally or hadronically, respectively. The central electromagnetic calorimeter (CEM) is a lead-
 406 scintillator sampling calorimeter which covers the range $|\eta| \leq 1.1$. The CEM has an energy
 407 resolution of $13.5\%/\sqrt{E_T}$ for electrons and photons [33]. The electromagnetic calorimeter in
 408 the forward regions (the “plug”) is of similar design, covers the region $1.2 \leq |\eta| \leq 3.6$, and
 409 has an energy resolution of $(16\%/\sqrt{E_T}) \oplus 1\%$ [34].

410 Crucial to electron and photon identification are the shower maximum detectors, placed
 411 at a depth of about six radiation lengths in the electromagnetic calorimeter. The shower
 412 maximum detectors allow detailed measurement, in the plane approximately transverse to
 413 the incident particle direction, of the shower shape at the expected peak of its develop-
 414 ment. The precision two-dimensional position measurements are made by orthogonal wire
 415 proportional chambers and resistive strips in the central calorimeter, and stereo layers of
 416 scintillator in the plug calorimeter [35, 36].

417 The hadronic calorimeter is an iron-scintillator sampling calorimeter, and is between
418 4.5 and 7 interaction lengths deep, depending on the pseudorapidity. It surrounds the
419 electromagnetic calorimeter and is divided into three sections: the central section covers
420 $|\eta| \lesssim 0.8$, the forward (plug) section covers $1.2 \leq |\eta| \leq 3.6$, and the “wall” section covers
421 the intermediate range.

422 The entire calorimetry system covers the pseudorapidity range $|\eta| < 3.6$. All calorimeters
423 are segmented into projective towers which point at the nominal center of the interaction
424 region.

425 C. Muon Detectors

426 In the pseudorapidity range $|\eta| \lesssim 0.6$, two sets of planar drift chambers are used to identify
427 muons. The inner layer (the CMU, for “Central Muon”) is located just outside of the central
428 hadron calorimeter towers. The outer layer (the CMP, for “Central Muon Upgrade”) is also
429 instrumented with scintillation counters for trigger and timing information. The CMP has a
430 square profile and lies outside the CMU, behind an additional 60 cm of iron shielding. Muons
431 in the region $0.6 < |\eta| < 1.0$ are detected with the Central Muon Extension (CMX), a layer
432 of drift chambers between layers of scintillator counters. The geometry of the CMX is that
433 of a pair of truncated cones, opening from the interaction point at the center of the detector.
434 The CDF muon system is described in more detail in Refs. [37] and [38]. By convention,
435 muons are named according to the muon detector in which they are reconstructed. A CMUP
436 muon has a track segment (“stub”) in both the CMU and CMP detectors.

437 D. Online Event Selection (Trigger)

438 The 2.5 MHz nominal bunch crossing-rate of the Tevatron far exceeds the rate at which
439 data can be written to permanent storage (75 Hz). CDF uses a three-level trigger system to
440 select a subset of the events to record [39, 40]. Each successive level of processing reduces
441 the event rate and refines the criteria used for event selection.

442 The first level, is implemented entirely through custom hardware. It uses information
443 from the calorimeter, the axial layers of the COT, and the muon detectors to quickly recon-
444 struct simple objects. Tracks are built from COT axial hits using a predefined set of patterns,

445 and electron and muon candidates are built from tracks matched to energetic towers in the
446 electromagnetic calorimeter and hit segments in the muon detectors, respectively.

447 Level 1 accepts events and passes them to the next level of processing, level 2, at a rate
448 of up to 50 kHz. Level 2, also built of custom hardware, performs further reconstruction.
449 In particular, clustering of calorimeter towers is performed, for photon, electron, and jet
450 identification.

451 Events satisfying level 2 criteria are passed to level 3, where they are directed to one of
452 about 300 dual-processor Linux computers. Level 3 applies the full event reconstruction,
453 using the same software that is used for offline analysis, including the application of prelimi-
454 nary calibration constants. This allows more stringent event selection to be made, improving
455 background rejection while maintaining efficiency for signal. Selected events are written to
456 tape for offline analysis.

457 E. Luminosity Determination

458 Luminosity is measured at CDF by a pair of conical Cerenkov detectors surrounding
459 the beam pipe, at $3.7 < |\eta| < 4.7$, on each side of the interaction region. Each detector
460 contains 48 smaller mylar cones filled with isobutane at about 1.5 atmospheres of pressure.
461 Photomultiplier tubes at the large ends of the mylar cones collect Cerenkov light produced
462 by particles emerging from inelastic $p\bar{p}$ scattering. The mean number of interactions per
463 beam crossing is inferred from the number of interactions in which no particles are observed
464 in either of the detectors (the “zero-counting method”). The instantaneous luminosity is
465 calculated from the mean number of interactions, the total inelastic $p\bar{p}$ cross section, and
466 the bunch crossing rate. The uncertainties on the luminosity are from the understanding of
467 the acceptance for the detectors as well as the 4% uncertainty on the value of the total $p\bar{p}$
468 cross section. The combined uncertainty of 6% contributes to the total uncertainty on the
469 cross section.

470 III. COLLISION DATA AND MONTE CARLO SAMPLES

471 We measure the $t\bar{t}$ cross section in the subset of the $p\bar{p}$ collision data which appear to have
472 at least one high- p_T lepton, as determined by the trigger system. To quantify the signal

473 acceptance, we use a sample of $t\bar{t}$ events which have been simulated using Monte Carlo
474 algorithms. Numerous other observed and simulated data samples are needed to refine the
475 estimated acceptance and estimate the background in the lepton + track sample. In this
476 section we describe the various samples used in this measurement.

477 A. Data Quality Requirements

478 Because the lepton + track event selection relies on many detector subsystems for the
479 reconstruction of electrons, muons, tracks, jets, and \cancel{E}_T , as well as the measurement of the
480 luminosity, we use only the CDF data in which all of the relevant parts of the detector
481 – the calorimetry, tracking, shower maximum, muon, and luminosity detectors – are fully
482 operational. For the measurement requiring a b -tag, we also require the silicon tracking
483 detector to be functioning because high-precision position measurements are necessary for
484 the reconstruction of a displaced secondary vertex. The integrated luminosity of the data
485 sample including information from the silicon detector is $1000 \pm 60 \text{ pb}^{-1}$. For the pretag
486 measurement, we include an additional 70 pb^{-1} which has no silicon information but which
487 is otherwise acceptable. For these data, PHX (forward) electrons cannot be reconstructed
488 and some tracking requirements are changed, as will be specified in Section IV.

489 B. Data Samples

490 We select lepton + track $t\bar{t}$ candidates from events passing the high- p_T lepton triggers.
491 There are high- p_T central and forward electron triggers, as well as triggers for both the
492 CMUP and CMX regions of the muon detectors. The central electron trigger selects events
493 containing a cluster with transverse energy greater than 18 GeV in the central electromag-
494 netic calorimeter and a matched track with $p_T > 9 \text{ GeV}/c$. Track matching is not available
495 online for forward electrons. To reduce the background trigger rate from jets, the electron
496 candidate E_T threshold is raised to 20 GeV, and the events are required to have at least
497 15 GeV of \cancel{E}_T . These requirements maintain efficiency for selecting electrons from W decays,
498 where the mean neutrino p_T is above 20 GeV/ c . Both electron triggers require the ratio of
499 the energy in the hadronic calorimeter to the energy in the electromagnetic calorimeter to
500 be less than 0.125 in order to reject hadronic jets. There are separate triggers for CMUP

501 and CMX muons. Each requires a track with $p_T > 20$ GeV/ c to be matched with a muon
502 track segment (“stub”) in the relevant detector(s).

503 Most of the data samples used in this measurement are derived from the set of events
504 passing the high- p_T lepton triggers. This includes the Z events used to study lepton identifi-
505 cation and the modeling of jet production by QCD radiation, as well as the W + jets sample
506 used in the calculation of the background from events with a fake lepton and the Z + jets
507 sample used in the calculation of the background from $Z/\gamma^* \rightarrow ee/\mu\mu$ + jets events.

508 To estimate the background from events with a fake lepton, we need a sample with a
509 large number of jets. We use the events passing a photon trigger with a transverse energy
510 threshold of 25 GeV.

511 C. Monte Carlo Samples

512 To calculate the acceptance of the lepton + track selection for the $t\bar{t}$ signal, we apply the
513 event selection to a sample of simulated $t\bar{t}$ events generated using PYTHIA version 6.216 [41]
514 for event generation and parton showering. The leptonic branching fraction for the W boson
515 is set to the measured value of 0.1080 ± 0.0009 [4]. For the central value of the cross section,
516 we use a sample generated with a top mass of $m_t = 175$ GeV/ c^2 . Identical samples generated
517 at other values of the top quark mass are used to recalculate the cross section at those mass
518 points. We also use a sample of $t\bar{t}$ events generated using HERWIG version 6.510 [42] to check
519 the dependence of the calculated acceptance on the event generator.

520 To estimate the contribution of backgrounds to the lepton + track sample, we use other
521 Monte Carlo samples, which will be described in the relevant sections. Most of them are
522 generated using PYTHIA, in the same version as the signal. For some studies, we use a
523 W + jets sample with matrix elements calculated by ALPGEN version 2.10' [43] and PYTHIA
524 used for parton showering.

525 In the Monte Carlo samples in this paper, we use the CTEQ5L parton distribution func-
526 tions to model the momentum distribution of the initial state partons [44]. The interactions
527 of particles with the detector are modeled using GEANT version 3 [45], using the GFLASH
528 parameterization [46] for showers in the calorimeter. Details on the implementation and
529 tuning of the CDF detector simulation may be found in Ref. [47].

530 IV. LEPTON + TRACK EVENT SELECTION

531 The lepton + track sample is drawn from the set of events with one or more fully re-
532 constructed electron or muon candidates and at least one isolated track which is distinct
533 from the first lepton and has the opposite sign. We also require candidate events to have
534 significant missing transverse energy (\cancel{E}_T), a key discriminant between the $t\bar{t}$ signal and
535 backgrounds, particularly Drell-Yan events where the final state leptons are electrons or
536 muons. The \cancel{E}_T in such events is generally the result of mismeasurement of the energies of
537 leptons or jets and the resulting distribution falls off rapidly with increasing \cancel{E}_T . For this
538 reason, we make a series of corrections to the \cancel{E}_T and place restrictions on the final-state
539 kinematics to reduce residual contributions from such events.

540 The requirement that the isolated track has the opposite charge of the fully reconstructed
541 lepton candidate reduces the contribution from events where, due to a fluctuation of frag-
542 mentation and hadronization, a jet has reproduced the signature of a lepton candidate. This
543 requirement is nearly 100% efficient for the signal and all other backgrounds, but only 61%
544 efficient for the background from events with jets producing a lepton-like signature.

545 Finally, we require events to have two or more jets. The $t\bar{t}$ signal contains two b jets
546 at leading order, while the cross sections of the backgrounds are significantly reduced by
547 requiring two or more jets in the final state.

548 A. Electron Selection

549 The electron and muon identification criteria used in this analysis are very similar to those
550 described in Ref. [28]. Electron selection is based on a reconstructed track, energy deposition
551 in the electromagnetic calorimeter, and the quality of the match between the track and the
552 energy signature in the calorimeter. This analysis uses two classes of electrons. Central
553 (“CEM”) electrons, in the range $|\eta| \lesssim 1.1$, have tracks in the central tracker and deposit their
554 energy in the central electromagnetic calorimeter. Forward (“PHX”) electrons are identified
555 in the range $1.2 \lesssim |\eta| \lesssim 2.0$, and deposit their energy in the plug electromagnetic calorimeter.
556 Forward electrons have tracks that use information from the silicon tracker, and derive their
557 abbreviated name “PHX” from “Phoenix”, the name of the tracking algorithm [48].

558 *1. Calorimeter Requirements*

559 First, the calorimeter cluster of the electron must have $E_T > 20$ GeV, calculated after the
560 electron energy has been corrected for calorimeter nonuniformities and the absolute energy
561 scale. The cluster must also be isolated, in the sense that the total energy in the towers in
562 a cone surrounding the tower containing the candidate electron shower is required to be less
563 than 10% of the candidate electron energy. The cone is defined to include objects within
564 $\Delta R = \sqrt{\Delta\eta^2 + \Delta\varphi^2} < 0.4$ around the candidate, but the towers in the electron cluster are
565 excluded. The distribution of energy between the towers in the cluster and the shape of
566 the shower in the shower maximum detector are required to be consistent with expectation
567 as determined, for instance, in test beam and studies of electrons from W and Z decays.
568 Finally, the amount of energy deposited in the hadronic part of the calorimeter must be sig-
569 nificantly less than the amount deposited in the electromagnetic part. For central electrons,
570 we require that the energy in the hadronic calorimeter be less than 5.5% of the energy in
571 the electromagnetic calorimeter, with a small energy-dependent correction to allow for the
572 fact that showers from more energetic electrons extend farther into the hadronic calorimeter.
573 For plug electrons, we require that the energy in the hadronic calorimeter be less than 5%
574 of the energy in the electromagnetic calorimeter.

575 *2. Track Reconstruction and Requirements*

576 Central electron candidate tracks are three-dimensional helices reconstructed from COT
577 hit information. If there are silicon hits in the path of the track through the silicon tracking
578 system, the hits are added and the track is refitted. This makes the measurement of track
579 parameters more precise, but we do not require silicon hits, to maintain efficiency and allow
580 use of data where the silicon tracking detector was not in use. Candidate tracks must have
581 at least three axial and two stereo segments in the COT, where each segment is a set of at
582 least five of twelve possible hits contained in a single superlayer.

583 Forward electron candidate tracks are reconstructed in the silicon tracker. The track
584 reconstruction algorithm builds seed track helices from plug calorimeter information, taking
585 a point from the shower maximum cluster centroid and another from the interaction vertex.
586 The curvature is estimated by equating the momentum to the energy in the calorimeter.

587 This yields two track hypotheses, one for each choice of sign. A road-based search algorithm
588 attempts to attach silicon hits to each of the track hypotheses, and helices with attached hits
589 are refit for a more precise measurement of the track parameters. The track fit is considered
590 successful if three or more silicon hits are attached and the fit has a χ^2 per degree of freedom
591 less than 10. If there are multiple tracks found for an electron candidate, the one with the
592 best fit quality, as measured using the χ^2 per degree of freedom, is taken. For both central
593 and plug electron candidates, we require the track to originate from a point along the beam
594 line that is less than 60 cm from the nominal center of the detector ($|z_0| < 60$ cm).

595 3. *Conversion veto*

596 Central electrons may be flagged as having originated from a photon conversion if there
597 is a second track near to the electron track with opposite sign. We do not use central
598 electrons which have been flagged as conversions. There is no explicit conversion veto for
599 forward electrons, but the silicon tracking algorithm suppresses tracks from conversions.
600 The algorithm creates a track hypothesis assuming that the electron track is prompt and
601 has momentum equal to the energy in the calorimeter, but these assumptions are wrong for
602 most conversion electrons. Silicon hits from conversion electron tracks will not generally be
603 close enough to the track hypothesis to be attached, and the track finding fails.

604 B. Muons

605 Muon candidates are defined as a track in the COT with $p_T > 20$ GeV/ c matched to a
606 track segment in one or more of the muon drift chambers. We require either a stub in both
607 the CMU and CMP detectors, or a stub in the CMX detector, and refer to the resulting
608 muon candidates as CMUP or CMX muons, respectively. Requiring muon signatures in
609 both the CMU and CMP detectors reduces the probability of reconstructing a muon from
610 a hadron that reaches the CMU as a result of a particle shower that is not fully contained
611 in the hadronic calorimeter.

612 1. *Calorimeter Signature*

613 The energy deposited in the region of the calorimeter intersected by the candidate muon
614 track is required to be consistent with the expectation for a minimum-ionizing particle.
615 Specifically, there must be no more than 2 GeV in the electromagnetic calorimeter and
616 6 GeV in the hadronic calorimeter, with a small correction for muons with momentum over
617 100 GeV/ c to allow for the expected rise in ionization. We also require muon candidates
618 to be isolated in the sense that the total sum E_T in the calorimeter towers in a cone of
619 $\Delta R < 0.4$ around the one intersected by the extrapolated muon track is less than 10% of
620 the muon p_T .

621 2. *Tracking Requirements*

622 Muon candidates use the same tracks and track quality requirements as central electron
623 candidates. We make a few additions to the quality requirements from muons, motivated
624 by backgrounds particular to muons, such as cosmic rays and kaon decays-in-flight. In
625 addition to the COT track and z_0 requirement, the candidate track must have a small
626 impact parameter (d_0). The impact parameter is the two-dimensional distance, in the plane
627 transverse to the beam direction, between the beamline and the point of closest approach
628 of the track helix to the beamline. We require that the impact parameter for muon tracks
629 be less than 20 (200) μm for tracks with (without) attached silicon hits. We also require
630 that the χ^2 , given the number of degrees of freedom in the track fit (i.e., the number of
631 hits on the track minus the number of fit parameters) is such that the probability to have
632 found a larger χ^2 for that track by chance is greater than 10^{-8} . This in essence requires
633 that the track be well reconstructed. It is similar in spirit to a requirement that the χ^2 or
634 χ^2 per degree of freedom be less than a specified value, but it removes the dependence of
635 the efficiency for good tracks on the number of degrees of freedom.

636 3. *Track-Stub Matching*

637 We check the quality of the spatial match between the COT track and the muon stub(s).
638 The quantity used is the distance between the track stub in the muon detectors and the
639 point at which the extrapolated COT track crosses the front plane of the corresponding

640 detector element. The distance is measured in the plane of the muon detector, transverse to
641 the measurement wires. A CMUP muon track must extrapolate to within 7 cm of the CMU
642 stub and within 5 cm of the CMP stub. For CMX, the maximum allowed displacement is
643 6 cm.

644 C. Track Lepton Selection

645 We use an isolated high- p_T track to identify the second lepton in the event. To qualify,
646 the tracks must have $p_T > 20$ GeV/ c , pass certain quality requirements, and be isolated in
647 $\eta - \varphi$ space from other energetic track activity. The track may be left by either a charged
648 lepton or a charged hadron from the decay of a τ lepton, but it is in either case indicative
649 of the presence of a lepton. The isolated track, in this role, is also referred to as a “track
650 lepton” because its identification relies entirely on information from the tracking detectors,
651 and also to distinguish it from the fully reconstructed electron and muon candidates. The
652 added acceptance for $t\bar{t}$ signal events where one and sometimes even both W ’s have decayed
653 to a τ and ν_τ is discussed in more detail in Sec. V.

654 1. Track quality

655 As is the case for muons, it is important for the track to be well-measured, both to reject
656 background and because the track momentum is the only measure of the particle’s energy.
657 The track must have at least 24 hits in the axial layers of the COT and at least 20 hits in the
658 stereo layers and satisfy the same χ^2 probability requirement as muons. The requirement
659 of a minimum number of track hits limits the acceptance for track leptons to $|\eta| \lesssim 1.15$,
660 according to the geometry of the COT. There is also a maximum allowed impact parameter,
661 0.025 cm, but unlike the muon case, the requirement is independent of the presence of silicon
662 hits. We also require silicon hits to be present if they are expected, to reduce the incidence
663 of fake tracks reconstructed from accidental combinations of hits. Specifically, if the track
664 passes through three or more layers of the silicon tracker known to be functional, it must
665 have at least three silicon hits attached.

666 2. *Track isolation*

667 Track isolation is crucial to the rejection of backgrounds from jets. We sum the p_T of every
668 track with $p_T > 0.5$ GeV/ c , including the candidate track, within a cone of $\Delta R < 0.4$ around
669 the candidate. The ratio of the candidate track p_T to the sum p_T in the cone is required
670 to be at least 0.9. To be included in the p_T sum, tracks must pass quality requirements
671 similar to, but less stringent than, those for the track lepton. No χ^2 probability or impact
672 parameter restrictions are made, and only 20 axial and 16 stereo hits are required.

673 **D. Jet Definition**

674 Jet reconstruction is based on a calorimeter tower clustering cone algorithm with a cone
675 size of $\Delta R = 0.4$. Towers corresponding to identified electrons according to the definition
676 above are removed before clustering. The E_T values of the jets are corrected for the ef-
677 fects of jet fragmentation, calorimeter non-uniformities and the calorimeter absolute energy
678 scale [49].

679 We extend the jet definition to facilitate the calculation of the rate for a jet to be re-
680 constructed as an isolated track, and use this jet definition everywhere in the analysis for
681 consistency. The details of the fake lepton background calculation are described in Sec-
682 tion VII A, but the core idea is to ensure that any object which could be identified as a track
683 lepton is included in the jet collection, because that jet collection forms the denominator of
684 the measured probability for an object of hadronic origin to be identified as a lepton.

685 This requires modification of the jet definition. For each track passing all of the track
686 lepton requirements, but ignoring the isolation requirement, we check whether it is within
687 $\Delta R = 0.4$ of the axis of a jet. Here, we consider all jets from the cone algorithm with
688 $E_T > 10$ GeV. If the track is not matched, we add it to the jet collection. If it is matched, we
689 check whether the p_T of the track exceeds the corrected E_T of the jet. If it does, we substitute
690 the kinematic information of the track for the kinematic information for the jet. If the p_T of
691 the track is less than the corrected E_T of the jet, we leave the jet kinematic information as
692 is. Inclusion of track information in this manner ensures counting of the products of parton
693 fragmentation where most of the momentum is carried by a single charged particle which
694 does not deposit all of its energy in the hadronic calorimeter. In extreme cases, jet energy

695 corrections will not account for all of the unmeasured energy and the track momentum is
 696 the best measure of the parton energy.

697 The final jet collection thus includes standard jets clustered with a cone size of 0.4, jets
 698 with kinematic information from tracks, and unaffiliated tracks. For event selection we count
 699 the number of jets with $E_T > 20$ GeV and $|\eta| < 2.0$, excluding those jets within $\Delta R \leq 0.4$ of
 700 either the lepton candidate or the isolated track. When making a $W + \text{jets}$ selection, such
 701 as is used in the fake lepton background estimates for both the pretag and tagged samples,
 702 only the fully reconstructed lepton is excluded from the jet counting.

703 E. Missing Transverse Energy Reconstruction

704 A transverse momentum imbalance in the detector indicates that particles have exited
 705 the detector without interacting. Dilepton $t\bar{t}$ events have two high- p_T neutrinos in the
 706 final state, leading to a considerable amount of \cancel{E}_T in signal events. Figure 2 shows the
 707 simulated \cancel{E}_T distributions for the $t\bar{t}$ signal and some of the backgrounds. Comparison of
 708 these distributions shows that using a \cancel{E}_T threshold to select events reduces the contribution
 709 from many of the backgrounds considered, particularly Drell-Yan events, but is quite efficient
 710 for $t\bar{t}$ events.

711 The missing transverse energy is defined as:

$$\vec{\cancel{E}}_T = - \sum_i E_T^i \hat{n}_i, \quad (3)$$

712 where i is an index that runs over all calorimeter towers with $|\eta| < 3.6$ and \hat{n}_i is a unit
 713 vector perpendicular to the beam axis and pointing at the i^{th} calorimeter tower. The scalar,
 714 \cancel{E}_T , is then defined as $\cancel{E}_T = |\vec{\cancel{E}}_T|$.

715 Some care must be taken with the \cancel{E}_T calculation, because a transverse momentum im-
 716 balance can also be generated by incorrect measurements of objects in the event and the
 717 energy resolution of the calorimeter towers themselves. To reduce the inclusion of events
 718 where the \cancel{E}_T is produced by energy mismeasurements, the \cancel{E}_T is adjusted in those cases
 719 where the calorimeter information is not the best measure of an object's energy.

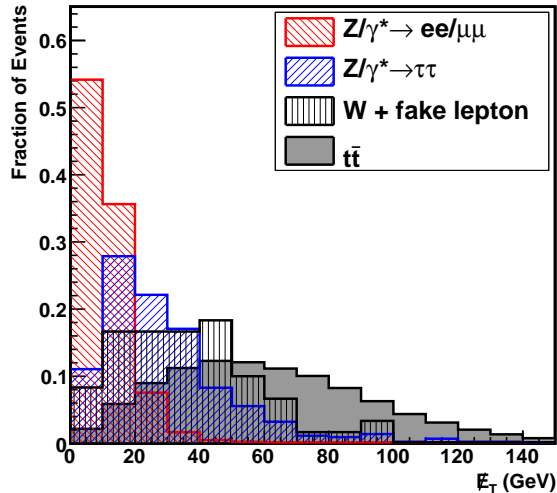


FIG. 2: Corrected missing transverse energy from several lepton + track backgrounds, compared to the $t\bar{t}$ signal. The distribution for WW events is similar to the $t\bar{t}$ distribution but slightly softer, and is omitted for legibility. Candidate events are required to have a fully reconstructed lepton and track and two or more jets, but no other event selection is applied. For the cross section measurements, we require events to have $\cancel{E}_T > 25$ GeV. Distributions taken from events generated with PYTHIA and normalized to have unit area.

720 *1. Muon Correction*

721 Muons are minimum-ionizing particles and deposit very little energy in the calorimeter.
 722 Thus, if the fully reconstructed lepton in the event is a muon (CMUP or CMX), we subtract
 723 the transverse components of the muon momentum from the corresponding components of
 724 the \cancel{E}_T . No correction is made to the calorimeter energy for the small amount of energy
 725 deposited by the muon.

726 *2. Track Correction*

727 We also correct for all tracks (excepting the fully reconstructed lepton if it is a muon)
 728 pointing at a 3 by 3 block of calorimeter towers where the E_T measured is less than 70% of
 729 the p_T of the track. All tracks with $p_T > 10$ GeV/ c , $|d_0| < 250\mu\text{m}$, at least 24 (20) hits on
 730 the axial (stereo) wires of the COT, and appearing to come from the same interaction vertex
 731 ($|\Delta z_0| < 5$ cm) as the primary lepton, are considered. The 70% threshold excludes normal

732 fluctuations in the energy and momentum resolution, so that we correct only for tracks
733 where the energy deposit measured in the calorimeter is clearly not consistent with the
734 momentum measured in the tracker. This correction accounts for tracks pointing at cracks
735 in the calorimeter, minimum-ionizing particles such as muons, and cases where showers
736 produced by hadronic particles in the calorimeters have unusually low light yields.

737 3. *Jet Correction*

738 We also correct the \cancel{E}_T for the jet energy calibrations by subtracting the difference between
739 the corrected and uncorrected jet energies. By doing this we use the best estimate of the
740 energies of those objects which are identifiable as jets. Jets with corrected $E_T > 10$ GeV
741 and $|\eta| < 2.0$ are included, except for objects in the jet collection which are tracks or have
742 had their kinematic information replaced by that of an associated track. These will have
743 already been accounted for in the track correction.

744 F. **Event Selection**

745 1. *Basic event selection*

746 Having defined our basic analysis objects, we can select events with features typical of
747 $t\bar{t}$ dilepton events. First, there must be at least one fully reconstructed electron or muon
748 with $p_T > 20$ GeV/ c in the event. Once a primary lepton is identified, we take as the track
749 lepton the highest p_T isolated track with $p_T > 20$ GeV/ c . To qualify, the track must appear
750 to be from the same interaction vertex as the primary lepton, ($|\Delta z_0| < 5$ cm). If there is
751 no such isolated track, we try the event selection again with the next fully reconstructed
752 lepton, if another has been identified. The leptons are considered in the following order:
753 central (CEM) electrons, CMUP muons, CMX muons, and finally forward (PHX) electrons.
754 Within a particular lepton type, the leptons are tested in order of descending E_T or p_T . In
755 the CDF data, for a lepton of a particular type to be considered, the trigger corresponding
756 to that category must have fired for that event, and the relevant parts of the detector must
757 be known to be fully functional at the time the event occurred.

758 After a track lepton is found, we correct the \cancel{E}_T , and require the corrected \cancel{E}_T to be
759 greater than 25 GeV. Each fully reconstructed lepton in an event is considered in turn until

760 the event has passed all of the selection criteria, or has failed them for all leptons.

761 2. $\Delta\varphi$ Requirements

762 Drell-Yan events may appear to have \cancel{E}_T in spite of the absence of neutrinos in the final
763 state. If the energy of one lepton or jet is measured incorrectly, false \cancel{E}_T appears, pointing
764 along or opposite to the direction of that object. For this reason we require that no lepton
765 or jet in the event be pointing directly at the \cancel{E}_T . The requirements for different objects
766 are determined by their respective angular size and potential for mismeasurement. Studies
767 of Drell-Yan events in simulation show that although \cancel{E}_T may be generated either pointing
768 near or away from a track lepton, most \cancel{E}_T associated with fully reconstructed leptons or
769 jets is pointing in the same direction as the lepton or jet. These studies also show that it is
770 uncommon for \cancel{E}_T associated with a jet to exceed 50 GeV. Therefore, we veto events where
771 the primary lepton points within 5° of the \cancel{E}_T or the track lepton is within 5° of parallel or
772 anti-parallel to the \cancel{E}_T . Also, all jets in the event must be more than 25° away from the
773 direction of the \cancel{E}_T , unless the event has $\cancel{E}_T > 50$ GeV.

774 3. Z Boson Veto

775 To further reduce background from Drell-Yan events, the \cancel{E}_T threshold is raised to 40 GeV
776 if the invariant mass of the lepton + track pair is in the range of the Z boson resonance
777 ($76 \text{ GeV}/c^2 < M < 106 \text{ GeV}/c^2$). This requirement is referred to as the “ Z veto”.

778 4. Candidate Events

779 For the cross section measurements we count events with at least two jets with corrected
780 $E_T > 20$ GeV and $|\eta| < 2.0$. The jets used for this are the extended collection described in
781 Sec. IV D, which is based on a calorimeter clustering algorithm with a cone size of $\Delta R < 0.4$.
782 Any jets within $\Delta R < 0.4$ of either the lepton candidate or the isolated track are excluded
783 from the jet counting. The final requirement is that the fully reconstructed lepton candidate
784 and the track lepton candidate have opposite sign.

785 Applying this selection to 1.1 fb^{-1} of CDF Run II data, we find 129 pretag lepton + track

786 $t\bar{t}$ candidate events with two or more jets.

787 **V. $t\bar{t}$ DILEPTON ACCEPTANCE**

788 We determine the geometric and kinematic acceptance for $t\bar{t}$ dilepton events by applying
789 the lepton + track event selection to the PYTHIA $t\bar{t}$ sample described in Section III. The
790 acceptance is defined as the number of simulated $t\bar{t}$ events passing the selection criteria,
791 divided by the total number of $t\bar{t}$ events in the sample. To be included in the numerator,
792 the event must be identified as a dilepton decay at the generator level, where the W 's may
793 decay to any of $e\nu_e$, $\mu\nu_\mu$, or $\tau\nu_\tau$. Other $t\bar{t}$ events passing the event selection are accounted
794 for as background (see Section VII A). Corrected for discrepancies between observed and
795 simulated data, the acceptance is 0.84 ± 0.03 %, where the uncertainty includes the sys-
796 tematic uncertainties. In the rest of this section, we discuss the acceptance, the corrections
797 made to it, and the systematic uncertainties on it.

798 **A. Contributions to the Acceptance**

799 One of the advantages of identifying the second lepton only as a track is the enhanced
800 acceptance for τ leptons from W decays. Standard electron and muon selection will accept a
801 fraction of τ decays, since 35% are through leptonic channels. There will be some inefficiency,
802 because a portion of the momentum of the original τ will be lost to the two neutrinos
803 produced. On the other hand, if “single-prong” hadronic decays are included, 85% of τ
804 decays have a single charged track in the final state. About 20% of the total lepton + track
805 acceptance is from events where one or both of the W 's decays to a τ lepton, and 65% of
806 that (13% of the total) is from events where at least one of the τ leptons decays hadronically.
807 Table I shows how the acceptance is distributed among the different lepton types.

808 **B. Corrections to the Acceptance**

809 To understand the discrepancies in lepton reconstruction between observed and simulated
810 data, we study the performance of the reconstruction in large control samples and derive
811 appropriate corrections. Real and simulated Z boson events are used, because the available

	ee	$e\mu$	$\mu\mu$	$e\tau$	$\mu\tau$	$\tau\tau$	total
$e+\text{track}$	17.4 ± 0.2	29.5 ± 0.3	0.0 ± 0.0	7.6 ± 0.1	2.3 ± 0.1	0.5 ± 0.0	57.4 ± 0.4
$\mu+\text{track}$	0.0 ± 0.0	5.9 ± 0.1	15.5 ± 0.2	0.5 ± 0.0	4.8 ± 0.1	0.3 ± 0.0	26.9 ± 0.2
total	17.4 ± 0.2	35.4 ± 0.3	15.5 ± 0.2	8.1 ± 0.1	7.1 ± 0.1	0.8 ± 0.0	84.3 ± 0.5

TABLE I: Acceptance for opposite-charge lepton + track events with two or more jets, for each possible pairing of generated charged leptons from the W decays. Numbers have been multiplied by 10000 for legibility. The first row shows the acceptance in the channels where the fully reconstructed lepton is an electron, and the second row shows the acceptance for the fully reconstructed muon channels. The majority of events are accepted as electron plus track because there is more geometric acceptance for electrons, and because the ordering of primary leptons means that events generated as electron-muon events will be preferentially accepted as electron+track. The uncertainties quoted only include the statistical uncertainty.

812 samples are large and the reconstruction of the invariant mass peak allows selection of a
813 very pure sample of dilepton events, even with minimal identification requirements placed
814 on the second lepton. We also correct the acceptance for the small inefficiency of the high- p_T
815 lepton triggers.

816 These corrections are also used in some of the background calculations.

817 1. Trigger Efficiencies

818 We measure single lepton trigger efficiencies with a combination of Z data and data taken
819 using an independent trigger. The Z sample is especially useful when the two lepton candi-
820 dates are found in sections of the detector corresponding to different triggers. Independent
821 triggers designed to share some, but not all, of the requirements of the trigger of interest
822 enable measurement of the efficiency of the omitted requirements.

823 What we need for the cross section measurements is the probability for a lepton + track
824 candidate to fire one of the high- p_T lepton triggers. This probability is higher than the single
825 lepton trigger efficiency since each event has two chances to fire one of the triggers, one for
826 each lepton. On the other hand, the second lepton is not fully reconstructed in our event
827 selection, so the event trigger efficiency is not just a simple combination of single-lepton

828 trigger efficiencies. To determine the per-event trigger efficiency for a particular process
829 and fully reconstructed lepton type, we count the number of events in a simulated sample
830 of that process that have one lepton of that type and the number with two of that type.
831 For events with one fully reconstructed lepton, we use the single-lepton trigger efficiency
832 as the event trigger efficiency. For events with two, we use the probability for at least one
833 of the two leptons to fire the trigger, given by $1 - (1 - \epsilon)^2$ where ϵ is the single-lepton
834 trigger efficiency. We then take the average of the two per-event efficiencies, weighted by the
835 relative number of events with one and two fully reconstructed leptons. The plug electron
836 trigger also includes a \cancel{E}_T threshold, so the trigger efficiency we use for those events also
837 depends on the value of the \cancel{E}_T as it would be calculated for the trigger decision. Note that
838 we include the electron E_T and \cancel{E}_T dependence of the trigger efficiencies where applicable,
839 by convoluting the single-lepton trigger efficiencies with the E_T and or \cancel{E}_T distributions for
840 the class of events in question.

841 The per-event trigger efficiency is also needed for background estimates that use an
842 acceptance calculated from simulation. For a given lepton type, the per-event efficiencies
843 are very similar across different physics processes, so the $t\bar{t}$ value is used. The one exception
844 is PHX + track $Z/\gamma^* \rightarrow \tau\tau$ events. For those events the typical plug electron E_T and \cancel{E}_T
845 fall in the middle of the turn-on curves for the trigger, and the trigger efficiency, about 66%,
846 is lower than those typical of $t\bar{t}$ and diboson events.

847 The single-lepton and total per-event trigger efficiencies are given in Table II.

848 2. Fully Reconstructed Electrons and Muons

849 Identification efficiencies for fully reconstructed leptons are measured in a sample of Z
850 candidates. These candidates consist of one fully reconstructed lepton candidate and one
851 opposite-charge lepton candidate of the same flavor which meets minimal kinematic and
852 identification criteria. The fully reconstructed candidate must pass the corresponding high-
853 p_T lepton trigger, and the invariant mass of the lepton candidate pair is required to be close
854 to the central value of the Z resonance peak.

855 For central (CEM) electrons, the minimally-identified lepton candidate is an electromag-
856 netic cluster fiducial to the central calorimeter with $E_T > 20$ GeV and a matched track
857 with $p_T > 10$ GeV/ c and $|z_0| < 60$ cm. The electron candidate pair must have an invariant

858 mass in the interval $76 \text{ GeV}/c^2 < M < 106 \text{ GeV}/c^2$. Electromagnetic clusters fiducial to the
 859 forward calorimeter are used to measure the forward (PHX) electron efficiency. No track re-
 860 quirement is made, so the efficiencies measured include the tracking efficiency. The invariant
 861 mass window used for this candidate pair is $81 \text{ GeV}/c^2 < M < 101 \text{ GeV}/c^2$.

862 For muons, the total reconstruction efficiency is the product of the efficiency to find a
 863 track stub in the muon chambers and the efficiency for a muon candidate with a track and
 864 stub to pass all of the remaining identification requirements. To measure the efficiency
 865 to find a track stub, the second muon candidate in the Z pair is a track pointing at the
 866 fiducial region of the muon detectors and meeting the same requirements on the energy
 867 deposition in the calorimeter as fully reconstructed muon candidates, except with the maxi-
 868 mum scaled up by 50%. To measure the identification efficiency, the second muon candidate
 869 is a track with $p_T > 20 \text{ GeV}/c$ matched to a track stub in the CMU and CMP, or in the
 870 CMX. We accept only events where the muon candidate pair invariant mass is in the range
 871 $81 \text{ GeV}/c^2 < M < 101 \text{ GeV}/c^2$.

872 The denominator of the efficiency is the number of leptons in the Z candidates passing
 873 the minimal requirements, and the numerator is the subset of those also passing all lepton
 874 selection requirements. We measure the efficiency in both observed and simulated data,
 875 because the full lepton selection is applied in calculating the acceptance. We therefore use
 876 the ratio of the efficiency in observed data to the efficiency in simulated data as a “scale
 877 factor” which is multiplied by the acceptance to correct it. Scale factors for the four primary
 878 lepton types are given in Table II.

879 3. *Track χ^2 Probability*

880 The χ^2 probability requirement, imposed on fully reconstructed muons and on track
 881 leptons, is intended to reject hadron decays-in-flight that can be mistaken for prompt high-
 882 p_T muons. Tracks reconstructed from a particle that decays in the tracker have a worse
 883 track fit because the track is constructed from hits from both the original hadron and the
 884 secondary muon, some of which will be far from the single reconstructed trajectory.

885 Because the requirement is made only in observed data, the acceptance is multiplied by
 886 the efficiency as measured in observed data, rather than by a scale factor. We measure this
 887 efficiency in a sample of Z candidates identified from a fully reconstructed lepton and an

888 isolated track. One subtlety here is that the χ^2 is correlated between the tracks of the two
 889 objects, through the hit timing information in the COT, so the efficiency to apply it to both
 890 is not equal to the product of efficiencies of the individual objects. Thus, for electron + track
 891 events, where the requirement applies only to the track lepton, the efficiency is the number
 892 of tracks that pass the requirement, divided by the total number of tracks. In contrast, for
 893 muon + track events, where the requirement applies to both, the relevant efficiency is the
 894 ratio of muon + track Z events where both leptons pass the requirement to all muon+track Z
 895 events. The measured efficiencies are 0.962 ± 0.001 for electron+track events, 0.944 ± 0.001
 896 for CMUP + track events, and 0.951 ± 0.002 for CMX + track events, and are included in
 897 Table II.

898 *4. Isolated Tracks*

899 Efficiencies for the track isolation and impact parameter requirements differ between
 900 observed and simulated data. To quantify the efficiency of the track isolation requirement,
 901 we use Z candidates from a fully reconstructed electron or muon and an opposite-charge track
 902 passing all of the track lepton requirements except isolation, where the lepton + track pair
 903 have an invariant mass in the interval $76 \text{ GeV}/c^2 < M < 106 \text{ GeV}/c^2$. To reduce background
 904 from jets, we accept only events where the track appears to be from a lepton of the same
 905 flavor as the fully reconstructed one, using information from the calorimeter towers at which
 906 the track points. The efficiency of the isolation requirement is the ratio of the number of
 907 tracks passing it to the total number of tracks. The efficiencies drop from about 95% for
 908 events with zero jets to about 90% for events with two or more jets. Taking the ratio of
 909 the efficiency from observed data to the efficiency from simulated data, the resulting scale
 910 factors are 1.004 ± 0.001 for events with zero jets, 1.002 ± 0.003 for events with one jet,
 911 and 0.965 ± 0.011 for events with two or more jets.

912 We measure the efficiency of the impact parameter requirement similarly. The total
 913 observed efficiency in data is 0.909 ± 0.003 , calculated as the weighted combination of
 914 0.940 ± 0.002 for data including silicon detector information and 0.53 ± 0.02 for the rest of
 915 the data. The corresponding efficiency is 0.9185 ± 0.0007 in simulation: 0.947 ± 0.001 for
 916 data including silicon detector information and 0.55 ± 0.01 for the rest of the data. Taking
 917 the ratio of the results yields a scale factor of 0.989 ± 0.003 .

Event type	Reconstruction scale factor	χ^2 probability efficiency	Single lepton trigger efficiency	Event trigger efficiency
CEM + track	0.981	0.962	0.971	0.975
PHX + track	0.935	0.962	0.918*	0.918
CMUP + track	0.926	0.944	0.908	0.916
CMX + track	0.984	0.951	0.910	0.937

TABLE II: Correction factors applied to the calculated acceptance. Uncertainties on these numbers are about a percent or smaller. CEM and PHX are the central and forward electrons, and CMUP and CMX are muons. The χ^2 probability efficiency applies to just the isolated track in electron + track events, but to both the muon and the isolated track in muon + track events. *For the forward (PHX) electron trigger, this efficiency is for W events, since the trigger also has a \cancel{E}_T requirement. This also means that the per-event efficiency is identical to the single-lepton efficiency.

C. Systematic Uncertainties on Acceptance

The systematic uncertainties on the acceptance reflect the limits on experimental understanding of the final-state objects used to identify $t\bar{t}$ events, as well as our ability to model $p\bar{p}$ interactions with Monte Carlo simulations. The first category includes uncertainties on lepton identification and the jet energy scale. The second includes uncertainties on QCD radiation, parton density functions, and the Monte Carlo generator used to calculate the acceptance.

The systematic uncertainties on the signal acceptance are discussed individually below and summarized in Table III.

1. Primary Lepton Identification Efficiency

The dominant uncertainty on the identification efficiency for fully reconstructed leptons is associated with isolation and our ability to model additional activity in the event, such as jets or unclustered low- p_T tracks, using Monte Carlo simulations. As described in Section V B, the lepton identification efficiencies are derived from real and simulated Z data, in which most events have zero jets. In the $t\bar{t}$ sample, where most events have two or more jets, and

Source	Uncertainty
Fully rec. lepton identification	1.1%
Track lepton identification	1.1%
Jet energy scale	1.3%
Initial-state QCD radiation	1.6%
Final-state QCD radiation	0.5%
Parton density functions	0.5%
Monte Carlo generator	1.5%
Total	3.1%

TABLE III: Summary of systematic uncertainties on the signal acceptance.

933 nearby jet activity can reduce the efficiency to identify isolated electrons and muons.

934 To quantify these effects, we measure the scale factor in the Z samples as a function
935 of the distance ΔR between the lepton candidate and the nearest jet. We calculate the
936 correction appropriate to $t\bar{t}$ events by folding this function with the ΔR distribution for
937 simulated $t\bar{t}$ candidate events. For each primary lepton type, the statistical uncertainty on
938 the re-weighted scale factor exceeds the difference between the original and re-weighted scale
939 factors. Therefore, we take the statistical uncertainties on the re-weighted scale factors as the
940 uncertainties on the scale factors. The total systematic uncertainty is the weighted average
941 of the uncertainties on the individual lepton types, where the weights are the acceptances
942 for each lepton category. The resulting uncertainty is 1.1%.

943 2. Track Lepton Identification Efficiency

944 This uncertainty quantifies how well the simulation models the track isolation requirement
945 in an environment with many jets, in analogy to the uncertainty on well-reconstructed
946 leptons. In this case, we base the uncertainty on the behavior of the correction as a function
947 of the number of jets. We correct the acceptance with the scale factor measured in events
948 with two or more jets, and take the 1.1% statistical uncertainty as the uncertainty on track
949 lepton identification.

950 *3. Jet Energy Scale*

951 The jet energy scale influences the $t\bar{t}$ acceptance because if the jet energies are over-
952 corrected, more events will have two or more jets and pass the event selection, and vice
953 versa. It also influences the acceptance through the jet energy corrections to the \cancel{E}_T and
954 the restriction on the $\Delta\varphi$ between the jets and the \cancel{E}_T for events with $\cancel{E}_T < 50$ GeV. To
955 estimate the uncertainty on the acceptance from the jet energy scale, we recalculate the
956 signal acceptance twice. First, we vary the jet energy corrections up by the uncertainties
957 from Ref. [49] and recalculate the energies of all the jets in the event, and then recalculate
958 the acceptance. We repeat the exercise, varying the jet energies down by their uncertainties,
959 and then take half the difference between the two recalculated acceptances, 1.3%, as the
960 systematic uncertainty.

961 *4. Initial and Final State Radiation*

962 Additional jets can be produced in association with the $t\bar{t}$ pair through radiation of one or
963 more gluons from the initial or final state particles. We can measure the dependence of the
964 acceptance on the rate of QCD radiation by comparing the central value of the acceptance
965 to values calculated in simulated PYTHIA $t\bar{t}$ samples identical to those used to calculate the
966 central value, except that the PYTHIA parameters governing the rate of initial and final state
967 radiation via parton showering have been varied. The range of allowed values is set by study
968 of the reconstructed p_T and M^2 of the Z/γ^* in Drell-Yan events with electrons or muons in
969 the final state [50]. Drell-Yan events allow isolation of initial-state radiation effects, because
970 the dilepton final state is colorless. The range of parameters found to cover the variation
971 in the observed initial-state radiation can then also be used to generate samples with more
972 and less final-state radiation, because the same parton shower algorithm is used.

973 The acceptance increases for the sample with more initial-state radiation, and decreases
974 for the sample with less. We take half the full difference, 1.6%, as the systematic uncertainty.
975 The results for final-state radiation are less conclusive, as the measured acceptances in the
976 modified samples differ from the nominal value by less than their statistical uncertainties of
977 1%. We therefore take the larger of the two observed differences, 0.5%, as the systematic
978 uncertainty.

980 The parton distribution functions (PDFs) describe the probabilities for each type of
 981 parton to carry a given fraction of the proton momentum. Variations of the PDFs can have
 982 a significant effect on the $t\bar{t}$ cross section [8]. The PDFs also have a smaller effect on the
 983 acceptance through the kinematics of the $t\bar{t}$ decay products. Twenty independent sources of
 984 uncertainty identified for the CTEQ5L PDF set are considered [44]. In evaluating the total
 985 uncertainty, we also include the difference between the CTEQ5L and MRST [51] PDF sets and
 986 the effect of lowering $\alpha_s(M_Z^2)$ from the preferred value of 0.1175 by 0.005, the uncertainty
 987 on the world average measured value at the time the PDF set was calculated [52].

988 To quantify the effect of PDFs on the lepton + track acceptance, we recalculate the
 989 acceptance twice for each variable of interest: once each for the upper and lower bounds on
 990 that variable. Information about the types and momenta of generated particles are stored
 991 when Monte Carlo events are produced, allowing the incoming partons and their momenta
 992 to be identified. The corresponding probabilities for those values are found in both the
 993 nominal PDF and the variation under study. The event weight is the ratio of the product
 994 of the altered probabilities to the nominal:

$$\text{weight} = \frac{p(x_1, Q^2) p(x_2, Q^2)}{p'(x_1, Q^2) p'(x_2, Q^2)}, \quad (4)$$

995 where p is the nominal PDF and p' is the modified PDF. The PDFs depend on the momentum
 996 transfer Q and the fraction x_i of the hadron's momentum carried by the parton, where the
 997 index i specifies one of the two incoming partons. To calculate the acceptance as a ratio of
 998 accepted to total events, each event contributes the calculated weight to the denominator of
 999 the ratio but the weight is only added to the numerator if the event passes the selection. We
 1000 repeat this process for each PDF variation and record the resulting change in acceptance.
 1001 Adding the results of all the variations in quadrature and averaging the positive and negative
 1002 uncertainties, we find a total uncertainty of 0.5%.

1003 6. Monte Carlo Generator

1004 To account for a possible dependence of the measured acceptance on the choice of Monte
 1005 Carlo event generator, the $t\bar{t}$ acceptance is remeasured, again for $m_t = 175 \text{ GeV}/c^2$, using the
 1006 HERWIG Monte Carlo and compared to the nominal value obtained using the PYTHIA Monte

1007 Carlo. In calculating the difference, we exclude the effect of the different $W \rightarrow \ell\nu$ branching
1008 ratios used by the two generators: PYTHIA uses the measured value, 0.1080 ± 0.0009 ([4]),
1009 and HERWIG uses $1/9$. The remaining difference between the acceptances measured with
1010 the two generators is 1.5%, which we include as a systematic uncertainty.

1011 VI. IDENTIFICATION OF JETS FROM b QUARKS

1012 The CDF SECVTX algorithm identifies b -jet candidates based on the determination of the
1013 primary event vertex and the reconstruction of one or more secondary vertices using dis-
1014 placed tracks associated with jets [53, 54]. If a secondary vertex is found that is significantly
1015 displaced from the primary vertex in the plane transverse to the beam, the jet is said to be
1016 “tagged” as a b -jet candidate.

1017 A. Determination of the Primary Vertex

1018 A primary vertex in an event is defined as the point from which all prompt tracks origi-
1019 nate. The location of the primary vertex in an event can be found by fitting well-measured
1020 tracks to a common point of origin. In high instantaneous luminosity conditions, more than
1021 one primary vertex may exist in an event, but these are typically separated in z . The z
1022 coordinate for each vertex is found by taking the weighted average of the z coordinates of
1023 all tracks within 1 cm of the first iteration vertex. The z position measurement of this
1024 first vertex has a resolution of $100 \mu\text{m}$ [53, 54]. The location of the primary vertex is then
1025 refined by the above information, along with constraints of the beamline position, and some
1026 tracking information.

1027 B. The SECVTX Algorithm

1028 The SECVTX algorithm starts from the primary interaction vertex for each event. In
1029 the present application, this is the vertex that is associated with the lepton + track. It
1030 then examines the tracks associated with each jet and applies basic quality criteria to them.
1031 These include the number of silicon layers associated with the track, minimum and maximum
1032 allowed impact parameters, and the track χ^2 per degrees of freedom. The algorithm then

1033 attempts to resolve a secondary vertex that is significantly displaced from the primary vertex
 1034 using tracks with large impact parameter significance, d_0/σ_{d_0} , where σ_{d_0} is the uncertainty
 1035 on the impact parameter.

1036 The SECVTX algorithm is based on a two-pass system. The first pass of the algorithm
 1037 builds an initial vertex, known as the “seed”, from the two most displaced tracks. The seed
 1038 vertex initiates the SECVTX algorithm. Pairs of tracks with invariant masses consistent with
 1039 the K_s^0 and Λ mass are removed from the track list. The algorithm then seeks to add tracks
 1040 to the seed vertex. The additional tracks must pass quality requirements on the impact
 1041 parameter and p_T and must not result in a poor χ^2 for the resulting three track vertex. If no
 1042 such vertex is found, then another seed vertex, made of the next two most displaced tracks
 1043 is tried. This continues until a vertex is resolved, or the seed list is exhausted. In the latter
 1044 case, the algorithm moves on to the second pass, in which it attempts to find a vertex using
 1045 only two tracks for which the quality requirements of the tracks are made more stringent.
 1046 Again, pairs of tracks whose invariant mass is consistent with the K_s^0 and Λ masses are
 1047 removed.

1048 With a secondary vertex in hand, SECVTX calculates the length of the vector between
 1049 the primary and secondary vertices in the plane perpendicular to the beamline. This vector
 1050 is then projected onto the jet axis:

$$L_{xy} = (\vec{r}_{\text{PV}} - \vec{r}_{\text{SV}}) \cdot \hat{p}_{\text{jet}}, \quad (5)$$

1051 where \vec{r}_{PV} is the position of the primary vertex, \vec{r}_{SV} is the position of the secondary vertex,
 1052 and \hat{p}_{jet} is the jet direction. L_{xy} is the two-dimensional decay length along the jet axis, and
 1053 $\sigma_{L_{xy}}$ the associated uncertainty. SECVTX defines a “displaced” (or “tagged”) vertex as one
 1054 with significance $|L_{xy}/\sigma_{L_{xy}}| > 3.0$. A long-lived hadron will generally travel in roughly the
 1055 same direction as the jet formed from the fragmentation and hadronization process. As a
 1056 result, the cosine of the angle between the jet axis and the vector extending from the primary
 1057 to the secondary vertex will be positive, and so will L_{xy} ; see Fig. 3. A negative value of
 1058 L_{xy} can result from resolution smearing of the track parameters and poorly reconstructed
 1059 tracks. Depending on the sign of L_{xy} , tags will be referred to as *positive* or *negative*. The
 1060 L_{xy} distribution for negative tags will be interpreted as the result of “mistags”, or tags from
 1061 non- b -jets.

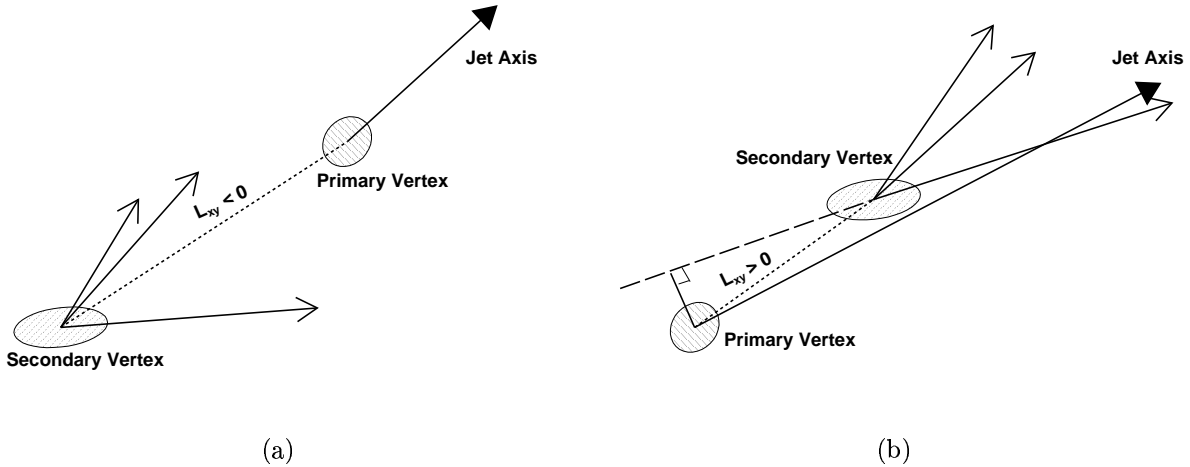


FIG. 3: Drawing showing reconstructed secondary vertices, illustrating example cases where (a) $L_{xy} < 0$ and (b) $L_{xy} > 0$.

C. Event Tagging Efficiency

The event tagging efficiency is the efficiency for tagging at least one of the two b -jets in a $t\bar{t}$ lepton + track event using the SECVTX tagger. To find the event tagging efficiency we use a $t\bar{t}$ PYTHIA Monte Carlo sample with $m_t = 175 \text{ GeV}/c^2$, the same sample used to calculate the pretag acceptance. Corrections to the event tagging efficiency are made for two effects. The first correction accounts for our ability to reconstruct jets which correspond to a B hadron decay. The second correction is for the possibility of mistakenly tagging light quark jets as heavy flavor jets.

The event tagging efficiency is given by the formula

$$\epsilon_{\text{tag}} = \epsilon'_b F_{1b} + 2\epsilon'_b(1 - \epsilon'_b) F_{2b} + (\epsilon'_b)^2 F_{2b}. \quad (6)$$

where ϵ'_b is the corrected single jet tagging efficiency (see below), and F_{1b} and F_{2b} are the taggable jet fractions. The taggable jet fractions describe the fraction of events with one or two jets which originate with the hadronization of a b quark and might be tagged. The denominator contains events from the simulated $t\bar{t}$ sample which pass the lepton + track selection, including the ≥ 2 jet requirement. The numerator of F_{1b} is the number of those which have one jet which is matched to a b hadron at generator level and contains two or more tracks passing the SECVTX quality requirements described in Section VI B. The numerator of F_{2b} is the number with two such jets. See Table IV for the values of the

1079 taggable jet fractions.

1080 The single jet tagging efficiency ϵ_b is the ratio of the number of taggable jets with a
1081 positive SECVTX tag to the number of taggable jets. We multiply ϵ_b by a scale factor, ϵ_{SF} to
1082 account for differences in the single jet tagging efficiency between observed and simulated
1083 data. We also apply corrections for the efficiency to tag light quark jets ϵ_q , and the efficiency
1084 to match a jet to a b hadron decay ϵ_{bmatch} . The corrected single jet tagging efficiency is:

$$\epsilon'_b = \frac{\epsilon_b \epsilon_{\text{SF}} \epsilon_{\text{bmatch}}}{(1 - \epsilon_q)}. \quad (7)$$

1085 The ϵ_{bmatch} correction accounts for the situation in which a b quark fragments to produce
1086 a jet which does not pass the jet selection criteria employed in this analysis. We measure
1087 the efficiency for matching a B hadron to a reconstructed jet in simulated $t\bar{t}$ events. We find
1088 $\epsilon_{\text{bmatch}} = (98.89 \pm 0.04) \%$. We multiply the per jet tagging efficiency obtained above by the
1089 matching efficiency to account for this small b -jet reconstruction inefficiency.

1090 The last correction, $1/(1 - \epsilon_q)$, accounts for tags of light quark jets, which results in an
1091 enhancement to the single jet tagging efficiency. As stated in Section VIB, negative tags
1092 are interpreted as mistakes made by the tagging algorithm, and are due to resolution effects.
1093 The negative tagging rate is similar for long-lived b -jets and for light quark jets. So, to find
1094 the efficiency for tagging light quark jets in $t\bar{t}$ decays, we find the efficiency for negative tags
1095 in b -jets in PYTHIA $t\bar{t}$ simulation events, which is equivalent to the rate of tagging of light
1096 quark jets. We find $\epsilon_q = (1.3 \pm 0.1) \%$. To correct the single jet tagging efficiency for the
1097 tagging of light quark jets we divide by $(1 - \epsilon_q)$.

1098 Table IV gives a summary of the inputs used to calculate the final event tagging efficiency
1099 and we obtain a value of 0.669 ± 0.037 . This translates into 5.5% systematic uncertainty due
1100 to event tagging.

1101 Applying the SECVTX tagging algorithm to the jets in the 129 lepton + track candidates,
1102 we find 69 events with one or more tagged jets.

1103 VII. BACKGROUND ESTIMATION IN PRETAG SAMPLE

1104 Background events in the $t\bar{t}$ dilepton sample generally have one or two massive vector
1105 bosons decaying to leptons. Non-negligible background processes are W + jets and similar
1106 events where one of the jets is misidentified as a lepton, diboson production, and Drell-Yan

Quantity	Value
F_{1b}	0.321 \pm 0.003
F_{2b}	0.611 \pm 0.003
ϵ_b	0.591 \pm 0.002
ϵ_{SF}	0.94 \pm 0.06
ϵ_q	0.013 \pm 0.001
ϵ_{bmatch}	0.9889 \pm 0.0004
ϵ_{tag}	0.669 \pm 0.037

TABLE IV: Inputs and results of calculation of event tagging efficiency. Note that the uncertainty on the event tagging efficiency is dominated by the systematic uncertainty on ϵ_{SF} . The other quoted uncertainties are all statistical uncertainties from simulation and are negligible.

1107 events where \cancel{E}_T is produced by a combination of τ decays and the mismeasurement of the
1108 energy of one or more objects in the event. Each of these processes requires the production
1109 of extra jets to satisfy event selection criteria.

1110 A. Backgrounds with a Jet Misidentified as a Lepton (“Fakes”)

1111 $W \rightarrow \ell\nu$ events with extra jets can pass the lepton + track selection if one of the jets
1112 is misidentified as a lepton. This can happen if the fragmentation of a parton results in a
1113 single charged hadron carrying most of the momentum of the original parton. If a single
1114 charged particle carries more than about 90% of the total momentum of all the charged
1115 particles produced by fragmentation, it may satisfy the criteria for an isolated track. This is
1116 a relatively rare occurrence, but the inclusive W cross section times the branching ratio to
1117 leptons is about 2700 pb [28], as compared to the 6.7 pb cross section for $t\bar{t}$ production. Even
1118 though only about one in 500 W +jets events will have enough (three) jets to produce a fake
1119 lepton and still pass the event selection, it remains the largest single source of background
1120 events.

1121 The estimation of the background from events with a fake lepton has three primary com-
1122 ponents: the rate for the production of W + jets events with the right kinematic features,
1123 the probability for a jet to be misidentified as a lepton (the “fake rate”), and the fraction of

1124 events in which the fake and true leptons have opposite charge. All present difficulties for the
 1125 simulation of physics events. The rate for the production of multiple extra jets in addition
 1126 to a vector boson can in principle be calculated perturbatively, but for large numbers of jets,
 1127 the complexity of the calculation grows prohibitively, although progress has been made in
 1128 recent years [43]. The fake rate is affected by parton fragmentation, a non-perturbative QCD
 1129 process which is not currently modeled with the needed accuracy. The fragmentation model
 1130 will also affect the predicted charge correlation between the true and fake leptons. Inaccura-
 1131 cies in the detector simulation further complicate the picture. Therefore, we rely primarily
 1132 on observed events for the estimate of the fake lepton background, and use simulated events
 1133 only when it is impossible to isolate the relevant effect in data.

1134 We summarize the calculation of the expected number of background events before de-
 1135 scribing the individual components in detail. The total number of lepton + track events
 1136 with n jets where one of the leptons is fake, N_{fake}^n , is the sum of the number of events N_t^n
 1137 with a fake track lepton and the number N_ℓ^n with a fake fully reconstructed lepton, where we
 1138 use the subscript t to indicate numbers relating to track leptons and ℓ to indicate numbers
 1139 relating to fully reconstructed leptons. The estimates N_t^n and N_ℓ^n are calculated separately
 1140 using similar procedures, and then corrected for the efficiencies ϵ_{OS}^n and ϵ_Z^n (explained in
 1141 more detail at the end of this section) of the remaining lepton + track event selection:

$$N_{\text{fake}}^n = \epsilon_{\text{OS}}^n \epsilon_Z^n (N_t^n + N_\ell^n) \quad (8)$$

1142 where

$$N_t^n = \sum_{E_T, |\eta|} \left(f_t^{(n+1)}(E_T, |\eta|) \right) \left(N_j^{(n+1)}(E_T, |\eta|) \right) \quad (9)$$

1143 and

$$N_\ell^n = \sum_{i=1}^4 \sum_{E_T, |\eta|} \left(f_\ell^i(E_T, |\eta|) \right) \left(N_j^{(n+1)}(E_T, |\eta|) \right) (A_\ell^i/A_t) . \quad (10)$$

1144 To predict the number of events N_t^n with n jets and a fake track lepton, we multiply the
 1145 number of jets $N_j^{(n+1)}(E_T, |\eta|)$ in the lepton + $\cancel{E}_T + (n+1)$ jet sample, binned in jet E_T and
 1146 $|\eta|$, by the track lepton fake rate $f_t^{(n+1)}(E_T, |\eta|)$ for the same number of jets and range of jet
 1147 E_T and $|\eta|$. The result is summed over jet E_T and $|\eta|$. The selection for lepton + \cancel{E}_T + jets
 1148 events is described in Section VII A 1, and the fake rate for track leptons is defined in
 1149 Sections VII A 3 and VII A 4 after motivating the choice of the γ + jets sample for the fake
 1150 rate calculation in Section VII A 2. We test the performance of the track lepton fake rate by

1151 comparison among relevant jet samples in Section VII A 5. To include the contribution from
 1152 events with a fake fully reconstructed lepton, N_ℓ^n , we multiply the same jet distributions
 1153 $N_j^{(n+1)}(E_T, |\eta|)$ by the fully reconstructed lepton fake rates f_ℓ^i , where the index i indicates the
 1154 type of the lepton identification criteria, and both the fake rate and jet counts are binned in
 1155 jet E_T and $|\eta|$ as for the fake track leptons. This yields the predicted numbers of events with
 1156 two fully reconstructed leptons where one is real and one is fake. We rescale the result by
 1157 the ratio of the $W \rightarrow \ell\nu + \text{jets}$ acceptance A_t for track leptons to the acceptance A_ℓ^i for fully
 1158 reconstructed lepton type i , to find the number where the track lepton is the lepton from
 1159 the W and the fully reconstructed lepton is fake. Summing over the four fully reconstructed
 1160 lepton types (i runs from 1 to 4) gives the total result. Details on the inclusion of fake fully
 1161 reconstructed leptons are given in Section VII A 6.

1162 The dominant contribution to the lepton + \cancel{E}_T + jets sample is $W + \text{jets}$, but for the
 1163 sample with three or more jets, which is used in the background prediction for the cross
 1164 section measurement, there is also a significant contribution from $t\bar{t}$. This happens in the
 1165 “lepton + jets” decay channel, in which the W that decays to a pair of quarks adds one or
 1166 two jets to the final state in addition to the two jets from the b quarks. If the lepton from the
 1167 decay of the other W is reconstructed as an electron or muon and one of the jets in the final
 1168 state produces an isolated track (or vice versa), such events can pass the full lepton + track
 1169 event selection. The treatment of the $t\bar{t}$ contribution to the candidates with a fake lepton
 1170 is discussed in Section VII A 7. These events require some special care, as they introduce a
 1171 dependence on the cross section we are measuring. That is treated by explicitly including
 1172 the dependence in the likelihood used to calculate the cross section (see Section IX A).

1173 The remaining component of the estimate is the efficiency for the selection criteria that
 1174 cannot be applied in selecting the lepton + \cancel{E}_T + jets sample. First is the opposite-charge
 1175 requirement. We calculate the efficiency ϵ_{os}^n for this requirement using a combination of
 1176 observed data and Monte Carlo simulations in Section VII A 8. The other two requirements
 1177 are the increased \cancel{E}_T threshold for events with a lepton + track invariant mass close to
 1178 the Z resonance, and the track lepton- \cancel{E}_T opening angle veto. The efficiencies for these,
 1179 collectively labeled ϵ_Z^n in Eq. 8, are given in Section VII A 9.

1180 Finally, we tally the systematic uncertainties on this background estimate in Sec-
 1181 tion VII A 10.

1182 *1. Selection of $W + jets$ Events*

1183 The selection for $W + jets$ events in the data is based on the event selection described in
1184 Section IV, with all requirements involving the track lepton omitted. That is, we select events
1185 from the same high- p_T electron and muon trigger sample containing the signal candidates,
1186 with one fully reconstructed electron or muon. We also require that these events have
1187 $\cancel{E}_T > 25$ GeV and pass the $\Delta\varphi$ criteria for the fully reconstructed lepton and the jets. Since
1188 one of the jets will be reconstructed as a lepton in events with a fake lepton, we predict the
1189 number of events passing the full lepton + track selection and having N jets by using events
1190 with $N + 1$ jets. We count the number of events with one jet, two jets, or at least three jets.

1191 The largest contribution to this sample is $W + jets$, where the W decays leptonically.
1192 There is also a significant contribution from $t\bar{t}$, which will be discussed in more detail below.
1193 There is also a small contribution from pure-QCD multijet events where one of the jets has
1194 been wrongly identified as a fully reconstructed electron or muon.

1195 *2. Jet Properties Influencing the Fake Rate*

1196 To motivate the choice of the $\gamma + jets$ sample for the fake rate, we focus our attention on
1197 the largest contribution to the fake lepton background, $W + jets$ events. The lepton fake
1198 rate is determined by parton fragmentation, and fragmentation is determined by the energy
1199 and type of the parton. The energy dependence will be included by parameterizing the fake
1200 rate as a function of jet E_T and $|\eta|$. Here we consider the possible influence of the parton
1201 type.

1202 A jet produced in association with a W has a higher probability of being a quark jet,
1203 meaning a jet which originates from a quark, than a jet of the same energy produced in a
1204 generic QCD multijet event. To understand this, note that most W and multijet produc-
1205 tion at the Tevatron takes place at relatively low x , where x is the fraction of the proton
1206 momentum carried by an individual parton. For Q^2 values typical of $W + jets$ or multijet
1207 production at the Tevatron, the gluon PDF is strong relative to the valence quark PDFs for
1208 $x \lesssim 0.15$. The two leading diagrams for $W + 1$ jet production (see Fig. 4) at the Tevatron
1209 have the same amplitude. The preference for diagrams with incoming gluons implies that
1210 the diagram with an outgoing quark will prevail, so the jets associated with a W boson are

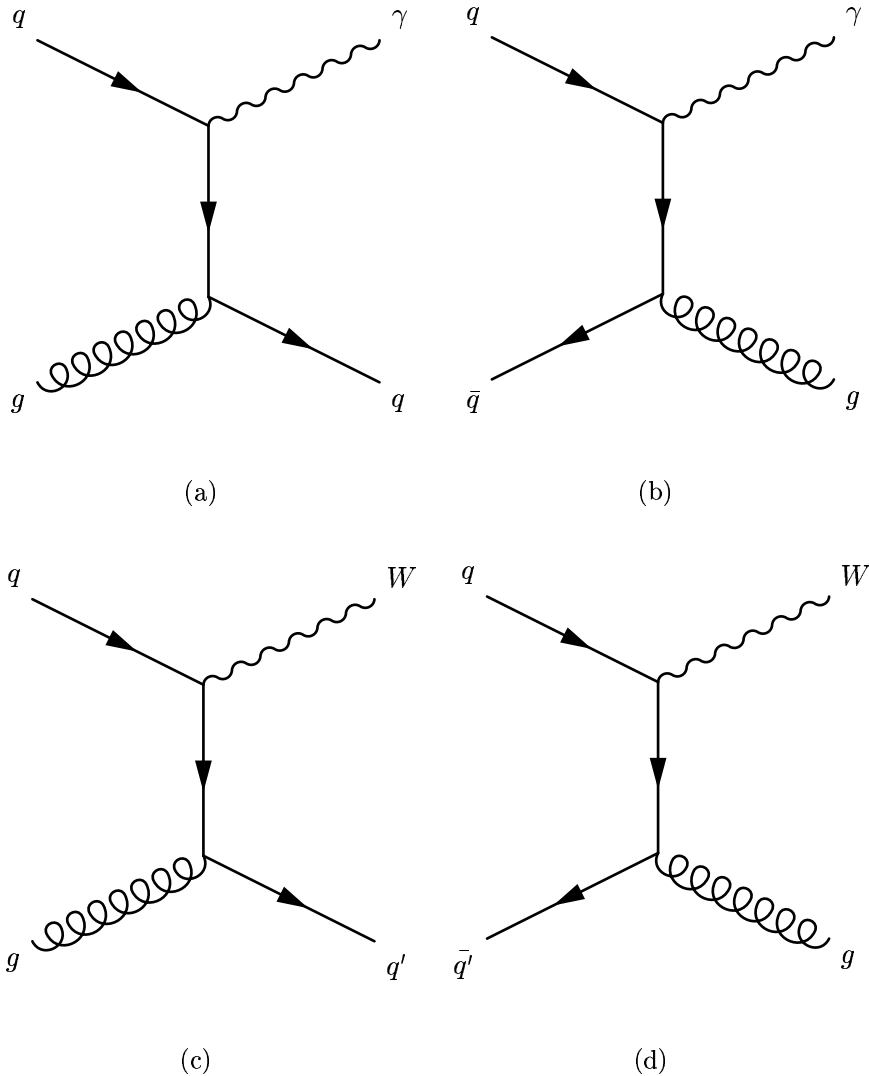


FIG. 4: Leading diagrams for W and γ production with one associated jet at the Tevatron. Diagrams (a) and (b) are for $\gamma + 1$ jet production, and (c) and (d) are for $W + 1$ jet production. Diagrams (a) and (c) dominate because of the relative strength of the gluon PDF at low x .

1211 more likely to be quark jets. This preference for quark jets is even more marked in $\gamma +$ jets
 1212 samples because the photon is massless, so we sample an even lower- x part of the PDF. In
 1213 the case of multijet production, the leading order diagram for $gg \rightarrow gg$ has a larger ampli-
 1214 tude than any of the other leading order $2 \rightarrow 2$ diagrams containing other permutations of
 1215 light quarks and gluons. Taking that in combination with the strength of the gluon PDF,
 1216 one expects jets produced in pure strong interaction events to be predominantly gluon jets,
 1217 that is, jets originating from gluons.

1218 The different partonic origins of jets matter because jets from light quarks appear to
 1219 have a different fake rate than jets from gluons. Gluon fragmentation results, on average,
 1220 in a larger number of charged particles than quark fragmentation. This behavior has been
 1221 verified experimentally, and can be seen in simulation [55]. An immediate consequence is
 1222 the fact that a quark jet will be more likely than a gluon jet to contain a single charged
 1223 track carrying most of the parton's energy. This also implies an increased probability to
 1224 produce a fake lepton.

1225 We can test the partonic origins of the jets in different processes and their effect on
 1226 fake rates using simulated data. In simulation, it is possible in most cases to match a
 1227 reconstructed jet to the quark or gluon from which it most likely developed. While we
 1228 do not trust the absolute value of fake rates in simulation, relative comparisons are still
 1229 meaningful. First, we find the fraction of jets matched to a quark in simulated $\gamma +$ jets,
 1230 $W +$ jets, and QCD multijet events. All of these samples are generated using PYTHIA, as
 1231 described in Section III. The minimum photon E_T in the photon sample is 22 GeV and we
 1232 select events with reconstructed photon $E_T > 25$ GeV. The minimum parton p_T in the jet
 1233 sample is 18 GeV/ c . The quark jet fractions for all of these processes as a function of jet E_T
 1234 are shown in Fig. 5. For any choice of jet multiplicity, the fraction of jets which are from
 1235 quarks is highest in the photon sample, next highest in the W sample and smallest in the
 1236 multijet sample. Also note that in the W and photon samples with higher jet multiplicities,
 1237 the tendency toward quark jet dominance persists but is diminished by the enhanced impact
 1238 of higher-order processes. Finally, one also sees that with increasing jet E_T , the preference
 1239 for quark jets in multijet events increases. This is also to be expected given the increased
 1240 Q^2 of the interaction and hence a reduced probability of an initial gg interaction.

1241 Figure 6 shows the difference in the fake rates between the three jet samples considered
 1242 earlier: $\gamma +$ jets, $W +$ jets, and QCD multijet. The $\gamma +$ jets sample has the highest fraction
 1243 of quark jets (See Fig. 5), followed by the $W +$ jets and multijet samples, and their fake rates
 1244 follow the same pattern. Figure 6 also shows that, in simulated multijet events, the quark
 1245 jet fake rate is nearly an order of magnitude higher than the gluon jet fake rate. Combined
 1246 with the different propensities for producing quark jets, this leads to different fake rates in
 1247 different samples. We also compare the separated quark and gluon jet fake rates for the
 1248 three samples in Fig. 6, and observe that the agreement between the separated fake rates is
 1249 better than the agreement between the inclusive ones.

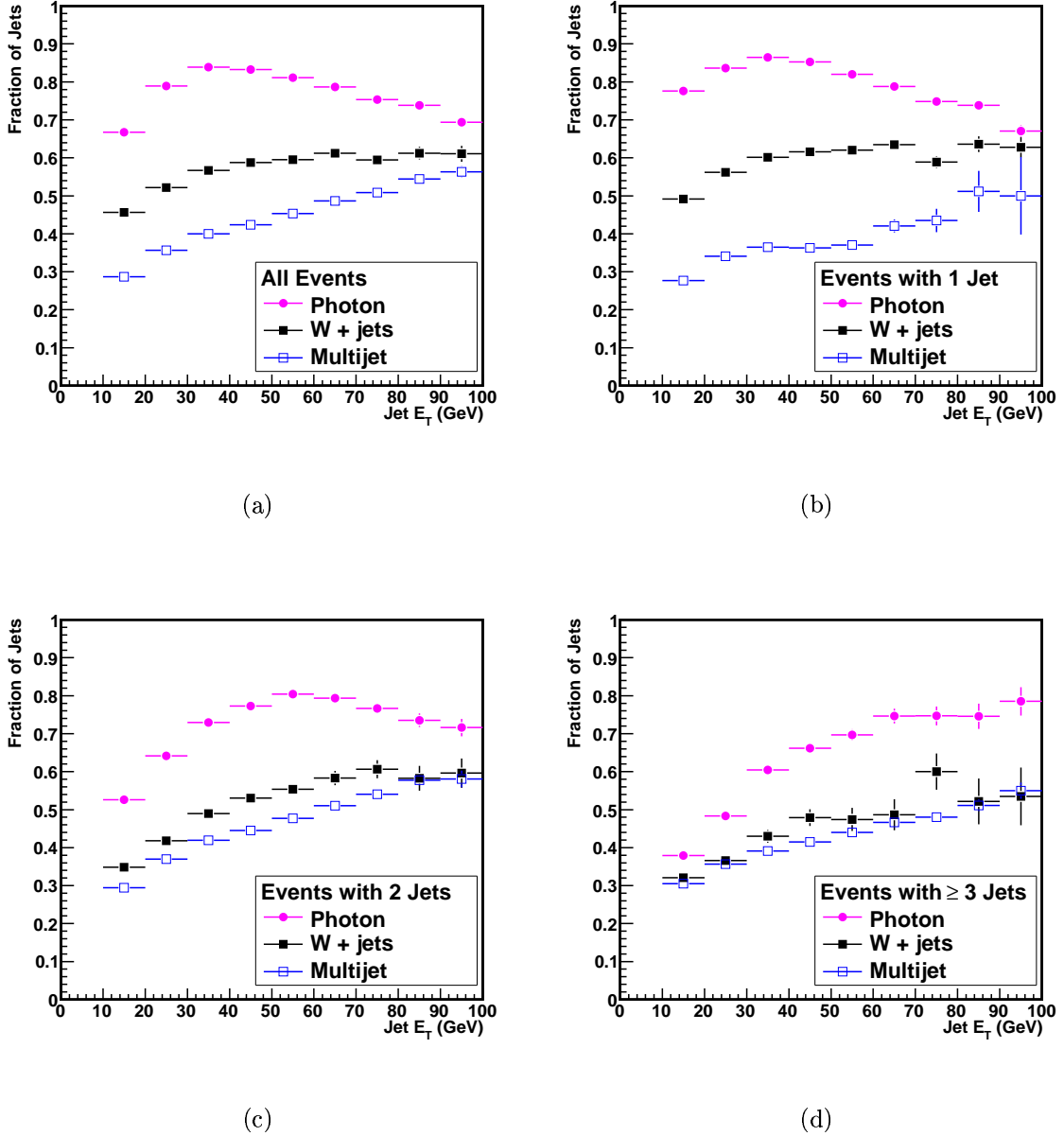
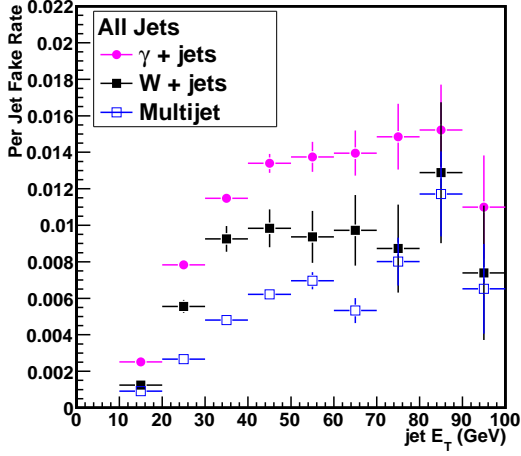


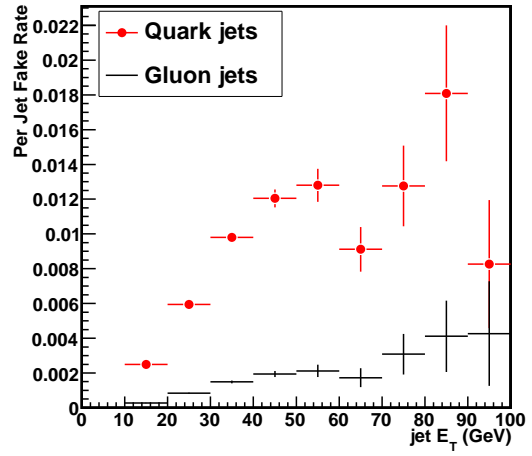
FIG. 5: The fraction of jets matched to a quark in simulated photon (filled circles), W (filled squares) and multijet (open squares) events, as a function of jet E_T . The fraction is shown for events with any number of jets (a), and then separately for events with one (b), two (c), and at least three (d) jets.

1250 **3. Fake Rate Definition**

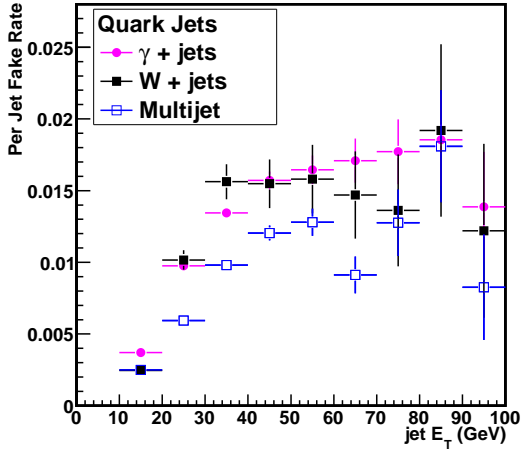
1251 The track lepton fake rate is the number of isolated tracks, divided by the number of
 1252 jets, in a sample containing no true leptons. The numerator is the number of track leptons



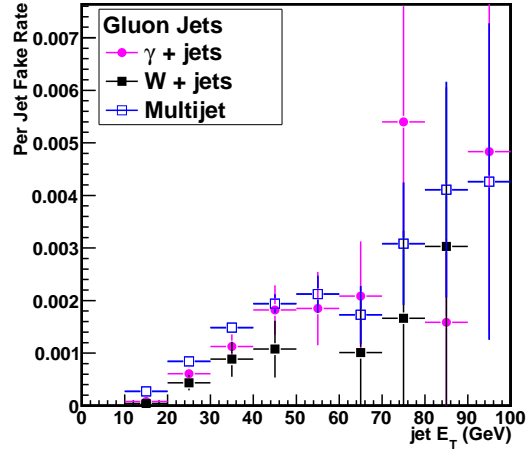
(a)



(b)



(c)



(d)

FIG. 6: Track lepton fake rates in simulation as a function of denominator jet E_T . (a) Fake rate for all jets in simulated $\gamma + \text{jets}$, $W + \text{jets}$, and multijet events. The fake rate in multijet events is lower than the fake rate in $W + \text{jets}$ events, and both are lower than that in $\gamma + \text{jets}$ events. Note that this $\gamma + \text{jets}$ sample does not have the $E_\gamma > 80$ GeV requirement applied. (b) Fake rate for jets matched to quarks (“quark jets”) compared to the fake rate for jets matched to gluons (“gluon jets”), showing the disagreement between them. Fake rates taken from the simulated multijet sample. (c) Fake rates for quark jets in the three samples. The agreement is better than that observed in (a). (d) The same, but for jets matched to gluons.

1253 according to the definitions in Section IV C. The denominator is the number of jets according
 1254 to the definition in Sec. IV D. Recall that in addition to the standard calorimeter cluster-
 1255 based jets, this jet collection includes tracks not associated with a jet as well as jets containing
 1256 a high- p_T track which otherwise would have fallen below the jet selection E_T threshold. The
 1257 jets used in constructing the fake rate are identical to those used to count jets for candidate
 1258 event selection. Note that a fake track lepton is a true isolated track, but one that does not
 1259 originate from a lepton.

1260 Ideally, the fake rate is measured in a data sample where the contamination from true
 1261 leptons is negligible. For this analysis, we use a sample of events triggered by a photon with
 1262 $E_T > 25$ GeV. Photons are restricted to the central calorimeter and selected with criteria
 1263 similar to those used for electrons, except that there must be no track pointing at the energy
 1264 deposited in the electromagnetic calorimeter [56]. To further reduce the possibility of lepton
 1265 contamination, we exclude events in which the invariant mass of the photon and any jet
 1266 in the event is close to the Z resonance ($76 \text{ GeV}/c^2 < M < 106 \text{ GeV}/c^2$) when the jet is a
 1267 track or has more than about 90% of its energy in the electromagnetic calorimeter. Finally,
 1268 we require the photon to have at least 80 GeV of energy (not E_T), to strengthen the analogy
 1269 to W production through the required Q^2 .

1270 The fake rate depends strongly on the E_T and $|\eta|$ of the jets in the denominator, so we
 1271 parameterize it as a function of these quantities. The fake rate for track leptons for each jet
 1272 multiplicity is shown as a function of the E_T and $|\eta|$ of the denominator jets in Fig. 7.

1273 Taking the jets for the lepton fake rate from a photon-triggered data sample instead of
 1274 a jet-triggered has not been done before in a dilepton $t\bar{t}$ cross section measurement. The
 1275 Run I dilepton cross section measurement [57] and the Run II measurement with 200 pb^{-1}
 1276 of integrated luminosity [20] both used samples triggered by high- E_T jets. The Run I
 1277 measurement placed an uncertainty of 62% on the fake lepton background. In the two
 1278 measurements of the previous Run II result, the uncertainty on the fake lepton background
 1279 is 30% for the earlier version of this analysis, and 51% for the analysis using two fully
 1280 reconstructed leptons. The uncertainty on the fake lepton background for this analysis will
 1281 be described in detail at the end of this section, but it is a total of 20%, with 6% from
 1282 the statistical uncertainty. The previously published measurements have a factor of 5 to
 1283 10 less integrated luminosity, so the statistical uncertainty would have made this technique
 1284 impractical in earlier measurements. As an aside, it is because of the availability of larger

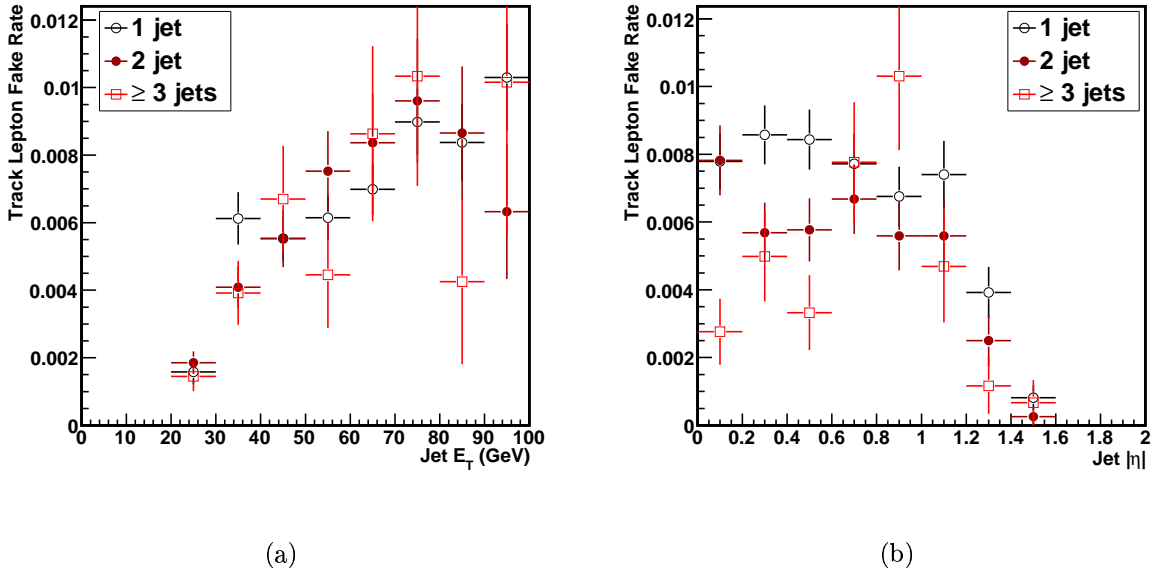


FIG. 7: Track lepton fake rates as a function of E_T (a) and $|\eta|$ (b) of the faking jet. The fake rate is the probability for a jet to pass the track lepton identification requirements, including the track isolation. The fake rate is measured in jets from photon + jets data, and includes $Z + 1$ jet events in the 1 jet fake rate. The uncertainty is statistical only. See Section VII A 3 for details.

1285 data samples that the failings of fake rates calculated with jet-triggered samples have started
 1286 to become apparent. We also note that our initial attempts to improve the fake lepton
 1287 background estimate were based on adding a third parameter, such as the number of tracks
 1288 per jet, to the fake rate. This technique was dropped in favor of the one presented here
 1289 because it was less successful when tested in simulation.

1290 4. Use of Z +jets Data

1291 In photon plus one jet events, conservation of momentum implies that events where the
 1292 measured E_T of the balancing jet is significantly lower than the photon E_T are rare. Because
 1293 of this, there are very few events in the lowest E_T bins of the fake rate. This is not crucially
 1294 important since this is an input to the zero jet event count prediction, which does not enter
 1295 into the cross section calculation. Nevertheless, it is possible to fill the gap in the one jet
 1296 fake rate by including the $Z + 1$ jet sample. The $Z +$ jets sample is a near-perfect analog
 1297 to the $W +$ jets sample, up to the slight difference in mass scale. Most $Z +$ jets events have

1298 at most one jet, typically near the E_T threshold, so there is not enough data to make useful
 1299 measurements of lepton fake rates for higher jet multiplicities. But, one-jet events where the
 1300 jet is in the lower E_T range is exactly what $\gamma + \text{jets}$ events are lacking. Therefore, the total
 1301 rate used to predict the number of fake leptons in the zero-jet lepton + track sample is the
 1302 combined rate from the $\gamma + 1 \text{ jet}$ and $Z + 1 \text{ jet}$ samples. We combine the two fake rates
 1303 by adding the jets from the $Z + 1 \text{ jet}$ numerator (denominator) to the $\gamma + 1 \text{ jet}$ numerator
 1304 (denominator) before calculating the fake rate.

1305 5. Validation of Track Lepton Fake Rate

1306 We test the accuracy of the track lepton fake rate in both real and simulated data. To
 1307 increase the size of the sample for validation, a lower kinematic threshold of 15 GeV is used
 1308 for both the track leptons and jets. This adds jets to the sample because of the steep falloff
 1309 of the E_T distribution. Also, the fake rate for 15 GeV track leptons is higher than for 20 GeV
 1310 track leptons, because it corresponds to a larger portion of the fragmentation spectrum.

1311 Using simulated CDF data, it is possible to test the fake rate estimation procedure by
 1312 using the fake rates obtained from simulated $\gamma + \text{jets}$ events to predict the number of fake
 1313 leptons in simulated $W + \text{jets}$ events. Events with 0, 1, and ≥ 2 jets in addition to the
 1314 fake lepton are considered. Figure 8 shows the predicted and observed number of fake
 1315 track leptons as a function of the E_T of the misidentified jet, for each jet multiplicity. The
 1316 integrated results are provided in Table V. The fake rate from jets associated with an 80 GeV
 1317 photon is seen to overestimate the number of fake leptons observed in jets associated with a
 1318 W . This effect is only statistically significant in events with one jet, and we will include this
 1319 18% discrepancy in the systematic uncertainty on this background. Omitting the $Z + 1 \text{ jet}$
 1320 data from the fake rate only exacerbates the disagreement (The previous section describes
 1321 the use of the $Z + \text{jets}$ data in the one jet fake rate).

1322 We directly test the fake rate obtained from the photon data using $Z + \text{jets}$ data. The
 1323 number of isolated tracks predicted in the $Z + \text{jets}$ data is compared to the number observed
 1324 for events with 0, 1, and ≥ 2 jets in addition to the isolated track. For this test, only the
 1325 fake rate from $\gamma + 1 \text{ jet}$ events is used to predict the number of fake leptons coming from the
 1326 $Z + 1 \text{ jet}$ sample. Although the event sample is small, no statistically significant discrepancy
 1327 is observed for any jet multiplicity in this test. Figure 9 shows the predicted and observed

1328 number of isolated tracks as a function of the E_T of the jet, for each jet multiplicity. Table
 1329 V provides the integrated results. The integer number of isolated tracks is well-predicted,
 1330 and the shape of the isolated track p_T distribution is well-modeled for events with zero
 1331 or one jets in addition to the isolated track. The agreement between the predicted and
 1332 observed distributions in the two-or-more jet case is more difficult to assess. There are 2358
 1333 Z events with three jets, so the predicted distribution is smooth, but there are only thirteen
 1334 Z candidates with two jets and an isolated track, so the distribution of the p_T of the isolated
 1335 tracks is highly prone to statistical fluctuations.

1336 We use the same framework to test fake rates obtained from multijet events. To mimic the
 1337 fake rate used in the previous published version of this analysis, we simulate the requirements
 1338 of the 50 GeV jet trigger at CDF on a PYTHIA multijet sample produced requiring a minimum
 1339 parton p_T of 18 GeV/ c . The fake rate is constructed as described above, except that events
 1340 with any number of jets are included. The inclusive jet fake rate is then applied to jets
 1341 from simulated $W +$ jets events. The results are shown next to the prediction from the
 1342 photon + jets fake rate in Fig. 8. For $W + 1$ jet events, 3040 ± 350 events are predicted,
 1343 and 4480 are observed. Using the same logic as used to derive the 18% systematic uncertainty
 1344 quoted above, this corresponds to a 47% systematic uncertainty for the fake rate from data
 1345 collected using a jet trigger. This motivates the choice to use the jets from the photon
 1346 trigger sample to build the fake rate.

1347 6. Fake Rates for Fully Reconstructed Leptons

1348 We also measure fake rates for all four primary lepton types, using the same method
 1349 and data as is used for the track leptons. The fake rate is at least an order of magnitude
 1350 smaller for primary leptons than for track leptons. Because there are so few events in the
 1351 numerator of the fake rate for the primary leptons, we use an inclusive fake rate instead of
 1352 calculating it separately for events with different numbers of jets. The fake rates for the fully
 1353 reconstructed leptons, as a function of the E_T and $|\eta|$ of the denominator jets, are shown in
 1354 in Fig. 10.

1355 To find the number of events where the track lepton is the lepton from the W and the
 1356 fully reconstructed lepton is fake, we multiply the fully reconstructed lepton fake rates by the
 1357 jet E_T and $|\eta|$ distributions from the lepton + \cancel{E}_T + jets data described in Section VII A 1.

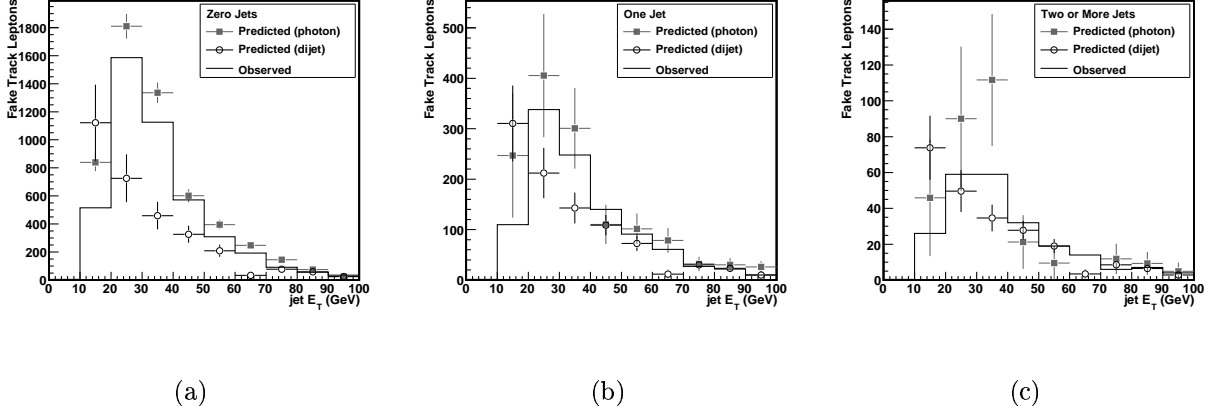


FIG. 8: Predicted and observed number of fake track leptons in simulated W + jets events, as a function of jet E_T . The comparison is made for events with zero (a), one (b), and at least two (c) jets in addition to the one that is reconstructed as an isolated track. One prediction, shown as solid squares, is made using the a fake rate derived from simulated γ + jets and Z + jets events, exactly as the fake rate is constructed from the observed data. The other, shown as open circles, is made using a fake rate derived from simulated QCD multijet events. Uncertainties on the predictions are statistical only.

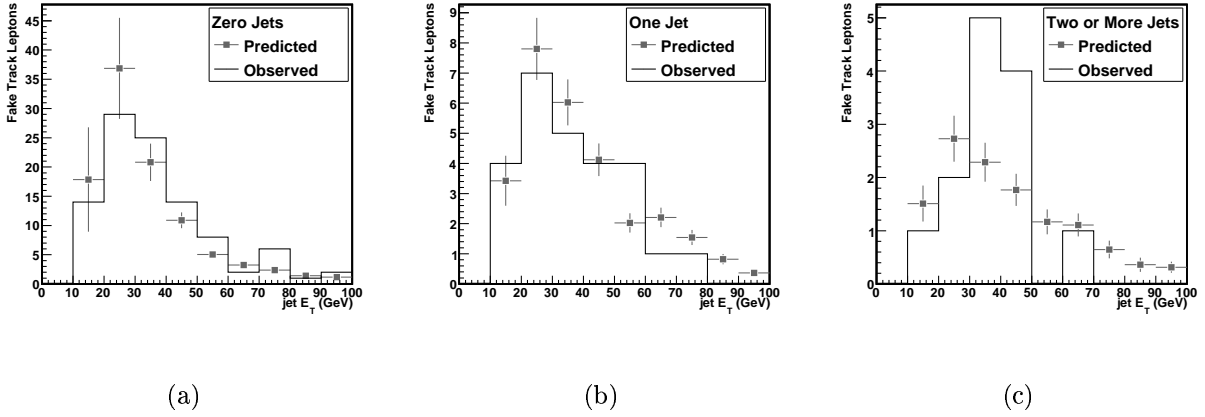


FIG. 9: Predicted and observed number of isolated tracks observed in CDF Z + jets data, as a function of jet E_T . The comparison is made for events with zero (a), one (b), and at least two (c) jets in addition to the one that is reconstructed as an isolated track. The fake rate used is derived from γ + jets data, and the uncertainty on it is statistical only.

Predict $W + \text{jets}$ with γ and $Z + \text{jets}$:		
Test in simulated data		
	Predicted	Observed
1 jet	5473 ± 147	4480
2 jets	1332 ± 200	1047
≥ 3 jets	304 ± 67	226
Predict $Z + \text{jets}$ with $\gamma + \text{jets}$:		
Test in CDF data		
	Predicted	Observed
1 jet	100 ± 13	101
2 jets	28 ± 2	26
≥ 3 jets	12 ± 1	13

TABLE V: Predicted and observed number of isolated tracks of hadronic origin in tests performed in observed and simulated data. The number of jets quoted is in addition to the jet which is reconstructed as an isolated track. The only statistically significant discrepancy observed is in the one jet category in the simulation, and is taken as part of the basis of the systematic uncertainty on this background estimate. Note that in the column headings, “Observed” refers to the directly counted isolated tracks, regardless of whether the study is done in real or simulated data.

1358 That gives the number of events with two fully reconstructed leptons where one is fake. To
1359 find the number where the true lepton is the track lepton, we scale the number by the ratio
1360 of the $W \rightarrow \ell\nu + \text{jets}$ acceptance for track leptons to the acceptance for fully reconstructed
1361 leptons. This ratio is measured in $W + \text{jets}$ events simulated using PYTHIA. There are other
1362 sources of fake leptons in the sample, but $W + \text{jets}$ is the dominant contribution, and the
1363 ratio of the acceptances for the sub-dominant contribution from $t\bar{t}$ should be similar, since
1364 the real lepton is still from a W . Summing over all lepton types yields the total contribution
1365 from fake fully reconstructed leptons, which are 6% of the total fake lepton background.

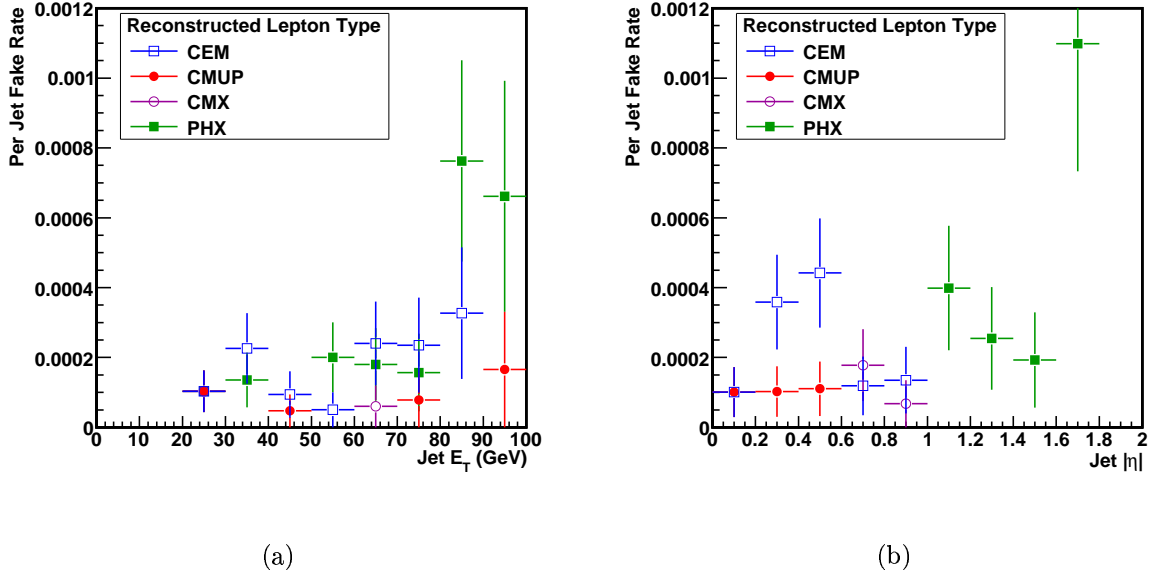


FIG. 10: Fully reconstructed lepton fake rates as a function of E_T (a) and $|\eta|$ (b) of the jet in the denominator. The fake rate is the probability for a jet to pass the lepton identification requirements and is measured in jets from photon + jets data. The shown uncertainty is statistical only.

1366 7. Contribution from $t\bar{t}$ Events with a Fake Lepton

1367 Other than $W + \text{jets}$, the only process contributing significantly (more than 5%) to
 1368 the lepton + $\cancel{E}_T + \text{jets}$ data sample is $t\bar{t}$ lepton + jets events. For a top quark mass of
 1369 175 GeV/ c^2 , corresponding to a cross section of 6.7 pb, such events produce 19% of the
 1370 jets in the lepton + \cancel{E}_T sample with three or more jets, the sample used derive the fakes
 1371 contribution to the background for the cross section measurement. Lepton + jets $t\bar{t}$ events
 1372 make a negligible contribution to lepton + \cancel{E}_T samples with one or two jets. Single top
 1373 quarks, produced through the electroweak interaction, can also generate the required lepton,
 1374 \cancel{E}_T , and jets signature, but the small cross section and lower jet multiplicity at leading order
 1375 mean that their contribution is negligible.

1376 Because of its size, the lepton + jets $t\bar{t}$ contribution deserves separate consideration.
 1377 Study of simulated $t\bar{t}$ events indicates that over 90% of the jets in these events come from
 1378 quarks. This is a very different fraction than for any other sample considered, although
 1379 many (roughly 2/3) of the jets are from heavy quarks, such as a b from t decay or a c from
 1380 W decay. The track lepton fake rate for jets from a light quark is about twice the rate for

1381 jets from a heavy quark, because the latter typically produce a larger number of charged
1382 tracks, leading to a greater likelihood to fail the track isolation criteria. As a result, the fake
1383 lepton is associated with the jet produced by a quark from W decay in about 90% of the
1384 simulated events with a fake lepton.

1385 The fake rate designed for $W + \text{jets}$ events is still usable. First, the smaller probability
1386 that heavy quark jets will be manifested as isolated tracks partially compensates for the fact
1387 that there are fewer gluon jets in $t\bar{t}$ than in the photon plus jets data used to define the fake
1388 rate. Second, the contribution of $t\bar{t}$ is still relatively small compared to $W + \text{jets}$ and the
1389 large systematic on the fake rate due to the discrepancy in the single jet bin is adequate to
1390 cover any remaining difference. We test the validity of these statements using the fake rates
1391 from the simulated $W + \text{jets}$ sample, because there is an insufficient number of events in the
1392 simulated $\gamma + \geq 3$ jet sample to make a meaningful comparison. If the $W + \text{jets}$ fake rate
1393 is sufficiently similar to the one from $t\bar{t}$ lepton + jets events, we may still use the same fake
1394 rate for both. The fake rate from the $W + \text{jets}$ sample predicts 518 ± 45 isolated tracks
1395 in a simulated $t\bar{t}$ lepton + jets sample, in which 424 are actually observed. The level of
1396 disagreement (18%) is not egregious when compared to the statistical uncertainty, and is
1397 comparable to the systematic uncertainty. We therefore use the photon + jets fake rate to
1398 predict the number of fake leptons for all events passing the $W + \text{jets}$ selection, regardless
1399 of their source.

1400 8. *Fraction of Events having Opposite Sign Leptons*

1401 We must also estimate the fraction of events with a fake lepton in which the real and
1402 fake lepton have opposite sign. This fraction is different for $W + \text{jets}$ and $t\bar{t}$ events, so they
1403 must be considered separately.

1404 First we will consider the opposite-sign fraction for $W + \text{jets}$ events. Leading diagrams
1405 for $W + \text{jets}$ production have the W recoiling against a quark which becomes a jet in the
1406 event, so the charge of the tracks in that jet is expected to be anti-correlated with the charge
1407 of the W .

1408 In simulated $W + \text{jets}$ events, the charge correlation is large, but falls off with increasing
1409 jet multiplicity. We measure opposite-sign fractions of $81 \pm 3\%$ for events with zero jets,
1410 $73 \pm 2\%$ for events with one jet, and $75 \pm 5\%$ for events with at least two jets. The

1411 difficulty with the numbers from the simulation is that the charge correlation, like the
 1412 fake rate, is influenced by details of jet fragmentation that may not be fully taken into
 1413 account in the Monte Carlo simulations. The opposite-sign fractions can be checked in
 1414 candidate lepton + track events with no jets, where the contribution from $t\bar{t}$ is negligible
 1415 but where the expected contribution of events with a fake lepton is large. Prior to an
 1416 opposite-sign requirement, the total number of predicted events agrees with the number
 1417 observed, within the statistical uncertainty. When the predicted opposite-sign fraction from
 1418 simulation is applied, more same-sign events are observed than are predicted, and the number
 1419 of opposite-sign events observed is correspondingly too small compared to the prediction.
 1420 This suggests that the simulation overestimates the fraction of events with a fake lepton of
 1421 opposite charge. We therefore obtain the opposite sign fraction from observed data, using
 1422 the zero-jet candidate events. We can further enhance the fraction of events with a fake
 1423 lepton by requiring a significant amount of energy in the region of the hadronic calorimeter
 1424 at which the track points. This is about 70% efficient for events with a fake lepton and
 1425 $Z/\gamma^* \rightarrow \tau\tau$ events, but reduces all other contributions by an order of magnitude. We then
 1426 subtract the estimated number of events from sources with two real leptons for all events and
 1427 for those with opposite sign. We find that $67 \pm 3\%$ of remaining events are opposite-sign,
 1428 which is taken to be the opposite-sign fraction for all events with zero jets.

1429 As a cross-check, we also measure the opposite-sign fraction using the zero-jet events
 1430 without the hadronic energy requirement described above, and find $69 \pm 5\%$, in good agree-
 1431 ment with the number calculated with the requirement. The larger uncertainty is due to the
 1432 systematic uncertainties on the larger contributions to the zero-jet sample from the other
 1433 processes.

1434 We cannot apply the same procedure to derive the opposite-sign fraction for higher jet
 1435 multiplicities because the contribution from $t\bar{t}$ is non-negligible. To obtain the charge corre-
 1436 lation for events with more jets, we rely on the simulation to model the dependence of the
 1437 correlation on the number of jets in the event. The assumption made is that each additional
 1438 jet dilutes the opposite-sign fraction toward 50%, the fraction corresponding to no correla-
 1439 tion. Defining a dilution factor x , the opposite-sign fraction f_{i+1} of events with $i + 1$ jets
 1440 can be expressed in terms of the fraction f_i for events with i jets as

$$f_{i+1} = 0.5x + f_i(1 - x) . \quad (11)$$

1441 From the $(81 \pm 3)\%$ and $(73 \pm 2)\%$ figures, we find $x = (26 \pm 12)\%$. Applying this to
 1442 the $(67 \pm 3)\%$ fraction from the zero-jet events, we find an opposite-sign fractions of
 1443 $(63 \pm 3)\%$ for events with one jet. Repeating the procedure with the same x and the
 1444 one-jet opposite-sign fraction, we find $(59 \pm 3)\%$ for events with two or more jets.

1445 Turning to the case of $t\bar{t}$ lepton + jets events with a fake track lepton, we observe in
 1446 simulation that 79% of such events have opposite-sign leptons. It seems likely that the
 1447 charge correlation here is attributable to the fact that the summed charge of the quark pair
 1448 produced by the W will be the opposite sign of the charge of the lepton from the other W .
 1449 We prefer not to use the number from simulation directly, since our results in the W + jets
 1450 sample suggest that the fragmentation model in simulation tends to overestimate charge
 1451 correlations. We correct the result from simulation using the observed difference between
 1452 observed and simulated data for W + 1 jet events where the jet is reconstructed as an
 1453 isolated track, using the same method described in the previous paragraph. In simulation,
 1454 81% of events are opposite-sign, compared to the 67% in the CDF data. For $t\bar{t}$ lepton + jets
 1455 events with three or more jets, we scale the fraction from simulation to $(67 \pm 6)\%$, which is
 1456 higher than the fraction for W + jets events with the same number of jets. The uncertainty
 1457 is taken to be half the difference between the original and rescaled numbers, or 9%. The
 1458 statistical uncertainties on the fractions from simulation are less than a percent and negligible
 1459 in comparison.

1460 To obtain a fake lepton background prediction for events with two or more jets, we
 1461 must combine the two opposite-sign fractions obtained for W + jets and $t\bar{t}$ lepton + jets in
 1462 proportion to the estimated number of fake leptons contributed by each process. Because
 1463 the predicted fraction of $t\bar{t}$ in the W + jets data is based on an acceptance measured in
 1464 simulation, this introduces a dependence on the $t\bar{t}$ cross section. We remove this dependence
 1465 by including it explicitly in the pretag background calculation in the likelihood expression
 1466 used to measure the cross section, which will be described in more detail in Section IX A. The
 1467 result is that, for the measured cross section of 9.6 pb, $(27 \pm 4)\%$ of jets in the normalizing
 1468 W + jets sample are predicted to be from $t\bar{t}$ for the final cross section value, and the re-
 1469 weighted opposite-sign fraction is $(61 \pm 3)\%$. Note that the 27% is calculated from the
 1470 measured $t\bar{t}$ cross section and is in a sense the result of the fit, so the uncertainty on it
 1471 is the observed change in the fraction when the cross section is varied by its calculated
 1472 uncertainties.

1473 *9. Efficiency for Additional Selection*

1474 We measure the efficiency of the Z veto and the track lepton $\Delta\varphi$ requirement in simulated
1475 $W + \text{jets}$ events generated using ALPGEN+PYTHIA Monte Carlo. The efficiency for the two
1476 criteria is $(82 \pm 2)\%$ for events with zero jets, $(85 \pm 1)\%$ for events with one jet, and
1477 $(89 \pm 2)\%$ for events with two or more jets. Scaling the event counts by these efficiencies
1478 yields the final prediction of candidate events with a fake lepton as a function of the number
1479 of jets.

1480 *10. Systematic Uncertainties*

1481 There are three sources of uncertainty in the estimate of the background from events with
1482 a fake lepton: the statistical uncertainty on the fake rate, the systematic uncertainty on the
1483 overall normalization of the estimate, and the uncertainty on the fraction of events with a
1484 fake lepton where the leptons have opposite sign.

1485 The uncertainty on the overall normalization comes from the largest observed discrepancy
1486 in the simulated and observed data tests described above. We have also argued that this
1487 18% uncertainty covers possible discrepancies between the fake rate for jets in $W + \text{jets}$
1488 events and jets in $t\bar{t}$ lepton + jets events. The uncertainty on the opposite-sign fraction is
1489 the statistical uncertainty on the fraction calculated from zero-jet candidate data, combined
1490 with the systematic uncertainty from the scaling of the fraction for $t\bar{t}$ lepton + jets events,
1491 and is 5%.

1492 Combining the 18% and 5% systematic uncertainties with the 6% statistical uncertainty,
1493 the total uncertainty on this background is 20%.

1494 **B. Diboson**

1495 *1. Diboson Acceptance*

1496 Diboson events (WW , WZ , and ZZ) events have small cross sections, comparable to the
1497 $t\bar{t}$ cross section. It is only recently that CDF and DØ have obtained sufficient data to observe
1498 WZ production [58, 59] and ZZ production [60, 61]. Also, if one or both bosons decay to
1499 leptons, these events can mimic the $t\bar{t}$ signature, so it is not possible to isolate a large sample

1500 of such events in the data. Therefore, the acceptance calculated from simulated events is
 1501 used together with the theoretical production cross sections to estimate this background.
 1502 We use event samples generated with the PYTHIA Monte Carlo generator and apply the same
 1503 corrections to the diboson acceptance as we did for the signal acceptance, with one additional
 1504 correction for the rate of jet production, described below. The estimated number of events
 1505 in the candidate sample is then the corrected acceptance multiplied by the theoretical cross
 1506 section and the integrated luminosity. The theoretical cross sections for these processes are
 1507 12.4 ± 0.8 pb for WW , 3.7 ± 0.3 pb for WZ , and 3.7 ± 0.3 pb for ZZ [62]. The ZZ sample
 1508 includes the γ^* contribution, with $M_{Z/\gamma^*} > 2$ GeV/ c^2 for both bosons. These cross sections
 1509 are calculated using the MCFM Monte Carlo program [62] and the uncertainties are based
 1510 on the Q^2 and PDF dependence of the cross sections.

1511 2. Correction for Number of Jets

1512 PYTHIA is a leading order Monte Carlo program and so is not expected to correctly predict
 1513 the fraction of events with extra high- p_T jets in addition to the core process. A scale factor
 1514 derived from a comparison of jet production in real and simulated $Z + \text{jets}$ data is applied
 1515 to correct the acceptance for events with two or more jets up to the observed level. A sample
 1516 of Z 's are selected with two opposite-charge, fully reconstructed electrons or muons having
 1517 an invariant mass in the interval $76 \text{ GeV}/c^2 < M < 106 \text{ GeV}/c^2$. The fraction of events
 1518 with two or more jets in simulation, 0.0142 ± 0.0002 , is lower than the fraction observed
 1519 in data, 0.0153 ± 0.0008 . A scale factor, once again defined as the ratio of the fraction in
 1520 observed data to the fraction in simulated data, is calculated for each jet multiplicity. The
 1521 scale factors found are 1.006 ± 0.002 for events with zero jets, 0.940 ± 0.018 for events
 1522 with one jet, and 1.08 ± 0.06 for events with two or more jets, where the uncertainties are
 1523 statistical only. We then multiply the acceptance by the appropriate scale factor for each
 1524 jet multiplicity. In order to maintain the same overall normalization, we rescale all three
 1525 acceptances by a common factor so that their sum is unchanged.

3. Systematic Uncertainties

The systematic uncertainties relevant to the signal acceptance also apply here. The lepton identification uncertainties are still 1.1% for both fully reconstructed and track leptons. The uncertainty on the number-of-jets correction, 5.5%, also applies to the predicted number of events. The jet energy scale uncertainty is also relevant here, and is evaluated in the same way, but has a larger effect: the energy spectrum of radiated jets falls sharply, so that small changes in the jet energy can lead to large changes in the event selection efficiency. The resulting uncertainty is 5.8%. Finally, we also include the theoretical uncertainties on the cross sections used to normalize the background prediction, which are 6% for the WW and 7% for WZ and ZZ . The total uncertainty on the diboson background calculation is 11%.

C. Drell-Yan

Drell-Yan events with \cancel{E}_T are a significant source of background for $t\bar{t}$ lepton + track events since there are two real leptons in the final state and the inclusive cross section is large ($\sigma(p\bar{p} \rightarrow Z/\gamma^*) \times Br(Z/\gamma^* \rightarrow \ell^+\ell^-) = 251 \pm 5$ pb for $66 \text{ GeV}/c^2 < M_{\ell\ell} < 116 \text{ GeV}/c^2$ [28]). In the case of $Z/\gamma^* \rightarrow \tau\tau$, the \cancel{E}_T is mostly from the neutrinos from the τ lepton decays, and the background calculation is based on simulation. For $Z/\gamma^* \rightarrow ee/\mu\mu$, there are no neutrinos in the final state and any \cancel{E}_T is the result of the flawed reconstruction of one or more leptons or jets. Such events are rare and difficult to distinguish from other sources of two leptons and \cancel{E}_T , so it is difficult to verify that they are simulated accurately. It is possible, however, to select a sample of events from the collision data with a high concentration of $Z/\gamma^* \rightarrow ee/\mu\mu$ events with \cancel{E}_T , and build an estimate using it, integrating information from simulation. The drawback is that the precision of this hybrid method is limited by its statistical uncertainty. This background estimate carries the largest uncertainty of any input to the cross section measurement.

1. $Z/\gamma^* \rightarrow \tau\tau$

It is difficult to isolate $Z/\gamma^* \rightarrow \tau\tau$ events in the data, but Monte Carlo simulation is expected to do a reasonable job of modeling the event kinematics because real neutrinos are responsible for the \cancel{E}_T in the final state. Therefore the estimate of the $Z/\gamma^* \rightarrow \tau\tau$

1554 background is calculated in the same way as the diboson backgrounds, including the rescaling
 1555 to compensate for the deficit in generated extra jets. Events are generated with $M(Z/\gamma^*) >$
 1556 $30 \text{ GeV}/c^2$; the corresponding cross section is $327 \pm 7 \text{ pb}$ [28]. The fractional systematic
 1557 uncertainties on the resulting background are also identical to those in the diboson case.

1558 *2. Calculation of $Z/\gamma^* \rightarrow ee/\mu\mu$ Background*

1559 The estimate of the background from $Z/\gamma^* \rightarrow ee/\mu\mu$ events is calculated as follows:

$$N_{\text{DY}}^i = N_{\text{out}}^i + N_{\text{in}}^i \quad (12)$$

$$N_{\text{out}}^i = (n_{25} - \hat{n}_{25}) f_i R_i \quad (13)$$

$$N_{\text{in}}^i = (n_{40} - \hat{n}_{40}) f_i \quad (14)$$

1560 The total number of background events, N_{DY}^i , is the sum of the number inside and outside
 1561 the “ Z region”, defined as those event where the lepton + track invariant mass is between
 1562 76 and 106 GeV/c^2 . The label i designates the number of jets, where i may be zero, one,
 1563 or two. All events with two or more jets are included in $i = 2$. Outside of the Z region,
 1564 the \cancel{E}_T minimum from the event selection is 25 GeV , so the background estimate N_{in}^i for
 1565 that region is based on the number n_{25} of lepton + track events with at least 25 GeV of \cancel{E}_T
 1566 in the CDF data in the Z region. Inside the Z region, the \cancel{E}_T minimum is 40 GeV , so we
 1567 count the number of events n_{40} in the same data with at least 40 GeV of \cancel{E}_T . To isolate the
 1568 contribution of $Z/\gamma^* \rightarrow ee/\mu\mu$ to those samples, we subtract the estimated number of events
 1569 from other sources passing the selection, labeled \hat{n}_{25} and \hat{n}_{40} in the above. The selection
 1570 used for n_{25} and n_{40} , and the calculation of \hat{n}_{25} and \hat{n}_{40} , are described in Section VII C 3.

1571 These data include events with any number of jets, so we multiply the number of events
 1572 by the fraction f_i expected to have a particular jet multiplicity i . Also, the background
 1573 estimate for events outside the Z region is based on an event count inside the Z region,
 1574 so we multiply it by the expected ratio R_i of the number of background events outside
 1575 the Z region to the number inside the region. These fractions are measured in simulated
 1576 $Z/\gamma^* \rightarrow ee/\mu\mu$ events. See Section VII C 4 for details.

1577 The statistical and systematic uncertainties on this method are described in Sec-
 1578 tion VII C 5.

3. Data Sample for Normalization

To obtain a sample of events from the CDF data similar to the candidate sample but with a larger contribution from $Z/\gamma^* \rightarrow ee/\mu\mu$, we alter the event selection by restricting the sample to the Z region ($76 \text{ GeV}/c^2 < M < 106 \text{ GeV}/c^2$) and including events of all jet multiplicities. The event selection is otherwise identical to that of the main analysis. In this sample, we count the number of events with $\cancel{E}_T > 25 \text{ GeV}$ and $\cancel{E}_T > 40 \text{ GeV}$, corresponding to the \cancel{E}_T thresholds used inside and outside the Z region in the candidate selection. The number of events in these samples are n_{25} and n_{40} in Equations 12-14.

These data are expected to contain many $Z/\gamma^* \rightarrow ee/\mu\mu$ events with \cancel{E}_T , but may also contain events from other sources, including $t\bar{t}$, WW , WZ , ZZ , $Z/\gamma^* \rightarrow \tau\tau$, and events with a fake lepton. We calculate the contributions of each of these exactly as described for the main analysis, except that the event selection is the modified version described above. The predicted number of events in both the $\cancel{E}_T > 25 \text{ GeV}$ and $\cancel{E}_T > 40 \text{ GeV}$ samples, labeled \hat{n}_{25} and \hat{n}_{40} in Equations 12-14 are subtracted from the corresponding number of observed events in the data to yield the number attributable to $Z/\gamma^* \rightarrow ee/\mu\mu$.

Once again, a dependence on the $t\bar{t}$ cross section appears and must be treated with care. As with the background from events with a fake lepton, we include this dependence explicitly in the likelihood used to calculate the cross section (See Section IX A).

4. Application of Simulated Data

We use calculations from simulated $Z/\gamma^* \rightarrow ee/\mu\mu$ events to divide the Drell-Yan events among the jet multiplicity bins and estimate the number of events outside the Z region. To calculate the necessary ratios f_i and R_i , we select events in the simulation using the criteria described in the previous section (VII C 3), except that the \cancel{E}_T threshold is kept constant at 25 GeV and events both inside and outside the Z region are included. That is, the event selection is identical to the main event selection except that there is no Z veto.

To measure R_i , we count the number of events inside and outside the Z region for each jet multiplicity. The ratio of the number outside to the number inside is R_i . We correct R_i for the different invariant mass resolutions in observed and simulated data. Comparing the fractions of events inside and outside the Z region for the different fully reconstructed lepton

The fraction f_i with each jet multiplicity			
	$i = 0$ jets	$i = 1$ jet	$i = 2$ jets
CEM	0.63 ± 0.02	0.28 ± 0.02	0.09 ± 0.01
CMUP+CMX	0.57 ± 0.02	0.32 ± 0.02	0.11 ± 0.01
PHX	0.68 ± 0.03	0.26 ± 0.02	0.06 ± 0.01
Ratio R_i of number inside 76-106 GeV/ c^2 to number outside			
	$i = 0$ jets	$i = 1$ jet	$i = 2$ jets
CEM	1.22 ± 0.09	0.94 ± 0.10	0.89 ± 0.19
CMUP+CMX	0.41 ± 0.04	0.31 ± 0.04	0.34 ± 0.08
PHX	0.47 ± 0.05	0.47 ± 0.08	0.84 ± 0.29

TABLE VI: Inputs to the $Z/\gamma^* \rightarrow ee/\mu\mu$ background estimate from simulation. The index i represents the number of jets in the events in which the quantity is measured, and the $i = 2$ category includes all events with two or more jets. Shown uncertainties are statistical only; systematic uncertainties are discussed in Section VII C 5

1608 types, we find correction factors significantly different from unity only for electron + track
1609 pairs. For CEM + track Z events, the mass region only includes 98% as many events in real
1610 data as it does in simulation. For PHX + track events, the number is 94%. We multiply
1611 these numbers by R_i . The uncertainties on these numbers are negligible compared to other
1612 uncertainties on this background.

1613 To distribute the estimate among the zero, one, and two-or-more jet categories, we mea-
1614 sure the fraction of events in the Z region having each of these jet multiplicities. These
1615 fractions, labeled f_i in Equations 12-14, depend on PYTHIA's modeling of the probability
1616 to produce extra jets, like the acceptances measured for diboson and $Z/\gamma^* \rightarrow \tau\tau$ events.
1617 Therefore, we apply the correction factors derived in Section VII B 2 here as well. After
1618 correction, the fractions f_i are rescaled by a common factor so that they sum to unity.

1619 The values of R_i and f_i , after correction, are shown in Table VI for each type of fully
1620 reconstructed lepton.

1621 *5. Systematic Uncertainties*

1622 The largest uncertainty on the $Z/\gamma^* \rightarrow ee/\mu\mu$ background estimate is the statistical
1623 uncertainty, which is 20%. This uncertainty is due in approximately equal parts to the sizes
1624 of the real and simulated data samples. The Monte Carlo samples used to calculate the
1625 ratios R_i and f_i , described in the previous section (VII C 4), contain 13.8 million events. To
1626 generate enough events to significantly reduce the uncertainty is impractical, and even if
1627 enough events were generated to make the contribution from simulation negligible, the total
1628 statistical uncertainty would still be 13%.

1629 Since the scale factor that is used to correct the number of extra jets produced by PYTHIA
1630 is applied to R_i , the fraction of events with jet multiplicity i , the statistical uncertainty of
1631 5.5% on the correction factor also contributes here.

1632 Finally, the reliability of the ratios R_i and f_i depends on the ability of the simulation
1633 to model the \cancel{E}_T from mismeasured objects. One way to make a quantitative comparison
1634 between observed and simulated data is to compare the fraction of events which exceed the
1635 25 GeV \cancel{E}_T threshold. Since many processes will contribute to the high- \cancel{E}_T ‘‘Drell-Yan’’
1636 data sample, we require the \cancel{E}_T to be pointing at a jet or the track lepton by inverting
1637 the corresponding $\Delta\varphi$ selection requirements. This ensures that the comparison is mostly
1638 between real and simulated $Z/\gamma^* \rightarrow ee/\mu\mu$ events in which the \cancel{E}_T is due to a mismeasured
1639 jet or lepton. The fraction of events with $\cancel{E}_T > 25$ GeV is then measured in the data, and the
1640 \cancel{E}_T distribution from the simulation is integrated to find the threshold that would give the
1641 same fraction of events above threshold. The outcome is a shift of 1 GeV in the threshold,
1642 to 24 GeV. All of the ratios from the simulation are re-derived with the 24 GeV threshold
1643 and the background is recalculated. The recalculated background estimate is 13.5% lower
1644 than the default estimate, and the full difference is taken as a systematic uncertainty.

1645 Combining the statistical and systematic uncertainties in quadrature yields a total un-
1646 certainty of 25% on this background.

1647 **D. Summary of Pretag Backgrounds**

1648 Backgrounds to the lepton + track $t\bar{t}$ sample come from diboson, Drell-Yan, and W + jets
1649 events. Where possible, background estimates include information from control samples in

Source	Uncertainty on background	Uncertainty on cross section
Lepton identification	1.6%	0.3%
Jet energy scale	5.8%	1.0%
Jet multiplicity	5.5%	1.8%
Diboson normalizations	6-7%	0.5%
$Z/\gamma^* \rightarrow ee/\mu\mu$	25%	3.6%
$W + \text{fake lepton}$	20%	7.9%

TABLE VII: Summary table of systematic uncertainties on the pretag background estimate. The $Z/\gamma^* \rightarrow ee/\mu\mu$ uncertainty includes the statistical uncertainty and the systematic uncertainty on the projection of the number of events to outside the Z mass region. The uncertainty on the jet multiplicity correction is listed separately, as it applies to the diboson and $Z/\gamma^* \rightarrow \tau\tau$ backgrounds as well.

1650 the observed data. In the case of $W + \text{jets}$ with a fake lepton, the background estimate is
1651 based almost entirely on data. For the $Z/\gamma^* \rightarrow ee/\mu\mu$ background, measurements in the
1652 data set the overall normalization but simulation is used to fill in the details. Diboson and
1653 $Z/\gamma^* \rightarrow \tau\tau$ contributions are estimated using simulation alone, with corrections obtained
1654 from comparisons between real and simulated applied where relevant.

1655 The predicted number of background events for each of these sources is presented in
1656 Table XI. The systematic uncertainties on all of the backgrounds and the corresponding
1657 uncertainty on the cross section measurement are collected in Table VII. Some care must
1658 be taken when combining the background uncertainties, due to correlations. The systematic
1659 uncertainties due to lepton and jet reconstruction are fully correlated between the diboson
1660 and $Z/\gamma^* \rightarrow \tau\tau$ estimates, and must be summed directly rather than in quadrature. Simi-
1661 larly, the uncertainty on the jet multiplicity correction is correlated between the Drell-Yan
1662 and diboson backgrounds. All other uncertainties are uncorrelated.

VIII. BACKGROUND ESTIMATION IN TAGGED SAMPLE

The tagged background estimate differs substantially from the pretag background estimate. First, the nature of the background changes when a tagging requirement is added. In the pretag analysis the dominant background is W +jets events with a fake lepton. In the tagged analysis backgrounds containing b -jets dominate. This includes processes producing two leptons and one or more b -jets, such as $Z + b\bar{b}$ events, as well as events from $t\bar{t}$ in the lepton + jets channel where one of the jets, either from the light quarks from the W decay or from one of the b quarks, is misidentified as a lepton. Second, in the tagged analysis, we are able to estimate all backgrounds, except for those arising from $t\bar{t}$ itself, using a single data-driven technique discussed below. The background from $t\bar{t}$ events with a fake lepton are estimated separately using a combination of real and simulated CDF data.

The tagged background estimate is based upon jet tagging rates obtained in generic QCD multijet events. We apply this tagging rate to the pretag candidate events, taking advantage of the fact that it has a large background component. We then correct this for tagged events from $t\bar{t}$ decays in the pretag sample, and for $t\bar{t}$ lepton + jets events with a fake lepton. Simulated events are used to estimate the size of the corrections.

A. Data-Based Estimate of Background

The background of the tagged lepton + track sample can be organized into two parts. The first is made up of processes with a decay signature similar to the signal, such as $Z + b\bar{b}$ events, or any event passing pretag selection criteria that also has a mistagged jet. In the $Z + b\bar{b}$ case, the b tag is legitimate and the mismeasurement of some object in the event produces false \cancel{E}_T . In the mistag case, a jet is falsely identified as a b -jet. Such backgrounds may be estimated using tag rate matrices, discussed in more detail below. The second category of background events are fakes from $t\bar{t}$ decay in the lepton + jets channel, where a jet is falsely identified as a track lepton. For these events, the probability to tag the event will be underestimated by the matrix because there are two b -jets in the event.

As stated in Section VIB, positive tags are interpreted to be tags of long-lived B hadrons and negative tags are interpreted as “mistags”, or mistakes due to material interactions or resolution effects. Positive and negative tag rates of generic QCD jets are parameterized in

1692 five quantities: jet E_T , the number of tracks in the jet, jet η , the number of primary vertices
 1693 in the event, and the total scalar sum of the E_T of all the jets in the event, Σp_T . These
 1694 parameterizations are termed “tag matrices”. The generic QCD jet samples used to build
 1695 the matrices contain real tags from B hadron decays, as well as mistags.

1696 As a first step in estimating the backgrounds, we treat all events in the pretag sample
 1697 as if they are from background sources that have the same relative proportion of heavy and
 1698 light flavor jets as the generic multijet sample. We apply the positive tag rate matrix to
 1699 all of the jets in the sample to obtain a first estimate of the expected number N_{matrix} of
 1700 background events in the sample. This estimate has to be corrected for the fact that the
 1701 sample is not entirely background and the fact that the jets do not have the same mix of
 1702 heavy and light quarks as generic QCD multijet events.

1703 In particular, $t\bar{t}$ events do not have the same tagging rate as generic QCD events, the rate
 1704 represented by the tag rate matrices. Top quark pair decays via the dilepton channel make up
 1705 a considerable portion of the pretag events by design, but these should not contribute to the
 1706 background estimate. We estimate this number $N_{\text{matrix}}^{\text{dil}}$ in Section VIII B and subtract it from
 1707 N_{matrix} . Also, a portion of the fake lepton background is not due to generic QCD processes,
 1708 but arise from $t\bar{t}$ decays in the lepton + jets channel. Recall that in this analysis $t\bar{t}$ decays
 1709 in the lepton + jets channel decays are considered a background. Again, these $t\bar{t}$ events
 1710 do not have the tagging rate predicted by the tag rate matrices, but unlike the dilepton
 1711 contribution, they are a background. Therefore, we need to subtract their contribution
 1712 $N_{\text{matrix}}^{\text{LJ}}$ from the matrix estimate, and add back the correct contribution $N_{\text{fakes}}^{\text{LJ}}$. $N_{\text{fakes}}^{\text{LJ}}$ is the
 1713 proper estimate of the number of lepton + jets events which pass the lepton + track selection
 1714 with a fake lepton and are tagged because of the presence of b -jets. These numbers will both
 1715 be derived in Section VIII C. Thus, the total tagged lepton + track background is given by:

$$N_{\text{bkg}}^{\text{tag}} = N_{\text{matrix}} - N_{\text{matrix}}^{\text{dil}} - N_{\text{matrix}}^{\text{LJ}} + N_{\text{fakes}}^{\text{LJ}} . \quad (15)$$

1716 Note that the tagging rate for background events with a fake lepton from W + jets
 1717 processes is well estimated by the tag rate matrices, and is included in N_{matrix} . Also, we
 1718 are now including jets from W/Z + jet events in the category of generic jets though we
 1719 pointed out earlier that they differ from QCD jets in average track multiplicity, which has
 1720 a significant impact on the lepton fake rate. The impact of these differences is taken into
 1721 account in the tag rate matrix, which is parametrized as a function of track multiplicity.

N_{matrix}	13.7 ± 1.1
$N_{\text{matrix}}^{\text{dil}}$	8.6 ± 2.3
$N_{\text{matrix}}^{\text{LJ}}$	0.7 ± 0.1
$N_{\text{fakes}}^{\text{pretag}}$	30.7 ± 6.7
$f_{W \geq 3j}^{\text{tag}}$	0.239 ± 0.008
$f_{\text{tag}}^{\text{top}}$	0.70 ± 0.03
$N_{\text{fakes}}^{\text{LJ}}$	5.2 ± 1.2
$N_{\text{bkg}}^{\text{tag}}$	9.5 ± 2.8

TABLE VIII: Details and results of the tagged background calculation. Uncertainties include systematic contributions.

As such, it can be applied equally well to jets in generic multijet processes and $W/Z + \text{jet}$ events.

B. Correction for $t\bar{t}$ Dilepton Content in the Pretag Candidate Sample

The pretag lepton + track sample has a large fraction of $t\bar{t}$ events, which should not be counted in the background estimate. The contribution to N_{matrix} from dilepton $t\bar{t}$ decays is estimated using simulated $t\bar{t}$ events. We derive the matrix tag rate, ϵ_{matrix} by applying the tag rate matrix to all jets in the pretag candidate events in simulated $t\bar{t}$ events, and divide by the total number of pretag events. We find $\epsilon_{\text{matrix}} = 0.122 \pm 0.025$. The total contribution to the background $N_{\text{matrix}}^{\text{dil}}$ from dilepton $t\bar{t}$ events is then given by

$$N_{\text{matrix}}^{\text{dil}} = \epsilon_{\text{matrix}} (N_{\text{obs}}^{\text{pretag}} - N_{\text{bkg}}^{\text{pretag}}), \quad (16)$$

where ϵ_{matrix} is the $t\bar{t}$ tag rate, and the estimated number of $t\bar{t}$ events in the pretag candidate sample is the difference between the number of observed pretag candidates and the predicted background, $N_{\text{obs}}^{\text{pretag}} - N_{\text{bkg}}^{\text{pretag}}$, which were described in Section VII.

We find $N_{\text{matrix}}^{\text{dil}}$ to be 8.6 ± 2.3 events. Values used in the calculation are found in Table VIII.

1736 C. Correction for $t\bar{t}$ Lepton + Jets in Pretag Sample

1737 As discussed in Section VII the fake lepton background originates from two processes.
 1738 The first is the QCD radiation of extra jets in $W + \text{jets}$ events, for which we can estimate
 1739 the tag rate using the matrix. The second is the lepton + jets channel decay of $t\bar{t}$ events,
 1740 which is estimated separately.

1741 We treat the $t\bar{t}$ lepton + jets channel as a background source and these events are rejected
 1742 from the acceptance for our selection. These events are present in the pretag sample, and
 1743 therefore contribute to N_{matrix} . However, like dilepton $t\bar{t}$ events, lepton + jets $t\bar{t}$ events do
 1744 not have the same tag rate as predicted by the tag rate matrices. As such, their contribution
 1745 to N_{matrix} needs to be replaced by a more accurate estimate. We subtract the lepton + jets
 1746 $t\bar{t}$ contribution in the same manner as for dilepton events. The tag rate in lepton + jets
 1747 events is slightly larger than in dilepton events because there are more jets per event. Using
 1748 simulated $t\bar{t}$ lepton + jets events we use the matrix to find the tag rate, and then multiply
 1749 by the number of predicted pretag background events from the $t\bar{t}$ process with a fake lepton:

$$N_{\text{matrix}}^{\text{LJ}} = N_{\text{fakes}}^{\text{pretag}} f_{\text{fakes}}^{\text{LJ}} \epsilon_{\text{matrix}}^{\text{LJ}}, \quad (17)$$

1750 where $N_{\text{fakes}}^{\text{pretag}}$ is the estimated number of fakes in the pretag sample and provides an overall
 1751 normalization for the tagged estimate. $f_{\text{fakes}}^{\text{LJ}}$ is the fraction of pretag fakes that come from $t\bar{t}$
 1752 decays in the lepton + jets channel, derived from simulation. We find $N_{\text{matrix}}^{\text{LJ}}$ to be 0.7 ± 0.1 .

1753 The actual contribution from the $t\bar{t}$ lepton + jets channel, $N_{\text{fakes}}^{\text{LJ}}$, now needs to be esti-
 1754 mated and added back into the total background; see Eq. 15. Because the pretag fake lepton
 1755 background estimate is based on $W + \text{jets}$ data, this is equivalent to finding the actual $t\bar{t}$
 1756 content of the events passing that selection which are also tagged. The quantity $N_{\text{fakes}}^{\text{LJ}}$ is
 1757 factorized as

$$N_{\text{fakes}}^{\text{LJ}} = N_{\text{fakes}}^{\text{pretag}} f_{W+\geq 3\text{jets}}^{\text{tag}} f_{\text{tag}}^{\text{top}}. \quad (18)$$

1758 Recall that in the pretag background estimate we used the fraction of events with a fake
 1759 lepton that has the opposite charge of the primary lepton. We need it here as well, but it is
 1760 different in the pretag fake lepton sample than in the tagged fake lepton from $t\bar{t}$ sample, so
 1761 we correct for the different opposite sign fractions in pretag and tagged fakes. $f_{W+\geq 3\text{jets}}^{\text{tag}}$ is
 1762 the fraction of $W + \geq 3$ jet events observed in data that are tagged, and $f_{\text{tag}}^{\text{top}}$ is the fraction
 1763 of tagged $W + \geq 3$ jet events which are from the $t\bar{t}$ lepton + jets channel. As in the pretag

1764 case, we are concerned with $W+ \geq 3$ jet events because we require at least two jets in the
 1765 events selection, and so an additional jet is required to fake the track lepton.

1766 The fraction $f_{W+\geq 3jets}^{\text{tag}}$ is calculated directly from the data, without using simulation. We
 1767 select $W+ \geq 3$ jet events with the same criteria that defines the lepton + \cancel{E}_T + jets sample
 1768 used to normalize the pretag fake lepton estimate (See Section VII A). The fraction of those
 1769 events which are tagged is $f_{W+\geq 3jets}^{\text{tag}}$.

1770 The fraction $f_{\text{tag}}^{\text{top}}$ of tagged $W+ \geq 3$ jet events which are $t\bar{t}$ lepton + jets is estimated as

$$f_{\text{tag}}^{\text{top}} = \frac{\alpha_{\text{LJ}} \sigma_{t\bar{t}} \int \mathcal{L} dt}{N_{\text{cand}}^{\text{LJ}}} . \quad (19)$$

1771 In the above, α_{LJ} is the lepton + jets acceptance in simulated $t\bar{t}$ events using the lep-
 1772 ton + $\cancel{E}_T + \geq 3$ jet selection, including the requirement that at least one jet be tagged,
 1773 that defines the tagged $W+ \geq 3$ jet sample described above. $\int \mathcal{L} dt$ is the total integrated
 1774 luminosity, $\sigma_{t\bar{t}}$ is the $t\bar{t}$ cross section, and $N_{\text{cand}}^{\text{LJ}}$ is the number of tagged lepton + jets events
 1775 in the CDF data. Those events are selected using the same criteria as the events used to
 1776 find $f_{W+\geq 3jets}^{\text{tag}}$. So the number of tagged $W+ \geq 3$ jets events which are from $t\bar{t}$ decays is
 1777 estimated by multiplying the acceptance for the $t\bar{t}$ lepton + jets channel by the integrated
 1778 luminosity and the $t\bar{t}$ cross section. By dividing by the number of candidate lepton + jets
 1779 events in the data we find the fraction of tagged events which are from $t\bar{t}$.

1780 Like some of the pretag backgrounds, this background depends on the $t\bar{t}$ cross section, so
 1781 we also include this dependence explicitly in the likelihood calculation (See Section IX A).
 1782 The final value of $f_{\text{tag}}^{\text{top}}$ is in Table VIII.

1783 **D. Systematic Uncertainties on Tagged Background Estimate**

1784 The systematic uncertainty on the tagged background estimate consists of the combined
 1785 uncertainties from the two components of the background: the background estimated using
 1786 the tag rate matrix and the background from lepton + jets channel events with a fake
 1787 lepton. Statistical errors on quantities derived from simulation, such as $\epsilon_{\text{matrix}}^{\text{top}}$ and $f_{W+\geq 3}^{\text{tag}}$,
 1788 are negligible.

1789 *1. Data-Based Background Prediction*

1790 The systematic uncertainty on the data-based prediction method is 8%. This uncer-
 1791 tainty applies to all predictions from the mistag matrix. It mostly arises from charm and
 1792 light flavor contamination in the data used to derive the tag rate matrices. Because this
 1793 systematic uncertainty is correlated among all predictions made using the matrix, we only
 1794 apply the systematic for the matrix technique to the physics background portion of N_{matrix} ,
 1795 the difference $N_{\text{matrix}} - N_{\text{matrix}}^{\text{dil}} - N_{\text{matrix}}^{\text{LJ}}$.

1796 Tagging predictions made by the tag rate matrices also have a statistical uncertainty
 1797 due to the limited sample size for each entry in the matrix. This uncertainty applies to
 1798 each of the three numbers calculated using the matrix, but is uncorrelated between them.
 1799 This contributes uncertainties of 1.1 events to N_{matrix} , 1.8 events to $N_{\text{matrix}}^{\text{dil}}$, and 0.1 events
 1800 to $N_{\text{matrix}}^{\text{LJ}}$ (see also Table VIII). Combined, these contribute an uncertainty of 2.1 events, or
 1801 47%, to the predicted matrix background of 4.4 events.

1802 The predicted contribution from $t\bar{t}$ dilepton events, $N_{\text{matrix}}^{\text{dil}}$, is computed from the number
 1803 of predicted pretag $t\bar{t}$ events, which is based on the number of observed candidates and the
 1804 predicted background in the pretag sample. The uncertainty on this prediction contributes
 1805 another 1.5 events to the uncertainty on $N_{\text{matrix}}^{\text{dil}}$, bringing its total uncertainty to 2.3 events.
 1806 This is another 34% uncertainty on the matrix background prediction.

1807 The total systematic uncertainty on the data-based background prediction is 2.6 events
 1808 or 59%.

1809 *2. Lepton + Jets with a Fake Second Lepton*

1810 The estimate $N_{\text{fakes}}^{\text{LJ}}$ of the number of background events from $t\bar{t}$ lepton + jets events with
 1811 a fake second lepton has the same sources of systematic uncertainty as the pretag fake lepton
 1812 background estimate, upon which it is based. This is a 20% systematic uncertainty on the
 1813 overall normalization and a 9% systematic uncertainty on the opposite sign fraction used
 1814 for lepton + jets events. See Section VII A for details.

1815 This background has a smaller additional contribution to the uncertainty which is unique
 1816 to the tagged background estimate. These are a 3% statistical uncertainty on $f_{W \geq 3j}^{\text{tag}}$ and a
 1817 4% statistical uncertainty on $f_{\text{tag}}^{\text{top}}$. Combined, these add an extra 5% uncertainty to the fake

Source	Uncertainty (in events)	Uncertainty on background	Uncertainty on cross section
tag matrix technique	2.6	59%	4%
$t\bar{t}$ (lepton + jets) + fake lepton	1.2	22%	2%
total	2.8	30%	5%

TABLE IX: Summary table of systematic uncertainties on the tagged background estimate.

1818 lepton background.

1819 The total systematic uncertainty on the background from lepton + jets events with a
1820 fake lepton is 1.2 events.

1821 The total tagged background systematic uncertainty is obtained by adding the total un-
1822 certainty on the matrix and fakes predictions in quadrature. We find the overall systematic
1823 uncertainty on the background estimate to be 2.8 events, or 30%. The systematic uncertain-
1824 ties on all of the backgrounds, and the corresponding uncertainty contributed to the cross
1825 section measurement, are collected in Table IX.

1826 IX. RESULTS

1827 We first describe the likelihood used to derive the cross section results, including the
1828 treatment of uncertainties. Then we summarize the predicted and observed event counts
1829 and present the cross sections for the two individual samples, the combined result, and
1830 selected kinematic distributions.

1831 A. Likelihood Fit

1832 To calculate the cross section results, we construct a likelihood function describing the
1833 joint probability of finding a particular number of candidate events in each sample given the
1834 predicted signal and backgrounds. We vary the input parameters to find the cross section
1835 value most likely to give the observed number of candidates in each sample.

1836 In order to combine the results, we must define two statistically independent samples so
1837 that the number of candidates in each can be described by independent Poisson distributions.
1838 Because the tagged events are a subset of the pretag events, we can divide the pretag

1839 candidate events into non-overlapping tagged and untagged samples. Although everything
1840 in this paper is described in terms of the pretag and tagged samples, the combined result is
1841 found from the tagged and untagged samples. The expected number of events in the tagged
1842 sample has already been characterized in terms of the signal acceptance, the event tagging
1843 efficiency, and the calculated background. The expected number of events in the untagged
1844 sample may be derived from the information about the tagged and pretag samples. The
1845 acceptance is identical to both the pretag and tagged samples, and the fraction of pretag
1846 events that go into the untagged sample is approximately $1 - \epsilon_{\text{tag}}$, where ϵ_{tag} is the event
1847 tagging efficiency. The equality is not exact because there are some events in the pretag
1848 sample which cannot be tagged because the silicon tracking was not in usable condition
1849 when those events were recorded (data quality requirements are described in Section III).
1850 Therefore, we calculate the number of expected untagged signal events as the difference
1851 between the predicted number of pretag and tagged signal events. Similarly, the backgrounds
1852 in the untagged sample are calculated as the difference between the pretag and tagged
1853 backgrounds.

1854 The likelihood function has seven independent parameters. One is the input cross section,
1855 and the other six are “nuisance parameters” corresponding to systematic uncertainties. The
1856 likelihood \mathcal{L} may be expressed as:

$$\begin{aligned} \log \mathcal{L} = & \log \mathcal{P}(N_u, N_u^{\text{pred}}) + \log \mathcal{P}(N_t, N_t^{\text{pred}}) \\ & + \sum_{i=1}^6 \left(\frac{1}{2} \frac{(Q_i - Q_i^0)^2}{\delta Q_i} \right) \end{aligned} \quad (20)$$

1857 where

$$N_t^{\text{pred}} = \sigma \mathcal{A} \epsilon_{\text{tag}} \int \mathcal{L} dt + B_t(\sigma) \quad (21)$$

1858 and

$$N_u^{\text{pred}} = N^{\text{pred}} - N_t^{\text{pred}} \quad (22)$$

$$= \sigma \mathcal{A} \int \mathcal{L} dt + B(\sigma) - N_t^{\text{pred}}. \quad (23)$$

1859 A Poisson distribution $\mathcal{P}(N, N^{\text{pred}})$ describes the probability to find N candidates given
1860 the mean number N^{pred} predicted. The number of tagged and untagged candidates are
1861 each described as independent Poisson distributions. In the above, N^{pred} is the number
1862 of candidates predicted in the pretag sample, N_t^{pred} is the number predicted in the tagged

1863 sample, and N_u^{pred} is the number predicted in the untagged sample. The corresponding
 1864 numbers of observed candidates are N , N_t , and N_u . \mathcal{A} is the pretag acceptance, ϵ_{tag} is the
 1865 event tagging efficiency, $\int \mathcal{L} dt$ is the integrated luminosity, and σ is the $t\bar{t}$ cross section,
 1866 for which we are fitting. The pretag and tagged background estimates, which depend on
 1867 the signal cross section, are $B(\sigma)$ and $B_t(\sigma)$. The probability distribution used for the
 1868 nuisance parameters, such as the acceptance and backgrounds, is a Gaussian centered on
 1869 the predicted value and having width equal to the relevant systematic uncertainty. This is
 1870 shown as the sum in Equation 20, where Q_i^0 is the central value of the nuisance parameter,
 1871 Q_i is the varied value, and δQ_i the associated uncertainty.

1872 The systematic uncertainties treated as nuisance parameters are on the acceptance, the
 1873 event tagging efficiency, the fake lepton background in the pretag and tag samples, the
 1874 remaining pretag background from Drell-Yan and diboson events, and the remaining tagged
 1875 background as estimated using the data-driven matrix method. These sources of uncertainty
 1876 are independent from each other, but some of them are shared between the pretag and tagged
 1877 measurements, and are varied together in the fit. Table X shows the cross section inputs
 1878 and their uncertainties, with the correlations between uncertainties shown. For example, the
 1879 systematic uncertainty on the acceptance is correlated because the same number is used in
 1880 both the tag and pretag samples. The number of expected tagged and untagged events vary
 1881 up or down together with the acceptance. In contrast, the uncertainty on the event tagging
 1882 efficiency applies to the tagged sample but not the pretag sample. As the event tagging
 1883 efficiency is varied in the fit, the number of events predicted shifts between the tagged and
 1884 untagged samples but their sum, the number of pretag events, remains constant. To put it
 1885 another way, the number of predicted untagged signal events is correlated with the number
 1886 of pretag and tagged events through the acceptance, but anticorrelated with the number
 1887 of tagged signal events through the event tagging efficiency. The common 20% systematic
 1888 uncertainty on the background from fake leptons is treated similarly to the acceptance,
 1889 because the predicted pretag, tagged, and untagged background from fake leptons will all
 1890 increase or decrease together. This happens because the tagged fake lepton background
 1891 prediction is normalized to the pretag fake lepton background prediction. All additional
 1892 uncertainties on the pretag and tagged backgrounds are treated independently, because the
 1893 calculations do not depend on each other, and the sources of uncertainty are distinct.

1894 Some of the background calculations depend on the $t\bar{t}$ cross section, the quantity we

	Pretag	Tagged
Acceptance (%)	$0.84 \pm 0.03 \pm 0.0$	$0.84 \pm 0.03 \pm 0.0$
Event Tagging Efficiency	-	$0.67 \pm 0.0 \pm 0.04$
Background from Fake Leptons (events)	$29.9 \pm 5.9 \pm 0.0$	$5.2 \pm 1.2 \pm 0.05$
Other Pretag Backgrounds (events)	$24.0 \pm 0.0 \pm 3.1$	-
Other Tagged Backgrounds (events)	-	$4.4 \pm 0.0 \pm 2.6$

TABLE X: Likelihood inputs for the pretag and tagged samples, with systematic uncertainties. Uncertainties are shown in the form (number) \pm (correlated uncertainty) \pm (uncorrelated uncertainty). The fake lepton background for tagged events includes only the leading $t\bar{t}$ lepton + jets contribution, because the W + jets contribution is included in the tag-matrix-based background calculation, which is uncorrelated with the pretag background estimate.

1895 wish to measure. In the fitting procedure, the number of predicted events is calculated as
1896 a function of the cross section. In addition to recalculating the number of expected signal
1897 events, we also recalculate the number of background events for the cross section at each
1898 point in the fit. This removes any dependence of the measured cross section on the expected
1899 value and allows the statistical uncertainties to be correctly calculated.

1900 The seven parameters is allowed to float, and we find the combination that maximizes
1901 the likelihood. The cross section at the maximum is our result. To calculate the uncertainty
1902 on the combined cross section, we find the points above and below the maximum value of
1903 the likelihood function at which the logarithm of the likelihood function has decreased by
1904 0.5.

1905 To estimate the expected improvement in precision of the combined cross section over
1906 the two single measurements we perform pseudoexperiments with an input cross section of
1907 6.7 pb. We find an expected improvement in precision of 15%, from 21% to 18%. The
1908 pull distribution from these pseudoexperiments is shown in Fig. 11. The pull distribution
1909 width is one within the uncertainties, demonstrating that the experimental uncertainties
1910 are correctly estimated. The slight bias in the mean is due to the fact that the number of
1911 candidates is restricted to integer values. This limits the possible values of the measured
1912 cross section for samples with small expected numbers of events.

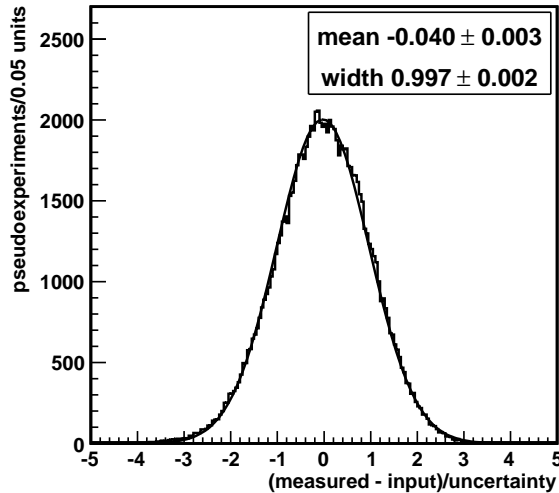


FIG. 11: Pull distribution from pseudoexperiments run with the likelihood used to find the combined cross section.

B. Pretag Sample

Using the event selection described in Section IV, we find 129 pretag candidate events in the data, which has an acceptance-weighted integrated luminosity of $1070 \pm 60 \text{ pb}^{-1}$. The background is calculated to be 53.8 ± 6.7 events and the summed acceptance times efficiency is $0.84 \pm 0.03\%$. Using these, we calculate the cross section using the likelihood fit described earlier in this section. Assuming $m_t = 175 \text{ GeV}/c^2$ and $BR(W \rightarrow \ell\nu) = 10.8 \%$, we find

$$\sigma_{t\bar{t}} = 8.3 \pm 1.3(\text{stat.}) \pm 0.8(\text{sys.}) \pm 0.5(\text{lum.}) \text{ pb} ,$$

consistent with the standard model prediction of $6.6_{-0.5}^{+0.3} (\text{scale})_{-0.3}^{+0.4} (\text{PDF}) \text{ pb}$ [8].

For the pretag sample, the signal and background predictions are summarized and compared to the observed number of candidate events, for events with zero, one, and two or more jets, in Table XI. The zero and one jet event comparisons test the background predictions, because the contribution from $t\bar{t}$ in these jet multiplicities is very small. The number of events predicted and observed agree for all jet multiplicities, although it should be noted that the zero jet events are not as strong of a cross-check, since a subset of these is used to derive the opposite-sign fraction for $W + \text{jets}$ events with a fake lepton (see Section VII A). Figure 12 is a visual representation of Table XI. In both the table and the figure, the signal

	0 jets	1 jet	≥ 2 jets
WW	85.8 ± 8.7	14.9 ± 1.5	3.7 ± 0.4
WZ	9.3 ± 1.0	4.3 ± 0.5	1.3 ± 0.2
ZZ	6.0 ± 0.6	1.6 ± 0.2	0.8 ± 0.1
$Z/\gamma^* \rightarrow ee$	71.3 ± 15.7	25.5 ± 6.0	7.6 ± 2.2
$Z/\gamma^* \rightarrow \mu\mu$	17.9 ± 5.2	8.4 ± 2.7	3.2 ± 1.1
$Z/\gamma^* \rightarrow \tau\tau$	35.5 ± 3.2	26.5 ± 2.5	7.3 ± 0.9
Fakes	244.1 ± 46.4	76.8 ± 14.6	29.9 ± 5.9
All Backgrounds	469.9 ± 52.5	157.9 ± 17.2	53.8 ± 6.7
$t\bar{t}, \sigma = 6.7$ pb	1.2 ± 0.1	17.3 ± 0.6	60.3 ± 1.9
Predicted	471.1 ± 52.5	175.2 ± 17.3	114.2 ± 7.1
Observed	443	187	129

TABLE XI: Predicted and observed pretag events in 1.1 fb^{-1} , with details of the background contributions. Systematic uncertainties on the predictions are included.

1929 prediction is shown at the theoretical cross section value of 6.7 pb, but the backgrounds
1930 which depend on the $t\bar{t}$ cross section are calculated at the measured value of 8.3 pb.

1931 The cross section calculated at other values of m_t is shown in Table XIV. The measured
1932 cross section decreases with increasing m_t even though the number of observed events is
1933 unchanged. For higher top quark masses $t\bar{t}$ decay products are more energetic and there-
1934 fore more likely to pass the kinematic selection, increasing the acceptance. The background
1935 estimates also depend weakly on the top quark mass through the use of simulated $t\bar{t}$ events
1936 to calculate the prevalence of $t\bar{t}$ in control data samples and the background from $t\bar{t}$ lep-
1937 ton + jets events with a fake lepton.

1938 We compare the kinematic features of the observed pretag lepton + track candidates to
1939 the expected distributions. In each of these figures, the $t\bar{t}$ contribution is normalized to the
1940 measured cross section, so only the shapes of the distributions are to be compared, not the
1941 normalization. One of the most prominent features of dilepton $t\bar{t}$ events in particular is the
1942 \cancel{E}_T from the two neutrinos. Figure 13 compares the \cancel{E}_T spectrum of candidate events to the
1943 summed spectra expected for signal and background as predicted by simulation. Because
1944 the top quark is so massive, the H_T distribution of $t\bar{t}$ events, defined as the scalar sum of

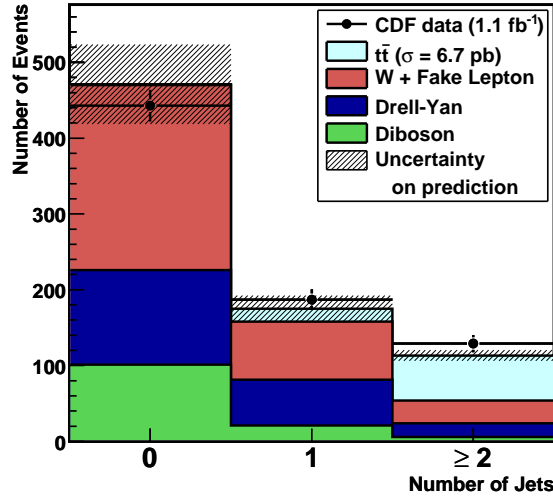


FIG. 12: Number of predicted pretag lepton + track events compared to the number observed in the CDF data. The cross-hatched areas show the combined statistical and systematic uncertainties (one standard deviation) on the prediction.

1945 the primary lepton E_T , track lepton p_T , \cancel{E}_T , and the E_T of all jets in the event, is also
 1946 distinctive. The H_T distribution, shown in Fig. 14, is skewed toward higher values for the $t\bar{t}$
 1947 signal than for its backgrounds. Turning to the charged leptons in the event, we show the
 1948 p_T of the fully reconstructed lepton and the track lepton in Fig. 15, and their invariant mass
 1949 in Fig. 16. Fig. 15 is useful for comparing the signal to the background contribution from
 1950 events with a fake lepton, since the latter produces a much softer lepton p_T distribution, due
 1951 to the exponentially falling jet p_T spectrum. Similarly, Fig. 16 is useful for comparing the
 1952 signal to the background from Drell-Yan events, since the invariant mass distribution is more
 1953 peaked for this background than for the signal. The agreement between the predicted and
 1954 observed distributions suggests that the content of the candidate sample is well-understood
 1955 within the uncertainties.

1956 C. Tagged Sample

1957 In the tagged sample, we find 69 candidate events, and measure 9.5 ± 2.8 background
 1958 events. The predicted and observed numbers of events in the sample, with the prediction
 1959 divided by source, are shown in Table XII. The inputs to the tagged cross section calculation

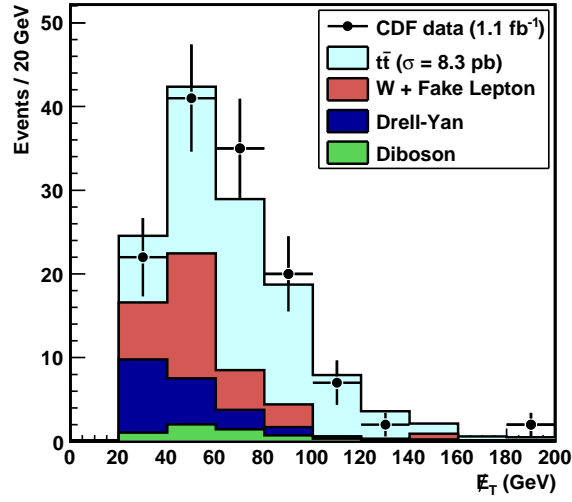


FIG. 13: Missing transverse energy of pretag lepton + track candidate events with two or more jets, compared to the predicted distribution. The highest bin shown includes all events which would be past the right edge of the plot.

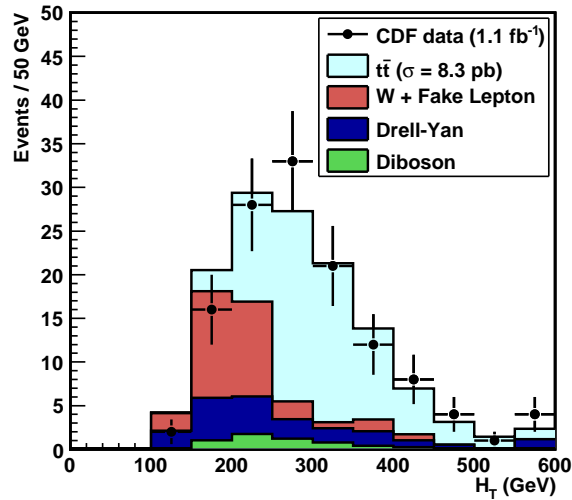


FIG. 14: Summed transverse energy (H_T) of pretag lepton + track candidate events with two or more jets, compared to the predicted distribution. The sum includes the fully reconstructed lepton, the track lepton, the \cancel{E}_T , and all jets passing the analysis selection. The highest bin shown includes all events which would be past the right edge of the plot.

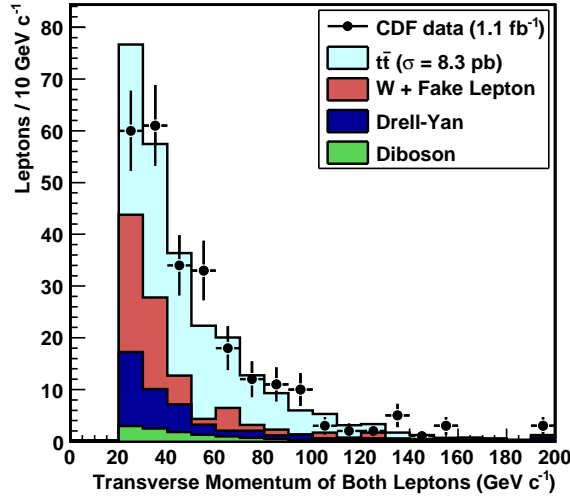


FIG. 15: Distribution of lepton transverse momenta in pretag lepton + track candidate events with two or more jets, compared to the predicted distribution. There are two entries for each event; one each for the fully reconstructed lepton and the isolated track. For fully reconstructed electrons, the E_T is used to estimate the p_T . The highest bin shown includes all events which would be past the right edge of the plot.

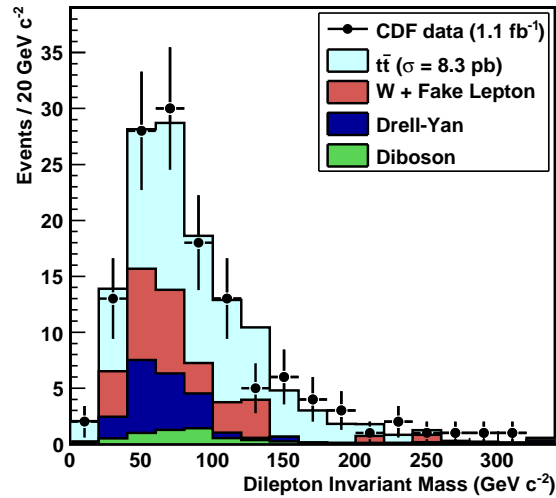


FIG. 16: Reconstructed invariant mass of the fully reconstructed lepton and isolated track pair in pretag candidate events with two or more jets, compared to the predicted distribution. The highest bin shown includes all events which would be past the right edge of the plot.

1960 are summarized in Table XIII. Using data with an integrated luminosity of $1000 \pm 60 \text{ pb}^{-1}$,
 1961 and assuming $m_t = 175 \text{ GeV}/c^2$ and $BR(W \rightarrow \ell\nu) = 10.8 \%$ we find:

$$\sigma_{t\bar{t}} = 10.5^{+1.4}_{-1.3} \text{ (stat.) }^{+0.8}_{-0.7} \text{ (sys.) } \pm 0.6 \text{ (lum.) pb .}$$

1962 The tagged cross section as a function of assumed top quark mass is included in Table XIV.
 1963 Similar to the pretag measurement, the background estimate is relatively insensitive to the
 1964 value of the top quark mass. The event tagging efficiency, for top quark masses between
 1965 170 and 180 GeV/c^2 , is consistent with that measured at $m_t = 175 \text{ GeV}/c^2$. Therefore, the
 1966 only change to the measurement as a function of the top quark mass is the acceptance for
 1967 $t\bar{t}$ events.

1968 The tagged cross section has a combined lower uncertainty of 1.6 pb, including the uncer-
 1969 tainty on the luminosity. This translates to an excess above the standard model prediction
 1970 of 2.4 in units of the calculated uncertainty on the measurement. However, the tagged mea-
 1971 surement is consistent with the pretag measurement. The two measurements differ by the
 1972 observed 2.2 pb in about 10% of pseudoexperiments, where the exact fraction depends on the
 1973 assumed true cross section. The kinematic features of the observed candidates are also con-
 1974 sistent with the standard model expectation, which for the tagged sample are predominantly
 1975 $t\bar{t}$.

1976 Figures 17-21 display some of the kinematic features of the tagged candidate sample,
 1977 compared the expected combined signal and background contribution. In all of these fig-
 1978 ures, the signal is normalized to the measured cross section. The H_T and \cancel{E}_T of the tagged
 1979 candidate events are shown in Fig. 17 and Fig. 18, respectively. These both have distinctive
 1980 distributions for $t\bar{t}$ events; see the discussion above on pretag kinematic distributions for de-
 1981 tails. Fig. 19 and 20 show the transverse momentum distributions of the fully reconstructed
 1982 leptons and the isolated tracks. Fig. 21 shows a unique feature of the tagged events, the
 1983 distance along the tagged jet axis from the interaction point to the reconstructed secondary
 1984 vertex, which corresponds to the distance traveled by the b hadron before decaying. In all of
 1985 the figures, the last bin on the right includes all events which would be past the right edge
 1986 of the plot.

1987 In all of the distributions, good agreement is observed between the candidate events
 1988 from data and the expected distributions. Comparing the distributions from the tagged
 1989 sample to the ones from the pretag sample, the improvement in sample purity from the b -

Source	Number of events
From Matrix (e.g. $Z + b\bar{b}$)	4.4 ± 2.6
Fakes	5.2 ± 1.2
All Backgrounds	9.5 ± 2.8
$t\bar{t}, \sigma = 6.7$ pb	37.7 ± 2.4
Predicted	47.3 ± 3.7
Observed	69

TABLE XII: Predicted and observed events with two or more jets, at least one of which is tagged, in 1.0 fb^{-1} , with details of the background contributions.

Input	Value
N^{tag}	69
$N_{\text{bkgd}}^{\text{tag}}$	9.5 ± 2.8
$\mathcal{A} \times \int \mathcal{L} dt$	$8.4 \pm 0.03 \text{ pb}^{-1}$
ϵ_{tag}	0.669 ± 0.037

TABLE XIII: Predicted background and observed events in 1.0 fb^{-1} , with inputs to the cross section calculation for the tagged analysis. Systematic uncertainties are included in the prediction numbers.

1990 tag requirement is evident. The agreement between the predicted and observed distributions
1991 shows that although the measured cross section is on the high side, the observed candidates
1992 are consistent with the expected $t\bar{t}$ signature.

1993 D. Combined Cross Section Results

1994 Using the likelihood fitter, we find a combined cross section of

$$\sigma_{t\bar{t}} = 9.6_{-1.3}^{+1.4}(\text{stat+sys}) \pm 0.6(\text{lum}) \text{ pb}$$

1995 OR

$$\sigma_{t\bar{t}} = 9.6 \pm 1.2(\text{stat})_{-0.5}^{+0.6}(\text{sys}) \pm 0.6(\text{lum}) \text{ pb.}$$

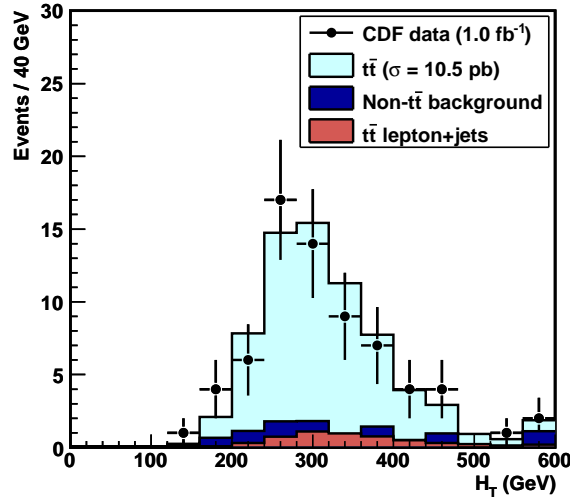


FIG. 17: Summed scalar energy (H_T) of the fully reconstructed lepton, the isolated track, the \cancel{E}_T and all jets in the tagged candidate sample, compared to the combined signal and background predictions.

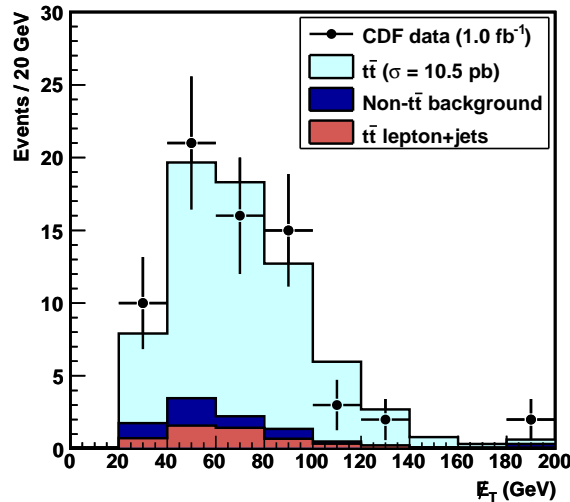


FIG. 18: Missing transverse energy of the lepton + track tagged candidate sample, compared to the combined signal and background predictions.

1996 The 14% combined statistical and systematic uncertainty is an improvement in precision on
 1997 either of the individual measurements. The combined cross section is also shown as a function
 1998 of the assumed top quark mass in Table XIV and Fig. 22. In both, the measured cross
 1999 section is compared to the theoretical prediction. Both the predicted and measured cross

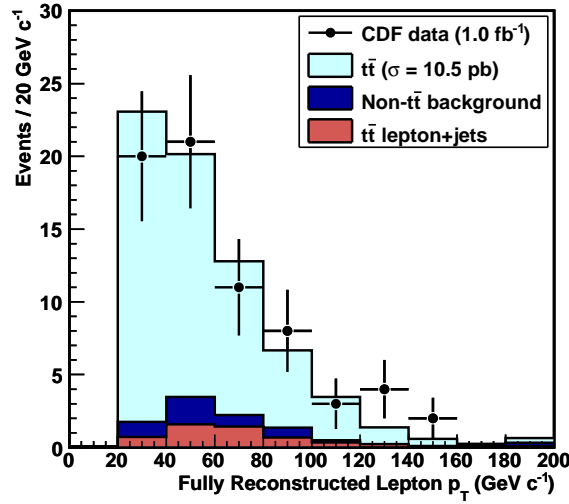


FIG. 19: Transverse momentum of the fully reconstructed lepton in the tagged lepton + track candidate sample, compared to the combined signal and background predictions. The E_T is used as an estimate of the lepton p_T for fully reconstructed electron candidates.

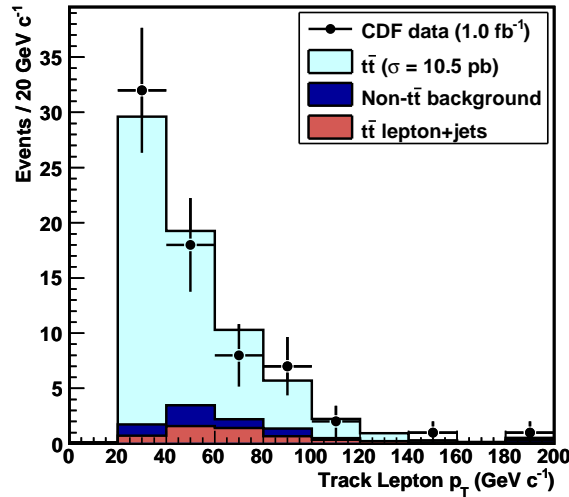


FIG. 20: Transverse momentum of the track lepton (isolated track) in the tagged lepton + track candidate sample, compared to the combined signal and background predictions.

2000 section depend on the top quark mass, but the dependence is stronger for the predicted cross
 2001 section. The predicted cross section drops off with increasing top quark mass because of the
 2002 increased collision energy needed to exceed the kinematic threshold for pair production of top
 2003 quarks. The measured cross section depends on the assumed mass more weakly, through the

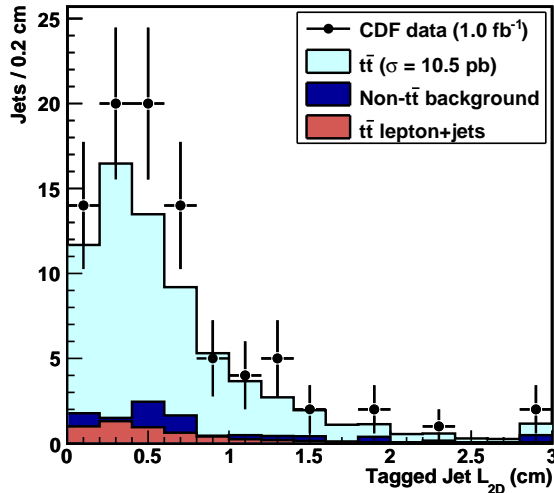


FIG. 21: Distance along the jet axis to the reconstructed secondary vertex in tagged jets in the lepton + track candidate sample, compared to the combined signal and background predictions.

2004 increased acceptance at higher top quark masses because of the increased average transverse
 2005 momentum of the decay products.

2006 To facilitate comparison of this result with other measurements and calculations, which
 2007 may be performed at different assumed top quark masses, we fit the combined cross section
 2008 results shown in Table XIV to the functional form

$$\sigma_{t\bar{t}}(m_t) = A + B(m_t - 175) + C(M_t - 175)^2,$$

2009 in the spirit of Ref. [8]. The top quark mass m_t is in GeV/c^2 , and the fit yields the coefficients
 2010 $A = 9.6 \text{ pb}$, $B = 4.4 \times 10^{-2} \text{ pb}/(\text{GeV}/c^2)$, and $C = 9.6 \times 10^{-3} \text{ pb}/(\text{GeV}/c^2)^2$.

2011 We compare the measured cross section to the standard model prediction at the current
 2012 world average measurement, $173.1 \text{ GeV}/c^2$ [3]. Using the fit described in the previous para-
 2013 graph, we measure $9.7_{-1.4}^{+1.5} \text{ pb}$, where the uncertainty includes the statistical, systematic, and
 2014 luminosity uncertainties. The prediction for this top quark mass from Ref. [8] is $7.0_{-0.6}^{+0.5} \text{ pb}$.
 2015 The uncertainty on the difference between the two, 1.5 pb , includes the uncertainty on
 2016 the measurement and the theoretical prediction. The significance of the the difference is
 2017 therefore $2.7 \text{ pb}/1.5 \text{ pb} = 1.8$. Comparison of the kinematics of the pretag and tagged can-
 2018 didate samples to the standard model expectation shows that the content of the sample is
 2019 reasonably well-understood. Also, the measurement agrees with the $D\bar{D}$ measurement in
 2020 the dilepton channel, $7.4 \pm 1.4 \text{ (stat.)} \pm 0.9 \text{ (sys.)} \pm 0.5 \text{ (lum.) pb}$ [21], as well as with the

Input m_t (GeV/ c^2)	Theoretical	Pretag	Measured cross section (pb)		
	σ (pb)	$t\bar{t}$ Acceptance	Pretag	Tagged	Combined
170	$7.7^{+0.6}_{-0.7}$	0.80 ± 0.02 %	$8.8^{+1.7}_{-1.6}$	$11.0^{+1.7}_{-1.5}$	$10.1^{+1.4}_{-1.3}$
172.5	$7.1^{+0.6}_{-0.6}$	0.83 ± 0.02 %	$8.5^{+1.7}_{-1.5}$	$10.7^{+1.7}_{-1.5}$	$9.8^{+1.4}_{-1.3}$
175	$6.6^{+0.5}_{-0.6}$	0.84 ± 0.03 %	$8.3^{+1.6}_{-1.5}$	$10.5^{+1.6}_{-1.5}$	$9.6^{+1.4}_{-1.3}$

TABLE XIV: The pretag and tagged cross section as calculated at several input top masses. Theoretical prediction from Ref. [8]. The statistical and systematic uncertainties are combined, and a common uncertainty of 6%, due to the uncertainty on the integrated luminosity, is omitted.

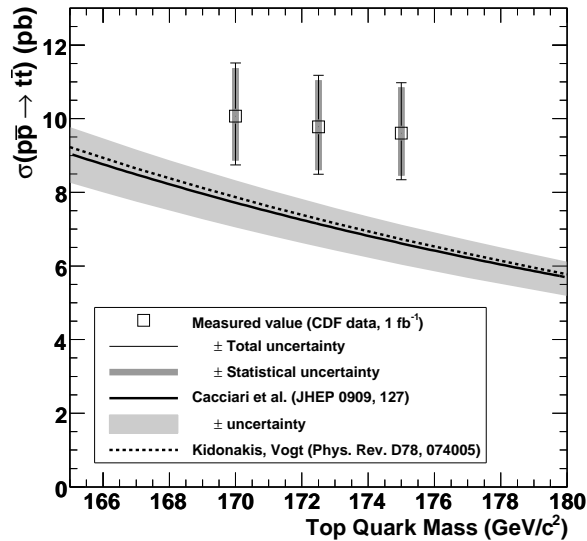


FIG. 22: Measured cross section as a function of the assumed top quark mass, compared to theoretical predictions for the cross section.

2021 published measurements from other channels cited in the Introduction, most of which are
2022 also above the predicted theoretical value.

2023 X. CONCLUSION

2024 We have measured the $t\bar{t}$ production cross section in the dilepton channel using events
2025 selected with one fully reconstructed lepton and one isolated track, both with and without
2026 the requirement that at least one jet in the event be tagged as a b . The combined result of

2027 these measurements is

$$\sigma_{t\bar{t}} = 9.6 \pm 1.2(\text{stat})_{-0.5}^{+0.6}(\text{sys}) \pm 0.6(\text{lum}) \text{ pb}$$

2028 for a top quark mass of 175 GeV/ c^2 . This is the first dilepton cross section result from
2029 CDF which uses b -tagging information. We have also improved the estimation of the pretag
2030 backgrounds with respect to the previous publication, particularly for the background from
2031 events in which a jet has been reconstructed as an isolated track. These changes, combined
2032 with the integration of more data, result in a more precise measurement of the cross section
2033 in the dilepton channel compared to other published results.

2034 The cross sections measured are high compared to the standard model prediction, but
2035 the consistency between the tagged and pretag measurements, their agreement with other
2036 published measurements, and the consistency of the candidate event kinematics with the
2037 standard model all support the hypothesis that the high cross sections observed are consis-
2038 tent with an upward fluctuation in the number of $t\bar{t}$ events accepted by the lepton + track
2039 selection.

2040 **Acknowledgments**

2041 We thank the Fermilab staff and the technical staffs of the participating institutions for
2042 their vital contributions. This work was supported by the U.S. Department of Energy and
2043 National Science Foundation; the Italian Istituto Nazionale di Fisica Nucleare; the Min-
2044 istry of Education, Culture, Sports, Science and Technology of Japan; the Natural Sciences
2045 and Engineering Research Council of Canada; the National Science Council of the Republic
2046 of China; the Swiss National Science Foundation; the A.P. Sloan Foundation; the Bun-
2047 desministerium für Bildung und Forschung, Germany; the Korean Science and Engineering
2048 Foundation and the Korean Research Foundation; the Science and Technology Facilities
2049 Council and the Royal Society, UK; the Institut National de Physique Nucleaire et Physique
2050 des Particules/CNRS; the Russian Foundation for Basic Research; the Ministerio de Ciencia
2051 e Innovación, and Programa Consolider-Ingenio 2010, Spain; the Slovak R&D Agency; and

2052 the Academy of Finland.

- 2053 [1] F. Abe *et al.* (CDF Collaboration), Phys. Rev. Lett. **74**, 2626 (1995).
2054 [2] S. Abachi *et al.* (DØ Collaboration), Phys. Rev. Lett. **74**, 2632 (1995).
2055 [3] Tevatron Electroweak Working Group, FERMILAB-TM-2427-E (2009).
2056 [4] C. Amsler *et al.* (Particle Data Group), Phys. Lett. **B667**, 1 (2008).
2057 [5] M. Cacciari *et al.*, JHEP **04**, 068 (2004).
2058 [6] R. Bonciani *et al.*, Nucl. Phys. **B529**, 424 (1998).
2059 [7] N. Kidonakis and R. Vogt, Phys. Rev. **D68**, 114014 (2003).
2060 [8] M. Cacciari *et al.*, JHEP **09**, 127 (2008).
2061 [9] N. Kidonakis and R. Vogt, Phys. Rev. **D78**, 074005 (2008).
2062 [10] S. Moch and P. Uwer, Nucl. Phys. Proc. Suppl. **183**, 75 (2008).
2063 [11] M. Schmaltz and D. Tucker-Smith, Ann. Rev. Nucl. Part. Sci. **55**, 229 (2005).
2064 [12] C. T. Hill and S. J. Parke, Phys. Rev. **D49**, 4454 (1994).
2065 [13] B. Lillie *et al.*, JHEP **09**, 074 (2007).
2066 [14] U. Baur and L. H. Orr, Phys. Rev. **D76**, 094012 (2007).
2067 [15] T. Aaltonen *et al.* (CDF Collaboration), Phys. Rev. Lett. **100**, 231801 (2008).
2068 [16] T. Aaltonen *et al.* (CDF Collaboration), Phys. Rev. **D77**, 051102 (2008).
2069 [17] V. M. Abazov *et al.* (DØ Collaboration), Submitted to Phys. Lett. B (2008).
2070 [18] H. P. Nilles, Phys. Rept. **110**, 1 (1984).
2071 [19] H. E. Haber and G. L. Kane, Phys. Rept. **117**, 75 (1985).
2072 [20] D. Acosta *et al.* (CDF Collaboration), Phys. Rev. Lett. **93**, 142001 (2004).
2073 [21] V. M. Abazov *et al.* (DØ Collaboration), Phys. Rev. **D76**, 052006 (2007).
2074 [22] A. Abulencia *et al.* (CDF Collaboration), Phys. Rev. **D74**, 072006 (2006).
2075 [23] A. Abulencia *et al.* (CDF Collaboration), Phys. Rev. Lett. **97**, 082004 (2006).
2076 [24] V. M. Abazov *et al.* (DØ Collaboration), Phys. Rev. Lett. **100**, 192004 (2008).
2077 [25] V. M. Abazov *et al.* (DØ Collaboration), Phys. Rev. Lett. **100**, 192003 (2008).
2078 [26] T. Aaltonen *et al.* (CDF Collaboration), Phys. Rev. **D76**, 072009 (2007).
2079 [27] V. M. Abazov *et al.* (DØ Collaboration), Phys. Rev. **D76**, 072007 (2007).
2080 [28] A. Abulencia *et al.* (CDF Collaboration), J. Phys. **G34**, 2457 (2007).

- 2081 [29] C. S. Hill (CDF Collaboration), Nucl. Instrum. Meth. **A530**, 1 (2004).
- 2082 [30] A. Sill *et al.* (CDF Collaboration), Nucl. Instrum. Meth. **A447**, 1 (2000).
- 2083 [31] A. Affolder *et al.* (CDF Collaboration), Nucl. Instrum. Meth. **A453**, 84 (2000).
- 2084 [32] A. Affolder *et al.* (CDF Collaboration), Nucl. Instrum. Meth. **A526**, 249 (2004).
- 2085 [33] L. Balka *et al.* (CDF Collaboration), Nucl. Instrum. Meth. **A267**, 272 (1988).
- 2086 [34] M. G. Albrow *et al.* (CDF Collaboration), Nucl. Instrum. Meth. **A480**, 524 (2002).
- 2087 [35] L. Nodulman *et al.*, Nucl. Instr. Meth. **204**, 351 (1983).
- 2088 [36] G. Apollinari *et al.*, Nucl. Instrum. Meth. **A412**, 515 (1998).
- 2089 [37] G. Ascoli *et al.*, Nucl. Instrum. Meth. **A268**, 33 (1988).
- 2090 [38] T. Dorigo *et al.* (CDF Collaboration), Nucl. Instrum. Meth. **A461**, 560 (2001).
- 2091 [39] B. L. Winer, Int. J. Mod. Phys. **A16S1C**, 1169 (2001).
- 2092 [40] K. Anikeev *et al.* (CDF Collaboration), Comput. Phys. Commun. **140**, 110 (2001).
- 2093 [41] T. Sjöstrand *et al.*, Comput. Phys. Commun. **135**, 238 (2001).
- 2094 [42] G. Corcella *et al.*, JHEP **01**, 010 (2001).
- 2095 [43] M. L. Mangano *et al.*, JHEP **07**, 001 (2003).
- 2096 [44] J. Pumplin *et al.* (CTEQ Collaboration), JHEP **07**, 012 (2002).
- 2097 [45] R. Brun and F. Carminati, CERN Programming Library Long Writeup **W5013** (1993).
- 2098 [46] G. Grindhammer *et al.*, Nucl. Instrum. Meth. **A290**, 469 (1990).
- 2099 [47] E. Gerchtein and M. Paulini (2003), eCONF C0303241, TUMT005.
- 2100 [48] D. E. Acosta *et al.* (CDF Collaboration), Phys. Rev. **D71**, 051104 (2005).
- 2101 [49] A. Bhatti *et al.*, Nucl. Instrum. Meth. **A566**, 375 (2006).
- 2102 [50] A. Abulencia *et al.* (CDF Collaboration), Phys. Rev. **D73**, 032003 (2006).
- 2103 [51] A. D. Martin *et al.*, Eur. Phys. J. **C35**, 325 (2004).
- 2104 [52] A. D. Martin *et al.*, Eur. Phys. J. **C4**, 463 (1998).
- 2105 [53] D. E. Acosta *et al.* (CDF Collaboration), Phys. Rev. **D71**, 052003 (2005).
- 2106 [54] C. Neu (CDF Collaboration), *CDF b-tagging: Measuring efficiency and false positive rate*,
2107 presented at TOP 2006: International Workshop on Top Quark Physics, Coimbra, Portugal,
2108 12-15 Jan 2006.
- 2109 [55] A. Affolder *et al.* (CDF Collaboration), Phys. Rev. Lett. **87**, 211804 (2001).
- 2110 [56] A. Abulencia *et al.* (CDF Collaboration), Phys. Rev. **D75**, 112001 (2007).
- 2111 [57] F. Abe *et al.* (CDF Collaboration), Phys. Rev. Lett. **80**, 2779 (1998).

- 2112 [58] A. Abulencia *et al.* (CDF Collaboration), Phys. Rev. **D76**, 111104 (2007).
- 2113 [59] V. M. Abazov *et al.* (DØ Collaboration), Phys. Rev. Lett. **98**, 161801 (2007).
- 2114 [60] T. Aaltonen *et al.* (CDF Collaboration), Phys. Rev. Lett. **100**, 201801 (2008).
- 2115 [61] V. M. Abazov *et al.* (DØ Collaboration), Phys. Rev. Lett. **101**, 171803 (2008).
- 2116 [62] J. M. Campbell and R. K. Ellis, Phys. Rev. **D60**, 113006 (1999).
- 2117 [63] In hadron-hadron collisions, there is always the possibility of producing additional jets, pho-
- 2118 tons, or other particles in addition to the ones under direct consideration. We will not explicitly
- 2119 write out the “+ X ” after this, but all final states mentioned in this paper are inclusive unless
- 2120 it is explicitly stated otherwise.